



# THE UNIVERSITY *of* EDINBURGH

This thesis has been submitted in fulfilment of the requirements for a postgraduate degree (e.g. PhD, MPhil, DClinPsychol) at the University of Edinburgh. Please note the following terms and conditions of use:

This work is protected by copyright and other intellectual property rights, which are retained by the thesis author, unless otherwise stated.

A copy can be downloaded for personal non-commercial research or study, without prior permission or charge.

This thesis cannot be reproduced or quoted extensively from without first obtaining permission in writing from the author.

The content must not be changed in any way or sold commercially in any format or medium without the formal permission of the author.

When referring to this work, full bibliographic details including the author, title, awarding institution and date of the thesis must be given.

# Prospects for Precision Measurements of the Top-Yukawa Coupling and CP Violation in $t\bar{t}H$ Production at the CLIC $e^+e^-$ Collider

Yixuan Zhang



Doctor of Philosophy  
The University of Edinburgh  
December 2020

# Abstract

High energy particle colliders provide unique facilities to investigate the physics that take place at the smallest scales. The thesis present works for both future and upgraded colliders. CLIC - the Compact Linear Collider - is a proposed high energy electron-positron collider with collision energies between 350 and 3000 GeV. The LHC is a high energy proton-proton collider at CERN operating at 13 TeV. Over the next few years, it will be upgraded to the High-Luminosity LHC to operate at higher luminosities. The thesis presents an analysis of the  $t\bar{t}H$  production at CLIC leading to predicted precisions on top-Yukawa coupling and constraints on the CP properties of the Higgs boson. The thesis also presents work for the ATLAS experiment investigating the suitability of new sensors for use in the HL-LHC and studies of physics processes.

The predicted precision on the top-Yukawa coupling using the  $e^+e^- \rightarrow t\bar{t}H$  process is measured to be 2.7% at  $\sqrt{s} = 1.5$  TeV at CLIC with polarised beams and an integrated luminosity of  $2.5 \text{ ab}^{-1}$  using the CLIC SiD detector model. The  $H \rightarrow b\bar{b}$  final state of the Higgs boson and the 6-jet and 8-jet final states are used for the analysis. A multivariate selection is used to separate the  $t\bar{t}H$  signal from the backgrounds.  $b$ -tagging information is observed to be the strongest variable in the multivariate selection.

The CP-propertis of the top-Higgs coupling are also investigated at  $\sqrt{s} = 1.5$  TeV using CLIC machine. A Higgs boson containing a mixture of scalar and pseudoscalar components is characterised by a mixing angle,  $\phi$ . The precision of the mixing angle  $\phi$  is determined to be  $\Delta \sin^2 \phi \simeq 0.07$  with cross-section measurements from both 6-jet and 8-jet final states. The results can be further improved up to  $\Delta \sin^2 \phi \simeq 0.03$  with an additional angular distribution, up-down asymmetry, in the semi-leptonic channel.

The ATLAS experiment is upgrading its Inner Detector (ID) to an all-silicon

system, the Inner Tracker (ITk). A new Front End chip, RD53A, has been developed using 65 nm CMOS technology. The thesis presents the work on the procedure of setting up the test for the RD53A chip by using testbeam at DESY with EUDET telescope. The **EUTelescope** software is used to reconstruct the tracks of particles and the **TBMon2** framework is used to do the final analysis for the testing module. With data collected in December 2018 at DESY testbeam facility, the residual of the UK RD53A module with cell size of  $50 \times 50 \mu\text{m}^2$  is found to be symmetrical with  $50.7 \mu\text{m}$  in x-axis and  $51.3 \mu\text{m}$  in y-axis. The hit efficiency is determined to be  $97.651\% \pm 0.035\%$  which passes the requirement for the HL-LHC.

# Lay Summary

This thesis presents work investigating some of the big questions about the Universe using high energy particle colliders such as the Large Hadron Collider (LHC) at CERN and a proposed new electron—anti-electron collider called CLIC.

The first question is, where does matter get its mass (or weight)? The theory of particle physics suggests a fundamental subatomic particle called the Higgs boson that is responsible for giving masses to other fundamental particles. To understand the behaviour of the Higgs boson, some of the properties of the Higgs boson are investigated in this thesis.

A second question addressed here is why is there more matter than antimatter in our Universe? Some theories suggest the Higgs boson could be one of the sources that contributes to the matter-antimatter inequality in the Universe. To explore this question, this thesis looks at the properties of the Higgs boson which would be different for the interaction of the Higgs boson with matter and with antimatter.

Finally, this thesis includes an R&D study of a new type of detector that can be used at the ATLAS experiment at the LHC at CERN.

Although proton-proton colliders such as the LHC are more well-known in high energy particle physics, this thesis shows that an electron-positron collider such as CLIC can make more precise measurements of the Higgs boson.

# Acknowledgements

There are many people that I need to thank for my pursuit of the PhD degree. Everyone that I met during my four year has influenced me to become better. First of all, I would like to give my deepest and sincere gratitude to my parents who have been very supportive to my decision of pursuing my dream and thereafter. Both of them are my role models that I will spend my whole life to chase and respect.

I would like to express my sincere gratitude to my PhD supervisor, Victoria Martin. She has been very supportive and helpful throughout my PhD in both academic guidance and life support. Thank you for giving me the opportunity to do research at my dream place, CERN, which has taught me invaluable knowledge and experience. Not only that she has taught me physics knowledge, but also I have learnt a lot of extremely useful soft skills from her. Getting supervised by Victoria is not just fruitful but also fun. Exploring coffee shops has become our weekly task before our every meet up in multiple cities. Thank you for always tirelessly looking for opportunities in entrepreneurship for me even if I only mentioned once. Thank you, you are the best supervisor!

I am very grateful to my supervisor at CERN, Philipp Roloff, for his support and patience in teaching. My knowledge and skills in physics analysis and coding has been greatly improved because of the help from Philipp. Every time when I got stuck on the progress of my analysis, Philipp can always show me the direction to break through. It was my pleasure to work with him and it has been the best time of my research days at CERN.

I also would like to give huge thanks to Yanyan Gao and Stephan Eisenhardt as my hardware project supervisors. I got personal lectures by Stephan when I first start working on hardwares in particle physics during my first year of PhD. A lot of the knowledge still benefits me on many of the practical work. I work with Yanyan for my last year of project work. She has taught me a lot of research techniques as well as influencing me with her passion in physics. She is always nice and patient. I also need to give her big thanks in helping with my thesis.

I would like to express my deep love to my girlfriend Fangfei Du and her family. Thank you for being with me through all my happy and down times during my pursuit of the PhD. Thank you for making me feel like having a second home

when I am studying abroad. I am extremely fortunate to have met you in my life.

Last but not least, I would like to thank the Edinburgh HEP group for all the support. It was my great pleasure to be part of the Edinburgh HEP group. I would also like to thank the CLICdp group at CERN for having me in the group. I was privileged to spend most of my research time at CERN with the CLICdp group. I need give special thanks to Lucie Linssen for kindly funding my stay at CERN. It was my pleasure to share an office with Jean-Jacques Blaising who is an inspiration for my career. I also would like to thank Simon Spannagel, Lars Rickard Strom, Andre Sailer and Dominik Dannheim for helping me with technical guidance for my research at CERN.

Thanks to you all for making my four years more than a PhD.

# Contents

<b>Abstract</b>	i
<b>Lay Summary</b>	iii
<b>Acknowledgements</b>	iv
<b>Contents</b>	vi
<b>List of Publications</b>	xi
<b>1 Introduction</b>	1
<b>2 Current Knowledge of the Universe</b>	4
2.1 Standard Model.....	4
2.2 Fermions.....	6
2.2.1 Leptons.....	6
2.2.2 Neutrinos.....	6
2.2.3 Quarks .....	7
2.3 Fundamental Forces in the SM .....	8
2.3.1 The Strong Interaction.....	9
2.3.2 Weak Isospin .....	10
2.3.3 Weak Hypercharge.....	11

2.3.4	The EW Unification .....	11
2.3.5	Higgs Mechanism.....	11
2.4	The Higgs Boson.....	13
2.4.1	Top-Yukawa Coupling .....	15
2.5	C,P and T Symmetries.....	15
2.5.1	CP Symmetry and Violation .....	16
2.5.2	Sources of CP Violation in SM .....	16
2.6	Beyond the Standard Model .....	17
2.6.1	Higgs Mixing .....	17
2.7	Phenomenology of $t\bar{t}H$ .....	18
2.7.1	Decay Products.....	18
2.8	Proton vs Electron Colliders.....	19
2.9	Current Measurements .....	21
2.9.1	$t\bar{t}H$ Observation .....	21
2.9.2	Higgs Couplings to Particles.....	22
2.9.3	CP Properties of Higgs Boson.....	22
2.10	Summary .....	22
<b>3</b>	<b>The Particle Microscopes</b>	<b>25</b>
3.1	The Particle Microscopes .....	25
3.2	Compact Linear Collider.....	29
3.2.1	CLIC Physics Program .....	31
3.2.2	CLIC Accelerator .....	32
3.2.3	CLIC Detector .....	34

3.3	Summary and Outlook of Future Colliders .....	38
<b>4</b>	<b>Top-Yukawa Coupling and Higgs Boson CP Analysis</b>	<b>40</b>
4.1	Top-Yukawa Coupling Measurement.....	40
4.1.1	Analysis Strategy .....	41
4.1.2	Simulation Samples .....	42
4.2	Event Reconstruction.....	43
4.2.1	PandoraPFA.....	44
4.3	Beam-Induced Background Suppression.....	45
4.4	Lepton Identification.....	48
4.4.1	Impact Parameter.....	48
4.4.2	Track Energy and Calorimeter Energy .....	49
4.4.3	Isolation Information .....	50
4.4.4	Summary of Isolated Lepton Selections.....	52
4.4.5	Summary of Tau Lepton Selections.....	52
4.4.6	Performance of Lepton Selections .....	53
4.5	Jet Grouping and Particle Reconstruction.....	55
4.6	Flavour Tagging.....	57
4.7	Signal Selection using Multivariate Analysis .....	58
4.8	Results on Precision of Top-Yukawa Coupling .....	62
4.8.1	LO to NLO Correction.....	62
4.8.2	CLIC Luminosity Scheme with Polarised Beam .....	63
4.9	Higgs Boson CP Analysis.....	64
4.9.1	Event Generation .....	65

4.9.2	Cross-Section Measurement.....	65
4.9.3	Results on Sensitivity to CP-Mixing in Higgs Boson .....	66
4.9.4	Angular Observable: Up-Down Asymmetry .....	67
4.9.5	Neutrino Reconstruction .....	69
4.9.6	$\chi^2$ Template Fit .....	72
4.9.7	Sensitivity to CP Properties of the Higgs Boson .....	73
4.9.8	Other Observables .....	74
4.10	Comparison with the LHC and Conclusion.....	74
<b>5</b>	<b>The ATLAS ITk Pixel detector</b>	<b>76</b>
5.1	The Large Hadron Collider.....	76
5.1.1	The ATLAS Experiment .....	78
5.1.2	Coordinate System.....	79
5.2	The ATLAS Inner Tracker .....	80
5.3	Test Beam Facility .....	83
5.3.1	DESY .....	83
5.3.2	The EUDET Telescope .....	84
5.4	Track Reconstruction .....	86
5.5	Post-Reconstruction Analysis.....	89
5.5.1	TBmon2 .....	89
5.6	Properties of RD53A .....	90
5.6.1	Residual .....	91
5.6.2	Efficiency.....	92
5.7	Outlook from the Results.....	95



# List of Publications

H. Abramowicz, N. Alipour Tehrani, D. Arominski, Y. Zhang *et al.* “Top-quark physics at the CLIC electron-positron linear collider”. *J. High Energ. Phys.* 3 (2019). [https://doi.org/10.1007/JHEP11\(2019\)003](https://doi.org/10.1007/JHEP11(2019)003)

CLICdp and CLIC Collaborations, P. N. Burrows, Y. Zhang *et al.* “The Compact Linear Collider (CLIC) - 2018 SummaryReport.” *CERN Yellow Reports: Monographs*. <https://doi.org/10.23731/CYRM-2018-002>

J. de Blas, R. Franceschini, F. Riva, P. Roloff, U. Schnoor, Y. Zhang *et al.* “The CLIC Potential for New Physics.” *CERN Yellow Reports: Monographs* Vol. 3 2018. <https://doi.org/10.23731/CYRM-2018-003>

# Chapter 1

## Introduction

Human beings have been trying to answer big questions about the Universe since ancient Greek times. Some of the unsolved questions are theoretical, meaning that existing theory cannot explain the observed phenomenon. Others are experimental, either because experimental apparatus is not precise enough to investigate further details or there is difficulty creating an experiment to test a proposed theory.

One of the most important questions in particle physics is to understand the origin of masses of fundamental particles. A theoretical model used to solve this is first proposed by three independent groups in 1964: by Peter Higgs [1]; by François Englert and Robert Brout [2]; and by Gerald Guralnik, C. R. Hagen, and Tom Kibble [3]. This model is called the Higgs mechanism and it is part of the Standard Model (SM) of particle physics. Without the Higgs mechanism, the gauge bosons responsible for interactions would all be massless, whereas experimental results suggest  $W^\pm$  and  $Z$  bosons have relatively large masses. A particle that explains this mechanism is the Higgs boson.

In 2012, the Higgs boson is first observed by the ATLAS and CMS experiments at the LHC with a mass of  $m_h \simeq 125$  GeV [4, 5]. Since then, both the ATLAS and CMS experiments are measuring the properties of Higgs boson. So far the results have shown a good consistency with the prediction by the Standard Model (SM) [6]. Precise measurements on Higgs properties could help to probe physics beyond the Standard Model (BSM) [7]. There still remains a few pressing questions which cannot be explained by current theories. One of them is the baryon asymmetry in the Universe [8]. New sources of CP violation could be able to explain this

question and is predicted by many extension theories of the SM.

The coupling strength between the Higgs boson and a fermion is referred to as the Yukawa coupling [9]. The SM predicts a linear dependent relation between the Yukawa coupling strength and the masses of the fermion [7]. The strongest coupling is therefore to the heaviest fermion - top quark, usually refer to top-Yukawa coupling,  $g_{t\bar{t}H}$ . It is kinematically forbidden for Higgs to decay into top quarks, but the large value of this coupling still leads to high rates of production of a Higgs boson with a pair of top quarks. Hence, the  $t\bar{t}H$  process is the best channel to study the top-Yukawa coupling [10, 11].

The  $t\bar{t}H$  process can be accessed at both the CLIC and the LHC. At the Compact Linear Collider (CLIC), a proposed future  $e^+e^-$  collider, the  $t\bar{t}H$  process can be accessed with high rate from the second energy stage at  $\sqrt{s} = 1.5$  TeV with a luminosity of  $2.5 \text{ ab}^{-1}$  [12]. The collision environment at an  $e^+e^-$  collider is much cleaner than a  $pp$  collider. Therefore, physics quantities are expected to be measured more precisely at an  $e^+e^-$  collider. In this thesis, the statistical uncertainty of the top-Yukawa coupling is measured in  $e^+e^- \rightarrow t\bar{t}\Phi$  where  $\Phi$  is a CP-mixed Higgs boson at  $\sqrt{s} = 1.5$  TeV with an integrated luminosity assumed to be  $2.5 \text{ ab}^{-1}$  with polarised beams. The result can then be compared with the projection of measurement from the HL-LHC [13, 14].

At the Large Hadron Collider (LHC), an existing  $pp$  collider, the  $t\bar{t}H$  process was first observed in 2017 at  $\sqrt{s} = 13$  TeV with a luminosity of  $36.1 \pm 0.8 \text{ fb}^{-1}$  [15]. To increase the potential for more discoveries, the LHC is increasing the luminosity for the High-Luminosity LHC (HL-LHC) project. The designed luminosity is expected to be 10 times more than at the current LHC. This allows access to rare processes such as  $t\bar{t}H$  with more data and hence can help us understand the physics in much more detail. For the preparation of the HL-LHC phase, the ATLAS and the CMS experiments at the LHC are upgrading their detectors to cope with the high particle density environment near the interaction point. This requires the detectors to have much smaller pixels, high radiation tolerance and high rate capability. For this purpose, the ATLAS experiment plans to replace its current Inner Detector (ID) to a full-silicon system, the Inner Tracker (ITk). The RD53 collaboration is developing a front end chip for the ATLAS ITk. The performance of this RD53A chip is tested by testbeam at DESY and is described in this thesis.

This thesis is structured in 6 chapters. A theoretical description of the Standard

Model and  $t\bar{t}H$  process is presented in Chapter 2. Both the  $e^+e^-$  linear collider, CLIC, and the  $pp$  circular collider, LHC, are described in Chapter 3. A brief description of the CLIC detector and ATLAS experiment is also presented in this section. Chapter 4 contains the analysis of top-Yukawa coupling measurements and CP studies of the Higgs boson at CLIC. Chapter 5 presents the work on the ATLAS ITk pixel detectors preparing for the upcoming HL-LHC upgrade. The thesis will finally be concluded and summarised in Chapter 6.

# Chapter 2

## Current Knowledge of the Universe

### 2.1 Standard Model

The Standard Model of particle physics (SM) is a theoretical model that describes the interactions between the elementary particles via three out of the four fundamental forces. In the SM, the quantum field theory used to describe phenomena observed in particle physics is very successful at providing accurate predictions. The SM theorises the interactions between the different types of elementary particles: fermions and bosons. Fermions include quarks and leptons which are collectively known as the “matter particles”. Bosons are the force carriers of the fundamental forces. The Higgs boson, that is also included in the SM, is responsible for generating the masses of elementary particles via *electroweak symmetry breaking*.

The SM is a renormalisable quantum field theory described as gauge fields under the  $SU(3)_C \times SU(2)_L \times U(1)_Y$  symmetry group<sup>1</sup> with fermions introduced as spinor fields. Each symmetry group describes a type of interaction, which occur through exchanging gauge bosons. The two symmetry groups  $SU(2) \times U(1)$  can be unified into the so-called *electroweak interaction* [16]. After spontaneous symmetry breaking, this becomes  $U(1)_{em}$  which is governed by the quantum electrodynamics (QED) [17]. Quarks are spin-1/2 particles with colour charges (red, green and blue) and undergo interactions by exchanging massless gluons. This is the strong nuclear interaction described using  $SU(3)$  by the Quantum

---

<sup>1</sup>The subscripts indicate the quantum number that the symmetry group couples to.  $C$  stands for colour charge,  $L$  stands for left-handed and  $Y$  stands for weak hypercharge.

Chromodynamics (QCD) [18, 19]. An overview of the SM is illustrated in Figure 2.1

In the following sections, a brief description of the SM, including the fundamental interactions between particles, is given. The properties of the heaviest SM particle, the top quark, is discussed in detail. The Higgs mechanism and the properties of the Higgs boson such as its production, decay and coupling to other particles, particularly to the top quarks, are described. Furthermore, CP-violation is briefly described. Shortcomings of the SM are discussed which lead to other models such supersymmetry, including Minimal Supersymmetric Standard Model (MSSM) [20]. Finally, CP mixing of the Higgs boson is discussed and current measurements from the LHC are presented.

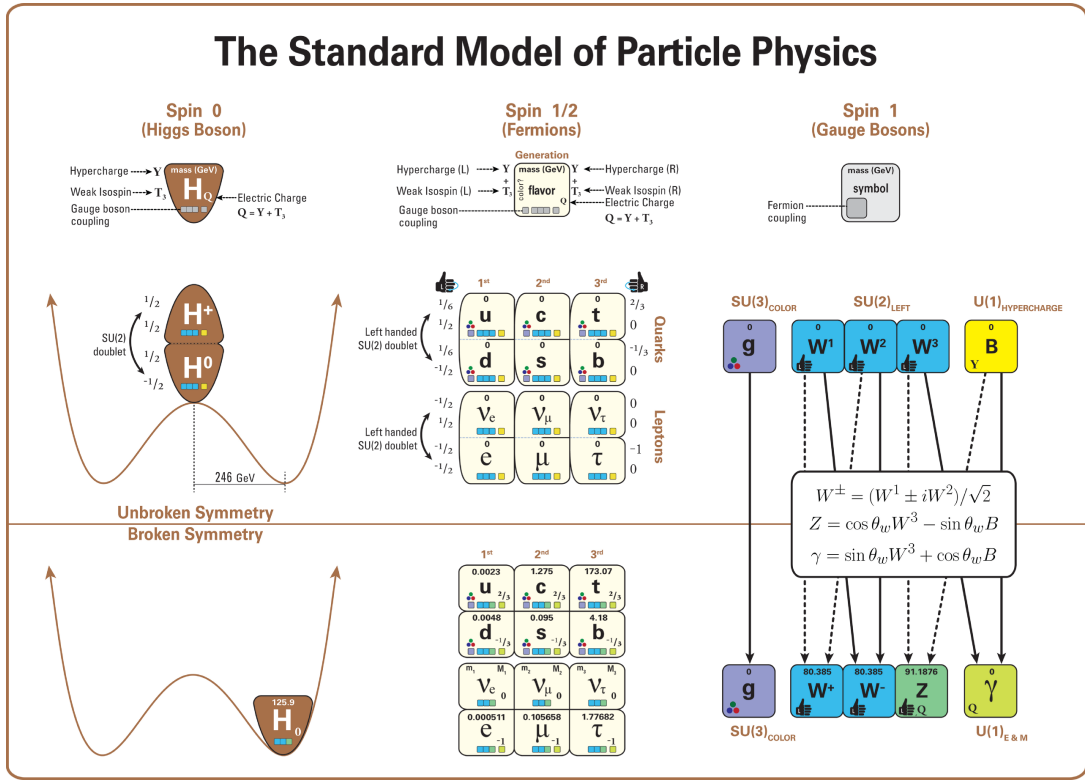


**Figure 2.1** Overview of the fermions and bosons described by the SM [21].

<sup>1</sup>The subscripts indicate the quantum number that the symmetry group couples to.  $C$  stands for colour charge,  $L$  stands for left-handed and  $Y$  stands for weak hypercharge.

## 2.2 Fermions

Fermions ( $f$ ) are the building block of our Universe. They consists of two types of particles: leptons ( $\ell$ ) and quarks ( $q$ ). There are three generations, with increasing masses. Quarks and leptons are spin-1/2 particles, therefore, in the SM, fermion fields are described using Dirac spinors denoted as  $\psi$ . Helicity is defined as the projection of spin onto the direction of momentum. If the direction of a particle's spin is in the same direction as its momentum, the helicity of the particle is right-handed and left-handed if opposite. All fermions have various charges: electrical charge ( $Q$ ), hyper charge ( $Y$ ), colour charge ( $C$ ) and weak isospin ( $I$ ) as described in Figure 2.1.

### 2.2.1 Leptons

Each lepton family is composed of a pair of a charged lepton ( $-e$ ) and an associated neutrino in each generation, including electrons  $e, \nu_e$ , muons  $\mu, \nu_\mu$  and taus  $\tau, \nu_\tau$ . Weak isospin  $I$  is a quantum number relating to weak interaction. Its third component  $I_3$  is conserved in all weak interactions. Left-handed leptons build up doublets  $(\nu_e, e^-)_L$ ,  $(\nu_\mu, \mu^-)_L$  and  $(\nu_\tau, \tau^-)_L$  with  $I_3 = +1/2$  and  $I_3 = -1/2$  respectively. In the SM, neutrinos are all left-handed and right-handed leptons are singlets  $e_R, \mu_R, \tau_R$  with  $I = 0$ . The EM force acts on all particles with a non-zero electric charge and the weak force acts on all particles with a non-zero weak isospin. Therefore, charged leptons interact via EM and weak forces, whereas neutrinos only interact through weak force.

### 2.2.2 Neutrinos

Neutrinos are very hard to detect as they are essentially massless and rarely interact with matter particles in the SM. However, neutrinos have been found to have non-zero masses from the observation of neutrino oscillations [22, 23]. Various experiments indicate that neutrinos have very small masses and have set experimental boundaries with an upper limit of 1.1 eV at 90% confidence level on the absolute mass scale of neutrinos [24].

### 2.2.3 Quarks

Quarks have a total of six flavours with two flavours in each generation. Each generation consists of an up-type and a down-type quark which carry electric charges of  $+2/3$  e and  $-1/3$  e respectively. The first generation is  $u$  and  $d$  quarks, the second generation contains charm  $c$  and strange  $s$  quarks, and the third generation includes top  $t$  and bottom  $b$  quarks. Left-handed quarks have a weak isospin value of  $I = 1/2$ , and right-handed quarks are isospin  $I = 0$ . Left-handed quarks can be grouped into doublets with weak isospin of  $\pm 1/2$  that behaves the same way as the weak interaction. Up-type quarks ( $u, c, t$ ) have the third component  $I_3 = +1/2$  and always transform into down-type quarks ( $d, s, b$ ) that have  $I_3 = -1/2$  via weak interaction. The weak interactions can occur either through charged-current interaction or neutral-current interaction by mediating a  $W$  boson or a  $Z$  boson respectively. Quarks never decay weakly into another quark with the same weak isospin. Right-handed quarks are singlets with both a weak isospin of  $I = 0$  and the third component  $I_3 = 0$  and do not undergo weak interactions.

The probabilities of transition between quark flavour  $i$  and quark flavour  $j$  are described by the unitary Cabibbo-Kobayashi-Maskawa (CKM) matrix [25, 26] with element  $V_{ij}$

$$\begin{pmatrix} d' \\ s' \\ b' \end{pmatrix} = \begin{pmatrix} V_{ud} & V_{us} & V_{ub} \\ V_{cd} & V_{cs} & V_{cb} \\ V_{td} & V_{ts} & V_{tb} \end{pmatrix} \begin{pmatrix} d \\ s \\ b \end{pmatrix} \quad (2.1)$$

with weak eigenstates on the left side, CKM matrix and a vector of down-type mass eigenstates on the right. The elements of the CKM matrix,  $V_{ij}$ , describes the transition from a quark of flavour  $i$  to a quark of flavour  $j$  with a probability of  $|V_{ij}|^2$ . The diagonal elements  $V_{ud} = 0.97446 \pm 0.00010$ ,  $V_{cs} = 0.97359^{+0.00010}_{-0.00011}$  and  $V_{tb} = 0.999105 \pm 0.000032$  represents the transitions within the same generation [27]. They are determined close to unity which means quarks are most likely to change flavours within the same generation.

Unlike leptons, quarks cannot be observed as free particles in nature. Each quark carries one of three *colour charges* (red, green or blue) and forms colour-neutral bound states referred to as *hadrons* due to *confinement*. Hadrons can be formed with either three quarks with three different colour charges ( $qqq$ , known as baryons, or  $\bar{q}\bar{q}$ ) or a quark with its anti-quark of opposite colour charges ( $q\bar{q}$ , known as mesons).

## 2.3 Fundamental Forces in the SM

The SM includes three of the four fundamental forces observed in the nature: the strong nuclear force, the weak nuclear force and the electromagnetic force (EM). It describes particles interactions through these forces via exchanging gauge bosons. However, the gravitational force is not included in the SM as its formulation within quantum field theory is not yet proven successful.

A hypothetical gauge boson, the graviton, would be introduced if gravity were included in the model. Due to its small coupling to the SM particles, the existence of gravity in the SM would not be significant enough to affect the predictions from the SM. The first observation of gravitational waves in 2016 may allow limits to be set on the mass of hypothetical gravitons to complete a unified theory of all four fundamental forces [28].

Physical processes occur when the corresponding symmetry group is invariant under gauge transformation performed at every point in the spacetime coordinates. The SM has a symmetry group  $SU(3)_C \times SU(2)_L \times U(1)_L$ . Starting with gauge invariance in the electromagnetism symmetry group  $U(1)$  with vector potential  $A_\mu = (\phi, -\mathbf{A})$ .

The gauge transformation can be written as

$$A_\mu \rightarrow A'_\mu = A_\mu - \partial_\mu \chi. \quad (2.2)$$

In relativistic quantum mechanics, the symmetry of EM  $U(1)$  requires the invariance of spinor  $\psi$  under local gauge transformation:

$$\psi(x) \rightarrow \psi'(x) = \hat{U}(x)\psi(x) = e^{iq\chi(x)}\psi(x). \quad (2.3)$$

where the phase  $q\chi(x)$  is an arbitrary function at any point in space-time. For this local phase transformation, the free-particle Dirac equation,

$$i\gamma^\mu \partial_\mu \psi = m\psi, \quad (2.4)$$

receives an additional term  $-q\gamma^\mu(\partial_\mu \chi)\psi$ . Hence, local phase invariance is not possible without an interaction. Therefore, the free-particle Dirac equation is

modified to include a new degree of freedom  $A_\mu$  which becomes

$$i\gamma^\mu(\partial_\mu + iqA_\mu)\psi - m\psi = 0, \quad (2.5)$$

where  $A_\mu$  is interpreted as a massless gauge field and  $q\gamma^\mu A_\mu\psi$  becomes an interaction term. Equation 2.5 can also be expressed using a covariant derivative

$$D_\mu \equiv \partial_\mu + iqA_\mu. \quad (2.6)$$

and the Dirac equation becomes

$$i\gamma^\mu D_\mu\psi - m\psi = 0. \quad (2.7)$$

The requirements of phase transformation with gauge invariance of  $U(1)$  implies the existence of a photon field  $A_\mu$  and fermions charge  $q$ .

### 2.3.1 The Strong Interaction

The strong interaction is described by Quantum Chromodynamics (QCD) [29] based on symmetry group  $SU(3)_C$ . It is the strongest fundamental force which is around 137 times of EM force,  $10^6$  times of weak force and about  $10^{36}$  times of gravitational force. However, it only acts at a distance of 1 fm or less.

Similar to  $U(1)$  local gauge symmetry, QCD is invariant under  $SU(3)$  local phase transformation:

$$\psi(x) \rightarrow \psi'(x) = \hat{U}(x)\psi(x) = e^{igs\boldsymbol{\alpha}(x)\cdot\hat{\mathbf{T}}}\psi(x). \quad (2.8)$$

Here  $g_S$  is the coupling constant of QCD interactions,  $\boldsymbol{\alpha}(\mathbf{x}) = \{\alpha(x)^a\}$  are eight functions of space-time coordinate  $x$  and  $\hat{\mathbf{T}} = \{T^a\}$  are the eight generators of the  $SU(3)$  symmetry group where  $a = 1, \dots, 8$ . The new degree of freedom is termed *colour* with red, green and blue labelling the states of the quarks and gluons. For this local gauge transformation, the Dirac equation becomes

$$i\gamma^\mu(\partial_\mu + igsG_\mu^a T^a)\psi - m\psi = 0, \quad (2.9)$$

with new gauge fields  $G_\mu^a \equiv \partial_\mu\alpha(x)^a$ . Each index  $a = 1, \dots, 8$  corresponds to one of the eight generators of  $SU(3)$  symmetry group, indicating eight colour states of gluons.

The gluon field between a pair of colour charged particles forms a flux tube between them and the strong force between the particles stays constant regardless of separation. To certain extent of separation, the energy required to separate the particles is sufficient to form another pair of colour-charged particles in the flux tube and two pairs of quarks are produced. Due to this effect, colour-charged particles are not observed as free particles and only exist in colour-neutral bound states in nature. This phenomenon is called *confinement*. As the energy scale increases and the corresponding length scale decreases, colour-charged particles interact weakly with each other and behave almost as free particles. This effect is referred to as *asymptotic freedom*.

### 2.3.2 Weak Isospin

The weak interactions, governed by symmetry group  $SU(2)$ , only interact with left-handed fermions or right-handed anti-fermions. It describes how particles changes flavours though radioactive decays.

The weak isospin ( $I$ ) serves as a quantum number of and governs how particles behave in the weak interactions. All left-handed fermion or right-handed anti-fermions have a third weak isospin value of either  $I_3 = +1/2$  or  $I_3 = -1/2$ , and they are the only particles participate in the weak interaction characterised by the V–A (vector minus axial-vector) structure. This leads to violation of the parity symmetries and charge conjugation, i.e. CP violation.

Similar to Equation 2.6, the Dirac equation of the weak interaction after  $SU(2)$  local phase transformation can be written as

$$i\gamma^\mu(\partial_\mu + ig_W \boldsymbol{\sigma} \cdot \mathbf{W}_\mu)\psi - m\psi = 0, \quad (2.10)$$

with weak coupling constant  $g_W$ , Pauli matrices  $\boldsymbol{\sigma}$ <sup>2</sup> and weak isospin fields  $\mathbf{W}_\mu \equiv W_\mu^a$  where  $a = 1, 2, 3$ . This indicates three boson fields in the  $SU(2)$  symmetry. Since the  $SU(2)$  symmetry group only interacts with left-handed fermions, for convenience, it is usually represented as  $SU(2)_L$ .

---

<sup>2</sup>The Pauli matrices  $\boldsymbol{\sigma}$  are a set of three  $2 \times 2$  complex matrices which are Hermitian and unitary.  $\sigma_1 = \begin{pmatrix} 0 & 1 \\ 1 & 0 \end{pmatrix}$ ,  $\sigma_2 = \begin{pmatrix} 0 & -i \\ i & 0 \end{pmatrix}$  and  $\sigma_3 = \begin{pmatrix} 1 & 0 \\ 0 & -1 \end{pmatrix}$ .

### 2.3.3 Weak Hypercharge

The weak hypercharge is the generator of the  $U(1)_Y$  group. It is a quantum number relating to the electric charge  $Q$  and the third component of weak isospin  $I_3$ , defined as  $Y = 2(Q - I_3)$ . The  $U(1)_Y$  symmetry group acts on particles with non-zero hypercharge under weak hypercharge field  $B_\mu$ . Therefore, the Dirac interaction becomes

$$i\gamma^\mu(\partial_\mu + ig'YB_\mu)\psi - m\psi = 0, \quad (2.11)$$

with coupling constant  $g'$ .

### 2.3.4 The EW Unification

The EM interaction and the weak interaction can be unified into the electroweak (EW) interaction based on combined symmetry group  $SU(2)_L \times U(1)_Y$ . The electroweak symmetry is described by the weak isospin fields  $\mathbf{W}_\mu$  and the weak hypercharge field  $B_\mu$ . In the EW theory, the  $\mathbf{W}_\mu$  bosons acquire masses through spontaneous symmetry breaking by interacting with the Higgs field, while  $B$  boson still remains massless. The mixing of the  $\mathbf{W}_\mu$  and  $B_\mu$  gauge fields give rise to masses of  $W$ ,  $Z$  and  $\gamma$  bosons.

### 2.3.5 Higgs Mechanism

A new complex scalar field of  $SU(2)_L$  weak isospin doublet, known as Higgs field  $\phi$ , is introduced to break the  $SU(2)_L \times U(1)_Y$  symmetry of the EW interaction:

$$\phi(x) = \begin{pmatrix} \phi^+ \\ \phi^0 \end{pmatrix}, \quad (2.12)$$

The SM Lagrangian density of the Higgs field is defined as

$$\mathcal{L}_{Higgs} = (D_\mu\phi)^\dagger(D_\mu\phi) - V(\phi), \quad (2.13)$$

with kinetic term and potential term  $V(\phi)$ . The kinetic term which describes the “motion” of the fields is defined based on the covariant derivative,  $D_\mu$ , of the  $SU(2)_L \times U(1)_Y$  symmetry group to keep the Lagrangian invariant under local

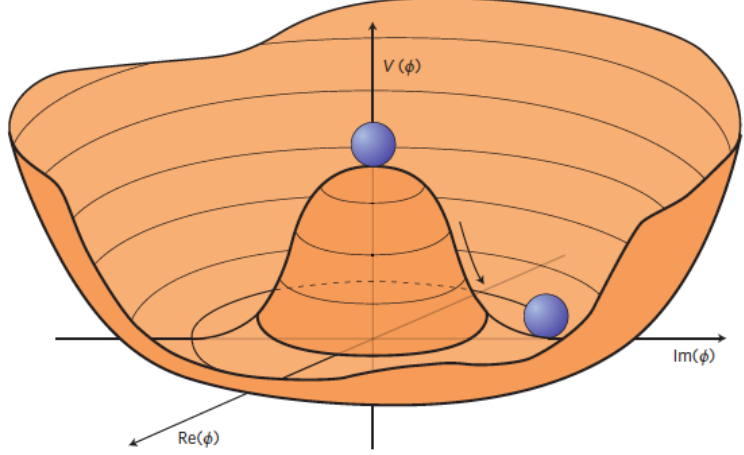


**Figure 2.2** An illustration of Higgs potential against two fields  $Im(\phi^0)$  and  $Re(\phi^0)$  with minimum at  $\mu/\lambda$  [30]. Any point at bottom of the potential breaks the  $U(1)$  symmetry.

$U(1)$  symmetry.

$$D_\mu \phi = (\partial_\mu + \frac{i}{2} g_W \boldsymbol{\sigma} \cdot \mathbf{W}_\mu + \frac{i}{2} g' Y B_\mu) \phi, \quad (2.14)$$

where  $Y = 1$  for the Higgs field. This introduces couplings between the Higgs field and the EW gauge fields  $\mathbf{W}_\mu$ ,  $B_\mu$ . The potential term is defined as

$$V(\phi) = \mu^2 \phi^\dagger \phi + \lambda (\phi^\dagger \phi)^2, \quad (2.15)$$

with parameters  $\mu$  and  $\lambda$  ( $\lambda > 0$ ) determining the shape of the potential. The symmetry is spontaneously broken for  $\mu^2 < 0$ , as it creates an infinite number of minima and the potential forms a ‘Mexican hat’ shape as shown in Figure 2.2. The unitary gauge sets  $\phi^+$  to 0 and make  $\phi^0$  real. This results in a non-zero expectation value of the Higgs potential  $\langle \phi \rangle = \sqrt{-\mu^2/\lambda} \equiv \nu = 246$  GeV is the vacuum expectation value of the Higgs field. Then the Higgs field can be defined as an excitation  $H(x)$  around the vacuum expectation value  $\nu$ :

$$\phi(x) = \frac{1}{\sqrt{2}} \begin{pmatrix} 0 \\ \nu + H(x) \end{pmatrix}, \quad (2.16)$$

where  $H$  indicates the Higgs boson. With the Higgs mechanism, the EW gauge fields  $W_\mu^a$  and  $B_\mu$  interact with each other through mixing to produce physically

observable bosons:

$$\begin{aligned}
Z \text{ boson: } & Z \equiv \cos \theta_W W^3 - \sin \theta_W B, \\
\text{photon: } & A \equiv \sin \theta_W W^3 + \cos \theta_W B, \\
W \text{ boson: } & W^\pm \equiv \frac{1}{\sqrt{2}}(W^1 \mp W^2),
\end{aligned} \tag{2.17}$$

where  $\theta_W \equiv \tan^{-1}(g_W/g')$  is the weak mixing angle,  $e \equiv g_W \sin(\theta_W)$  is the electric charge.

The mass of the  $Z$  boson,  $m_Z$ , and the mass of the  $W$  boson,  $m_W$ , are related as  $m_Z = m_W / \cos \theta_W$ . In terms of the  $SU(2)_L$  and  $U(1)_Y$  couplings, masses of  $Z$  and  $W$  are given by:

$$m_W = \frac{1}{2}g_W\nu, \quad m_Z = \frac{\nu}{2}\sqrt{(g_W^2 + g'^2)}. \tag{2.18}$$

Thus, the overall gauge symmetry  $SU(3)_C \times SU(2)_L \times U(1)_Y$  is broken into  $SU(3)_C \times U(1)_{em}$ . Since the gauge symmetries of  $SU(3)_C$  and  $U(1)_{em}$  are all conserved, the associated gauge bosons, gluons and photons, remain as massless particles.

A new particle arising from the EW symmetry breaking, the Higgs boson, has a mass of  $m_H = \sqrt{2\lambda}\nu$ . The fermions are also given masses through interactions between the fermion fields  $\psi$  and the Higgs field  $H$ :

$$\mathcal{L}_{Yukawa} = -\frac{\nu}{\sqrt{2}}g_f\bar{\psi}\psi - \frac{g_f}{\sqrt{2}}H\bar{\psi}\psi, \tag{2.19}$$

with the Yukawa coupling  $g_f \equiv \sqrt{2m_f}/\nu$ . The masses of fermions are determined to be  $m_f = \nu g_f/\sqrt{2}$  and the Yukawa interaction couples the interactions between the fermions and the Higgs boson. Thus, the mechanism of spontaneous symmetry breaking in EW and the existence of the Higgs field describes the origin of the masses of the fundamental particles in the SM.

## 2.4 The Higgs Boson

The Higgs boson is a spin 0 particle carrying neutral electric charge and colour charge. It was discovered by the ATLAS and the CMS experiments at the LHC in 2012 with measured mass resonance around  $m_H \simeq 125$  GeV [27] with datasets

collected at  $\sqrt{s} = 7$  TeV and 8 TeV [27]. Currently the most precise measurement on the mass of the Higgs boson is  $m_H = 125.38 \pm 0.14$  GeV with dataset collected from 2011 to 2016 [31].

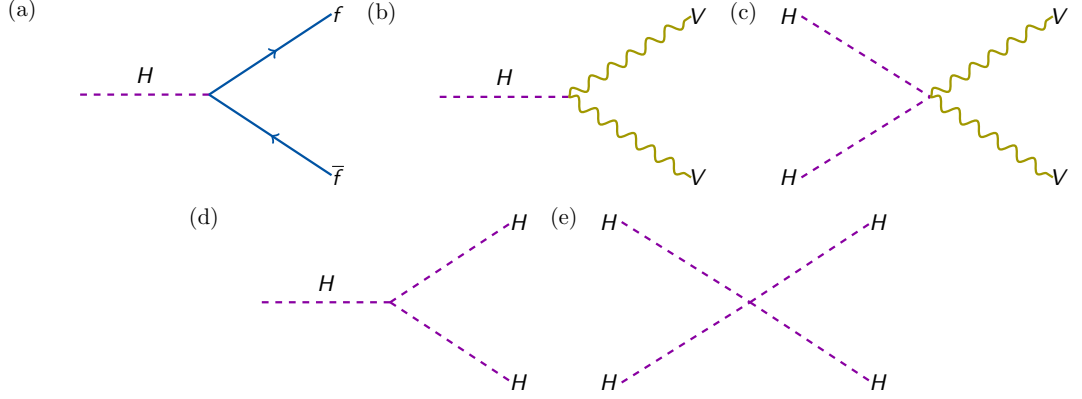


**Figure 2.3** SM interactions of the Higgs boson illustrated using Feynman vertex terms [32]. (a) Yukawa coupling, (b)(c) vector boson interactions and (d) (e) Higgs self-coupling.

The Higgs boson couples to fermions, bosons and the Higgs boson itself as shown in Figure 2.3. The interactions of the Higgs boson can be described by the following Lagrangian:

$$\mathcal{L} = -g_{Hf\bar{f}} \bar{f} f H + \frac{g_{HHH}}{6} H^3 + \frac{g_{HHHH}}{24} H^4 + \delta_V V_\mu V^\mu \left( g_{HVV} H + \frac{g_{HHVV}}{2} H^2 \right) \quad (2.20)$$

with

$$g_{Hf\bar{f}} = \frac{m_f}{\nu}, \quad g_{HVV} = \frac{2m_V^2}{\nu}, \quad g_{HHVV} = \frac{2m_V^2}{\nu^2}, \quad g_{HHH} = \frac{3m_H^2}{\nu}, \quad g_{HHHH} = \frac{3m_H^2}{\nu^2}, \quad (2.21)$$

where  $V = W^\pm$  or  $Z$  and  $\delta_W = 1$ ,  $\delta_Z = 1/2$ . The fermion field  $\psi$  in Equation 2.19 is replaced with  $f$  for simplicity. The strength of the coupling between the Higgs boson and fundamental fermions  $g_{Hf\bar{f}}$  are linearly proportional to the fermion masses, and the couplings to bosons  $g_{HVV}$  and  $g_{HHVV}$  are proportional to the square of the boson masses. Higgs self couplings  $g_{HHH}$  and  $g_{HHHH}$  are proportional to squared mass of itself. The coupling of Higgs to fermions is related to the Yukawa coupling  $g_f$  in Equation 2.19 by a factor of  $\sqrt{2}$ .

## 2.4.1 Top-Yukawa Coupling

The strength of the Yukawa coupling is linearly dependent on the mass of the fermion. The heaviest fermion, top quark, is predicted to have the largest Yukawa coupling  $g_t = \sqrt{2}m_t/v \approx 1$  in the SM.

The Higgs boson couples to fermions mainly through decay process where the Higgs boson decays into a fermion and an antifermion pair. However, it is kinematically forbidden for the Higgs boson to decay into a top quark pair, as top quarks ( $m_t = 172.9 \pm 0.4$  GeV [27]) are heavier than the Higgs boson ( $m_H = 125.10 \pm 0.14$  GeV [27]). Therefore, alternative ways for directly probing the top-Yukawa coupling is needed.

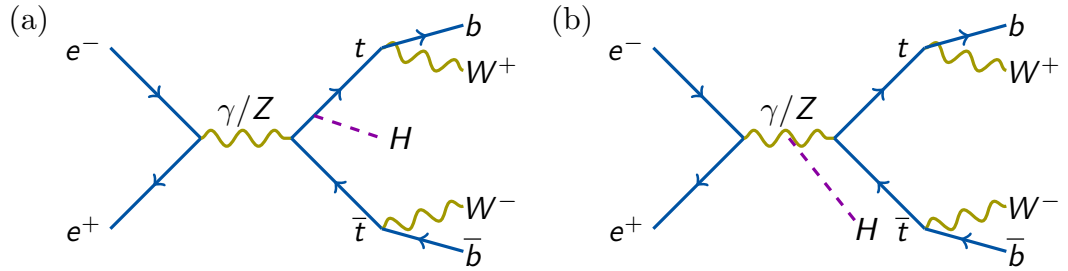


**Figure 2.4** Feynman diagrams of the  $t\bar{t}H$  production at electron-positron colliders. Both processes contribute to the total cross-section of  $t\bar{t}H$ , but only (a) contributes to the top-Yukawa coupling.

The coupling can be directly measured through the associated production of the Higgs boson and a top-antitop quark pair ( $t\bar{t}H$ ). The Higgs boson is radiated from one of the top quarks at which the  $g_{t\bar{t}H}$  can be measured as shown in Figure 2.4(a).

## 2.5 C,P and T Symmetries

$$\begin{aligned}
 \psi &\rightarrow -i(\bar{\psi}\gamma^0\gamma^2)^T \\
 C : \bar{\psi} &\rightarrow -i(\gamma^0\gamma^2\psi)^T \quad P : \begin{pmatrix} x \\ y \\ z \end{pmatrix} \rightarrow \begin{pmatrix} -x \\ -y \\ -z \end{pmatrix} \quad T : t \rightarrow -t \\
 A^\mu &\rightarrow -A^\mu
 \end{aligned} \tag{2.22}$$

Charge, parity and time reversal symmetries are fundamental discrete symmetries of the Universe. Charge conjugation (C) changes particles to its anti-particle, and changes the signs of all charges. Parity transformation (P) flips sign of

spatial coordinates. Time reversal symmetry (T) reverses time as shown in Equation 2.22. Combination of C, P and T in any order is conserved symmetries.

### 2.5.1 CP Symmetry and Violation

CP-symmetry is a product of the charge conjugation and the parity conjugation. It is usually conserved, however, some processes that violate the CP have been observed in the weak interaction [33]. This phenomenon can be used to explain the matter-antimatter asymmetry in the Universe as the Big bang is thought to produce equal amount of matter and anti-matter. Therefore, it is essential to search for phenomenon that exhibit CP violation.

### 2.5.2 Sources of CP Violation in SM

There are at least three sources of CP violation in the SM. The first one, predicted by the SM, exists in the strong interaction by searching for the electric dipole moment of the neutron, but the unsuccessful experimental search suggests that this strong CP violation is too small to account for the matter-antimatter asymmetry. The second source, which involves the CKM matrix, has been experimentally observed and can only account for a small fraction ( $10^{-3}$ ) of the necessary CP-violation in the early universe [34]. The first observation of CP violation was discovered in the decays of neutral kaons in 1964 [35]. Following the discovery, the Large Hadron Collider beauty (LHCb) experiment is measuring CP violation in the interactions of  $b$ -hadrons to help explain the matter-antimatter asymmetry [36]. The third source exist in the lepton mixing matrix, the *Pontecorvo-Maki-Nakagawa-Sakata* (PMNS) matrix, similar to the CKM matrix for quarks. Neutrino oscillation experiments, such as T2K and proposed next-generation experiments Hyper-Kamiokande and DUNE, will search for evidence of more CP violation [37]. A process called leptogenesis, a hypothetical process that produces an asymmetry between lepton and antilepton, could become a potential explanation for the matter-antimatter asymmetry.

So far the amount of CP violation sources found experimentally are not enough to account for the matter-antimatter asymmetry observed in the Universe. New physics beyond the SM would be required to explain the remaining sources of CP violation. Since CP is not a symmetry of nature, new particles and interactions

can be introduced to create new sources of CP violation. Higgs boson interactions would be a good candidate for this new theory. If Higgs boson exhibited any CP-violating properties, it might propagate its CP properties to other particles through interactions under Higgs mechanism introducing more sources of CP violation.

## 2.6 Beyond the Standard Model

The SM Higgs boson is predicted to be CP even and have spin zero,  $J^{CP} = 0^{++}$ . It is possible to have more than one spin-zero Higgs bosons with CP-odd or no definite CP quantum number in the *Beyond The Standard Model* (BSM). For example, in Supersymmetry models [38], an additional complex Higgs doublets is introduced (Equation 2.12). In the *Minimal Supersymmetric extension of the Standard Model* (MSSM) [20], this leads to five physical Higgs states with three neutral, two CP-even ( $H^0$  and  $h^0$ ) and one CP-odd (pseudoscalar  $A^0$ ) and two charged Higgs  $H^\pm$ . The Higgs boson may exhibit a mixed CP property if CP violation is provided by the Higgs sector in the BSM.

### 2.6.1 Higgs Mixing

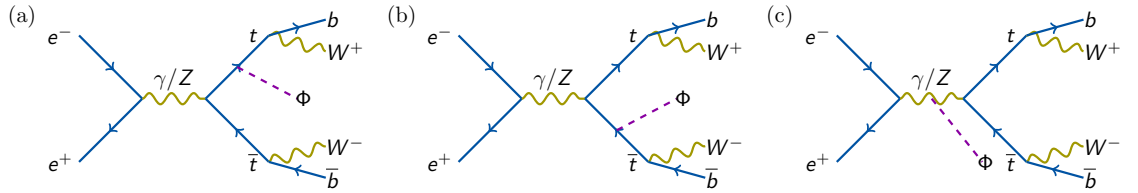


**Figure 2.5** Feynman diagrams for the  $e^+e^- \rightarrow t\bar{t}\Phi$  process with (a) a CP-violating Higgs boson  $\Phi$  radiates from the top quark, (b)  $\Phi$  radiates from  $\bar{t}$  and (c)  $\Phi$  radiates from the  $Z$  boson which will cause interference with (a) and (b).

In order to study the CP properties of the Higgs boson, we introduce an arbitrary CP-violating Higgs boson  $\Phi$  in the  $e^+e^- \rightarrow t\bar{t}\Phi$  process where  $\Phi$  is a mixture of CP-even Higgs and CP-odd Higgs  $|\Phi\rangle = a|H\rangle + b|A\rangle$ . The cross-section of this process is sensitive to the CP nature of the Higgs boson which could allow us to set an upper limit on how precise the CP parameters can be measured.

The  $t\bar{t}\Phi$  coupling with a general CP-violating Higgs  $\Phi$  can be described as [39]

$$C_{\Phi t\bar{t}} = -ig_{Ht\bar{t}}(a + ib\gamma_5). \quad (2.23)$$

The CP parameters  $a$  and  $b$  are real. With this modification,  $a = 1, b = 0$  represents SM case and  $a = 0, b \neq 0$  becomes the pure pseudoscalar Higgs boson case. The exact value of  $b$  depends on the model. Assuming that  $a^2 + b^2 = 1$ , where  $a = \cos \phi$  and  $b = \sin \phi$ , this reduces the free parameter to a mixing angle  $\phi$  [39]. A measurement of  $\phi$  will give direct indication of CP-violation in the Higgs boson.

For the calculation of the total cross-section of  $t\bar{t}\Phi$ , the interference effect from  $ZZ\Phi$  ( $Z \rightarrow t\bar{t}$ ) needs to be taken into account (Figure 2.5(c)). The SM  $ZZH$  does not couple to the CP-odd Higgs boson at least at tree level. To modify this effect in the CP-violating case, the SM  $ZZH$  coupling is parameterised by a real parameter  $c$  [39],

$$g_{\Phi ZZ} = -ic g_{HZZ}. \quad (2.24)$$

The parameter  $c$  is set to 1 in the analysis in Chapter 4 to make a compatible comparison with the result from the LHC [40].

## 2.7 Phenomenology of $t\bar{t}H$

The Higgs boson plays an important role in both the SM and many of the BSM theories [20]. Measurements of its properties can help us understand the SM in more details as well as possibly explaining some of the phenomenon that cannot be explained by the SM. The  $t\bar{t}H$  process gives us a direct access to the largest Yukawa coupling to the Higgs boson [9]. The measurement might be a gateway to search for BSM as many BSM theories requires a precise measurement of top-Yukawa coupling [7]. Any small deviation from SM prediction would already be an indication of new physics.

### 2.7.1 Decay Products

The  $t\bar{t}H$  production also includes processes where the Higgs boson radiates from the mediating photon or  $Z$  boson (2.4(b)). However, it does not contribute to the top-Yukawa coupling.

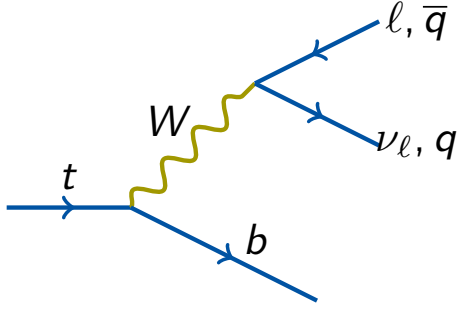


**Figure 2.6** Feynman diagram of the dominant decay product of the top quark and the subsequent  $W$  boson.

A top quark decays into a bottom quark and a  $W^+$  boson (Figure 2.6). The  $W^+$  boson subsequently decays into either a charged antilepton and a corresponding neutrino ( $BR \simeq 33\%$ ) or a quark antiquark pair ( $BR \simeq 67\%$ ) [27]. The bottom quark produced from top quark begins hadronisation and forms jets of hadrons.

The Higgs boson can decay into a fermion or boson pair as shown in Figure 2.7. The most common decay is to a bottom-antibottom quark pair with a branching ratio of 58.2% [27]. Higgs boson decaying into a  $W$  boson pair is the second highest branching ratio with 21.4% [27]. The experimental environment determines which processes are best to observe Higgs bosons.

In  $t\bar{t}H$  production, depending on the subsequent decay products of the  $W$  bosons from top quarks, the search channels can be classified according to the number of charged leptons in their final state as shown in Table 2.1.

No. leptons	Process	Channel name	$BR$
0	$t\bar{t}H \rightarrow b\bar{b}qqqq + b\bar{b}$	Full-hadronic	46%
1	$t\bar{t}H \rightarrow b\bar{b}qq\ell\nu + b\bar{b}$	Semi-leptonic	45%
2	$t\bar{t}H \rightarrow b\bar{b}\ell\ell\nu\nu + b\bar{b}$	Di-leptonic	9%

**Table 2.1** Searching channels classified using different number of leptons with corresponding branching ratio ( $BR$ ) where  $q$ ,  $\ell$  and  $\nu$  represent quark, charged lepton and neutrino.

## 2.8 Proton vs Electron Colliders

Protons consists of  $udd$  valence quarks and are bounded through exchanging gluons. These gluons produce additional quarks inside the proton by splitting to

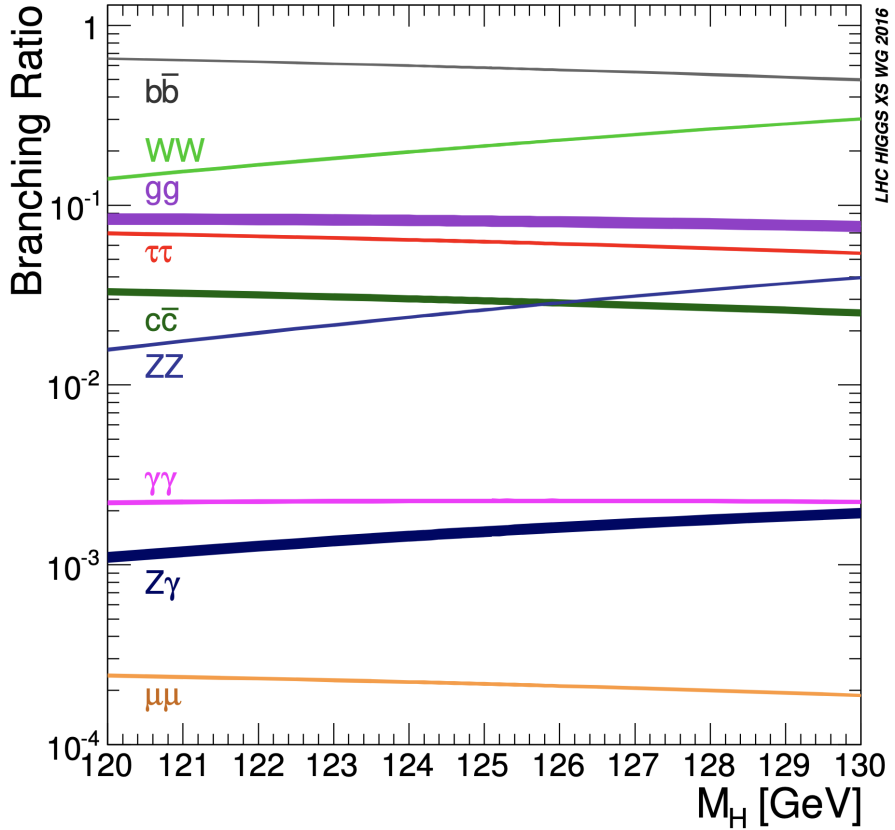


**Figure 2.7** Branching ratios for the main decays of the Higgs boson around  $m_H = 125$  GeV. Theoretical uncertainties are indicated as bands. [27]

form quark anti-quark pairs of *sea quarks*. Therefore, the composition of a proton is not only three valence quarks but also gluons and sea quarks; they are defined as *partons*. A free quark can be produced in high energy collisions, but it will quickly hadronise into colour-neutral bound states. Hence, quarks can only be observed experimentally in the form of bundles of particles known as *jets*.

As a result, proton-proton colliders are characterised by high multiplicity of jets and hence processes with hadrons in their final states are harder to observe experimentally. For instance, Higgs bosons decaying into photon pairs ( $BR = 2.27 \times 10^{-3}$ ) and  $Z$  boson pairs ( $BR = 2.62 \times 10^{-2}$ ) are the key search processes used for Higgs bosons in a proton-proton collisions, as the leptons ( $e, \mu$ ) and photon pairs in the final state can be successfully identified from other particles.

In electron-positron colliders, due to their cleaner environment, it becomes easier to reconstruct jets. This makes  $e^+e^- \rightarrow t\bar{t}H$ , where  $H \rightarrow b\bar{b}$ , the best process to measure  $g_t$  as it has the largest branching ratio. There will be at least 4  $b$ -quarks in the final state.

## 2.9 Current Measurements

Since the discovery of the Higgs boson in 2012 [4, 5], studies of the Higgs boson properties have been the primary task at the LHC [31]. The LHC has made various measurements on the Higgs boson for studying the properties of both SM and BSM cases. No significant deviation from the SM prediction were found.

### 2.9.1 $t\bar{t}H$ Observation

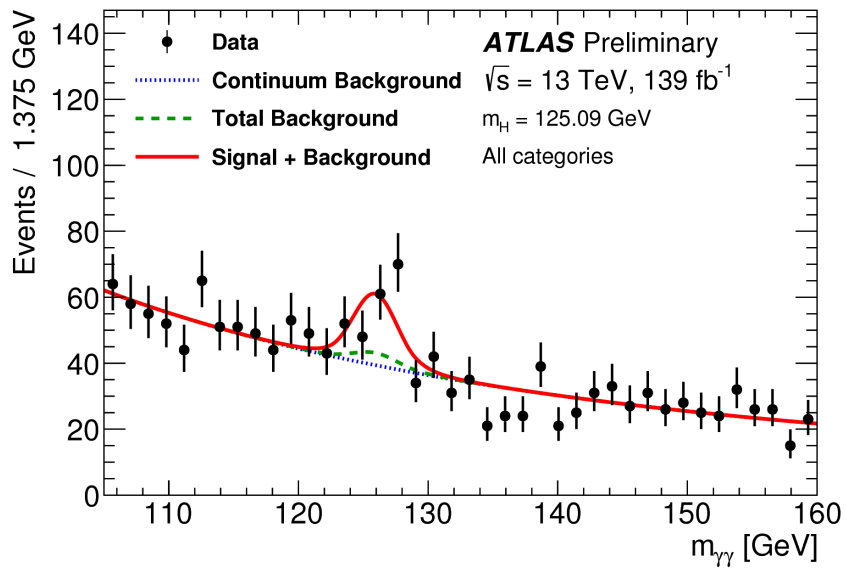


**Figure 2.8**  $t\bar{t}H$  production in the  $H \rightarrow \gamma\gamma$  decay mode [41]. The  $t\bar{t}H$  signal is indicated by a localised resonant bump in the red curve fitted to the data of the signal plus background shapes. The green dashed line represents the other Higgs production modes which provide a small contribution to the resonant peak.

A direct test of the Higgs-top quark coupling can be performed through the production of the Higgs boson in association with a top quark pair,  $t\bar{t}H$ . Evidence of this production was found in 2017 by the ATLAS collaboration using  $pp$  dataset collected at a centre-of-mass energy  $\sqrt{s} = 13 \text{ TeV}$  with an integrated luminosity of  $36.1 \pm 0.8 \text{ fb}^{-1}$  [15]. With dataset collected from the full of Run 2 from 2015 to 2018 with a luminosity of  $139 \text{ fb}^{-1}$  at  $\sqrt{s} = 13 \text{ TeV}$ , the observed(expected)  $t\bar{t}H$  production significance is  $4.9(4.2)$  standard deviations (Figure 2.8). The measured total  $t\bar{t}H$  production cross-section at  $\sqrt{s} = 13 \text{ TeV}$  agrees with the prediction from the SM [41].

## 2.9.2 Higgs Couplings to Particles

According to Equation 2.21, the couplings between the Higgs boson and fermions are linearly proportional to fermion masses. The measurements results are consistent with the prediction from the SM as shown in Figure 2.9.

## 2.9.3 CP Properties of Higgs Boson

To investigate the CP properties of Higgs boson, a mathematical description of the CP-mixing Higgs boson in [40] is expressed as

$$\mathcal{L} = -\frac{m_t}{v}(\bar{\psi}_t \kappa_t (\cos \alpha + i \sin \alpha \gamma_5) \psi_t) H \quad (2.25)$$

where  $\kappa_t$  is the top-Yukawa coupling parameter,  $\alpha$  is the CP-mixing angle. In the SM case,  $\kappa_t = 1, \alpha = 0$ ; in CP-odd case,  $\alpha = 90^\circ$ . Similar to Equation 2.23,  $\alpha$  is equivalent to  $\phi$  and  $\kappa_t$  determines the cross-section or magnitude of the  $t\bar{t}H$ .

Measurements of the CP-mixing angle,  $\alpha$ , could reveal the CP properties of Higgs boson. The data in reference [40] was taken with ATLAS detector at  $\sqrt{s} = 13$  TeV with an luminosity of  $139 \text{ fb}^{-1}$ . The results place constraints on a pure CP-odd coupling between the Higgs boson and top quark at  $3.9\sigma$ , and CP-mixing angle  $|\alpha| > 43^\circ$  is excluded at 95% CL. This means a pure CP-odd Higgs has been ruled out at 95% CL. Higgs boson will only exhibit a pure CP-even property or a CP-mixed property with  $< 26\%$  of CP-odd Higgs.

## 2.10 Summary

The theoretical perspectives of the Higgs boson have been discussed in this chapter. Properties of the Higgs boson need to be precisely measured to test the SM as well as giving us a gateway of probing BSM. One of the most interesting physics processes to investigate is the  $t\bar{t}H$ . Both the top-Yukawa coupling and CP properties of the Higgs boson can be measured in this process (discussed in Chapter 4). Many of the current and proposed experiments such as the LHC and CLIC started researches into  $t\bar{t}H$ . In the next Chapter, experimental apparatus used for this research including accelerators and detectors will be discussed.

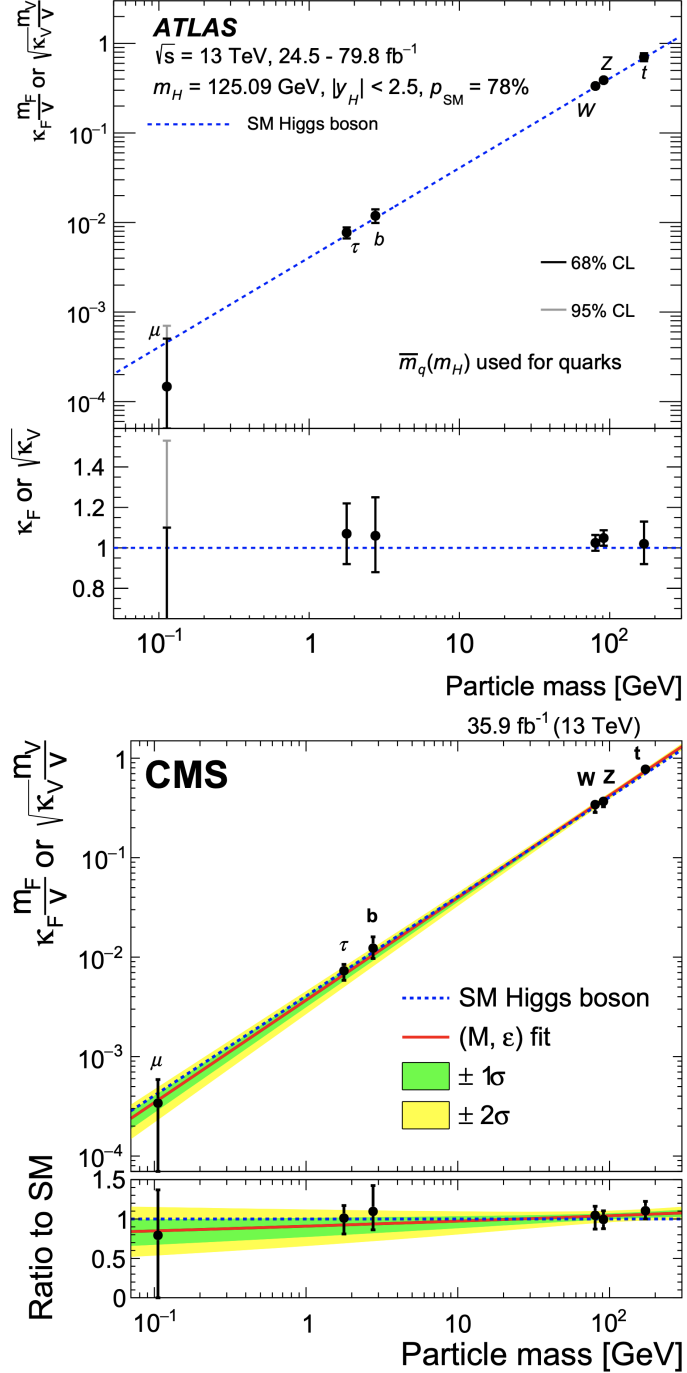


**Figure 2.9** Top (ATLAS): Reduced Higgs boson coupling strength modifiers  $\kappa m/v$  for fermions ( $F$ ) and  $\sqrt{\kappa} m/v$  for bosons ( $V$ ) as a function of particle masses ( $m_F$  or  $m_V$ ). The SM prediction is indicated by blue dotted line. The black error bars represent 68% CL intervals and grey error bars represent 95% CL intervals [13]. Bottom (CMS): Similar results have also been produced by CMS [14]

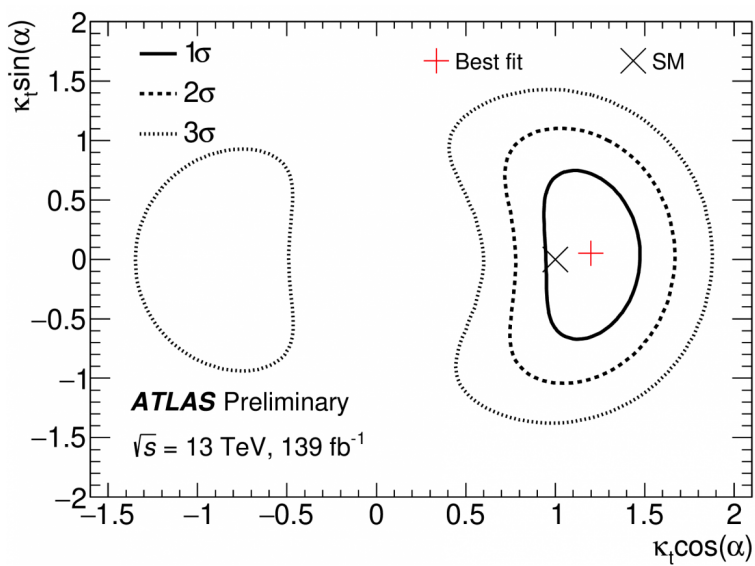


**Figure 2.10** Likelihood contours for  $\kappa_t \cos \alpha$  and  $\kappa_t \sin \alpha$  with gluon-gluon fusion and  $H \rightarrow \gamma\gamma$  (Equation 2.25) [40].

# Chapter 3

## The Particle Microscopes

### 3.1 The Particle Microscopes

Many of the unanswered questions about the Universe are hidden inside the subatomic world. One of the ways to reveal the nature of our Universe is by smashing two extremely high energetic particles. Modern colliders typically consist of an accelerator and a detector. The accelerator can accelerate particles close to speed of light with extremely high energy. Particles will then be brought to collision at an interaction point. After collisions, many of the byproducts will decay shortly after being produced and a detector can be used to capture these fleeting moments.

The most common particles used for higher energy collisions are hadrons (mainly protons) and electrons/positrons. Both of protons and electrons/positrons are charged particles and therefore can be accelerated with an electric field. However, due to huge mass difference ( $m_p = 938.28 \text{ MeV}/c^2$ ,  $m_e = 0.51 \text{ MeV}/c^2$ ) [27], much higher energy can be achieved by accelerating protons compared to electron/positron due to energy loss in synchrotron radiation. This allows a proton collider to reach a much higher collision energy in order to reach the limit of current energy scale and to explore new physics. In contrast, electron-positron collider has a lower collision energy but measurements could be made with higher precision as the experimental environment is cleaner for analysis Table 3.1.

Hadron colliders accelerate particles in a circular path such as the current world largest particle collider, the *Large Hadron Collider* (LHC) [43]. With circular

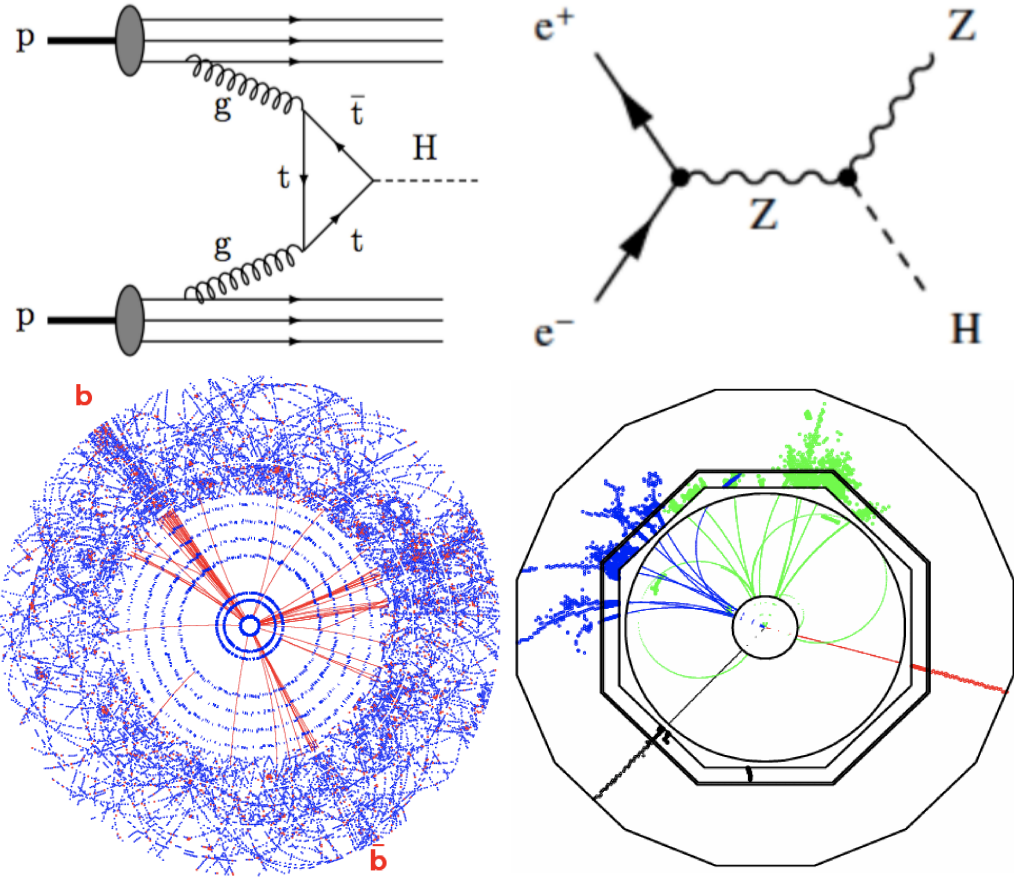


**Figure 3.1** Major Feynman diagrams of single Higgs boson production in proton colliders (left) and  $e^+e^-$  colliders (right) [42] with corresponding event displays.

	$p - p$ collisions	$e^+e^-$ collisions
Cross-section	large cross-section → high event rate	small cross-section → low event rate
Initial state	proton composites of quarks → initial state unknown → limited precision	$e^+e^-$ are point-like particles → initial state well defined → high precision
Backgrounds	high rate of QCD backgrounds → complex triggering system → high levels of radiation	clean environment → trigger-less readout → low levels of radiation

**Table 3.1** Advantages and disadvantages of proton colliders and  $e^+e^-$  colliders. Initial state includes  $\sqrt{s}$  and polarisation.

geometry, particles can be accelerated to very high energies up to TeV scale as this can be done over a much longer distance to build up the energy. However, energy will be lost during circular acceleration as charged particles will emit synchrotron radiation as they move along bent paths. The energy loss from this

effect is inversely proportion to the mass to the 4<sup>th</sup> power of the particles.

$$\Delta E \propto \frac{1}{R} \left( \frac{E}{m} \right)^4 \quad (3.1)$$

This means lighter particles will suffer more from the energy loss in the circular accelerators and cannot be accelerated to higher energies. An example of this is *LEP* (Large Electron-positron Collider) which used to occupy the same tunnel as the LHC but could only accelerate electrons ( $0.51 \text{ MeV}/c^2$ ) up to 104.5 GeV per beam [44], whilst current LHC can accelerate protons up to 7 TeV per beam. The collision energy of the proposed future  $e^+e^-$  collider, the *Future Circular Collider* (FCC) in particular *FCC-ee* (electron-positron collider), with a circumference of 100 km will also be limited to 365 GeV by synchrotron radiation as shown in Figure 3.3 [45, 46].

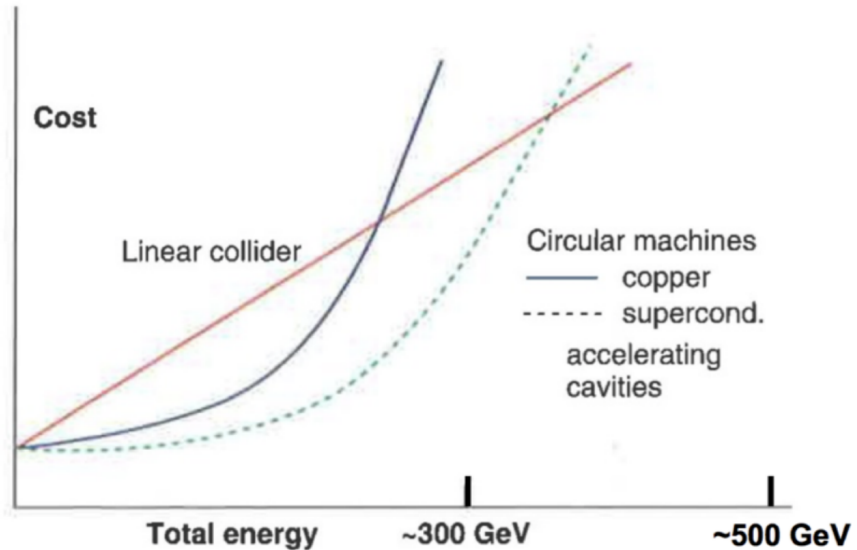


**Figure 3.2** *Cost vs energy for proposed  $e^+e^-$  colliders [47]. Circular collider loses energies from synchrotron radiation while accelerating electrons and the amount of cost to sustain the energy grows exponentially. Linear collider does not suffer from the same issue, the energy and cost are linearly dependent on the acceleration tunnel length.*

Electrons/positrons can also be accelerated linearly such as the *Stanford Linear Collider* at SLAC and the proposed future linear colliders *International Linear Collider* (ILC) and *Compact Linear Collider* (CLIC). Although the event rate would not be as high as circular lepton colliders, the collision energy can easily surpass the limit of circular lepton colliders by increasing the length of tunnel linearly (as

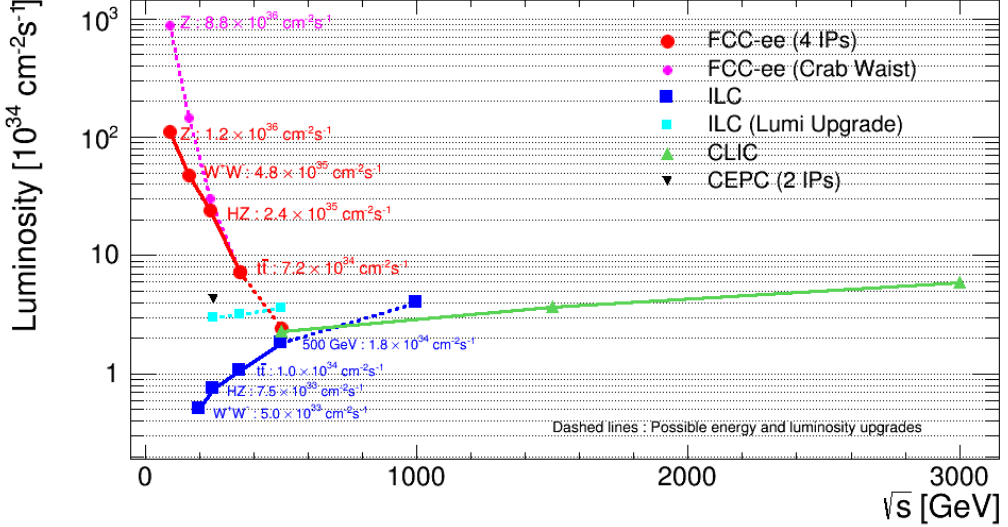


**Figure 3.3** *Luminosity vs energy for proposed  $e^+e^-$  colliders [48]. Circular colliders compared to linear colliders have relatively large luminosity but low in collision energy due to synchrotron radiation.*

shown in Figure 3.2&3.3). The collision energy of ILC could reach up to 1 TeV with 30–50 km in length [49], more than 10 times as long as the 50 GeV machine at SLAC (3.2 km) [50]. Meanwhile CLIC could even reach 3 TeV with 50 km with novel two-beam acceleration technique. Comparison between ILC and CLIC is shown in Table 3.2. The high-energy linear colliders will be able to provide a clean environment for precision measurements (as illustrated in Figure 3.1). It also opens up a discovery window to search for potential BSM physics.

	ILC	CLIC
Energy stages (GeV)	250-1000	380-3000
Acc. Gradient (MV/m)	35	72/100
Main linac tech	Super-conduct	Normal-conduct
Bunch spacing (ns)	554	0.5
Polarisation	$e^-/e^+$	$e^-$
Total luminosity ( $\text{cm}^{-2}\text{s}^{-1}$ )	$1.4 \times 10^{34}$	$1.5 \times 10^{34}$
Length (km)	20	11-50
Project timeline (years)	31	27
Beamstrahlung photon/electron	1.9	1.5

**Table 3.2** *Comparison of key parameters between linear  $e^+e^-$  colliders ILC and CLIC. [51]*

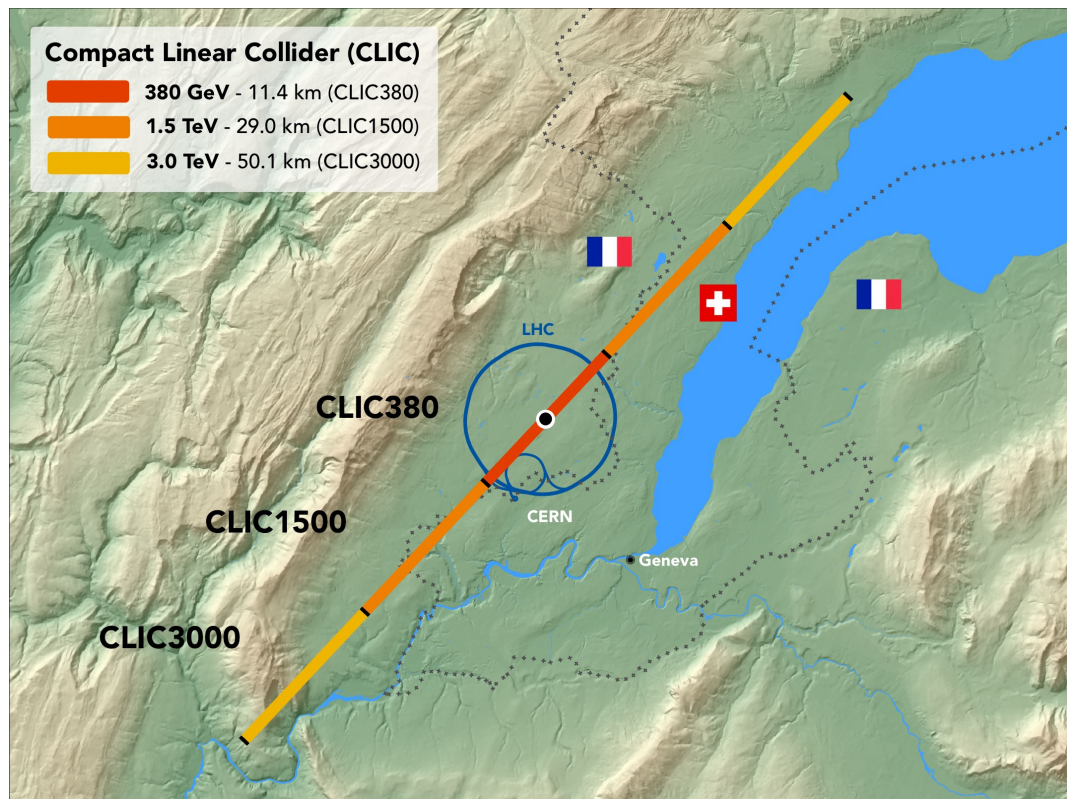
## 3.2 Compact Linear Collider



**Figure 3.4** Overview of the proposed CLIC machine at CERN. Credit: CERN.

The Compact Linear Collider (CLIC) is a proposed multi-TeV future linear  $e^+e^-$  collider designed to be built at CERN [12] (Figure 3.4). The accelerator would span a length of 11 to 50 km with three different centre of mass energy stages 380 GeV, 1.5 TeV and 3 TeV [52]. At CLIC, the accelerating gradient is designed to have 100 MV/m which means an electron will gain 100 MeV as it is accelerated through 1 m. The bigger the acceleration gradient, the smaller distance is needed for any given energy. As a comparison, accelerating gradient at ILC is 35 MV/m. The accelerating gradient is very important for linear colliders. For circular machines, particles can gain more energy by looping more turns inside the tunnel.

CLIC is in the “Development Phase” as shown in Figure 3.5 with ongoing research and development from both the CLIC accelerator and the CLIC detector and physics teams. There is extensive effort into studies of the physics potential of the CLIC experiment [53, 54].



2013 – 2019

**Development Phase**

Development of a project plan for a staged CLIC implementation in line with LHC results; technical developments with industry, performance studies for accelerator parts and systems, detector technology demonstrators

2020 – 2025

**Preparation Phase**

Finalisation of implementation parameters, preparation for industrial procurement, pre-series and system optimisation studies, technical proposal of the experiment, site authorisation

2026 – 2034

**Construction Phase**

Construction of the first CLIC accelerator stage compatible with implementation of further stages; construction of the experiment; hardware commissioning

2020

2026

2035

Update of the European Strategy for Particle Physics

Ready for construction

First collisions

7 years

27 years

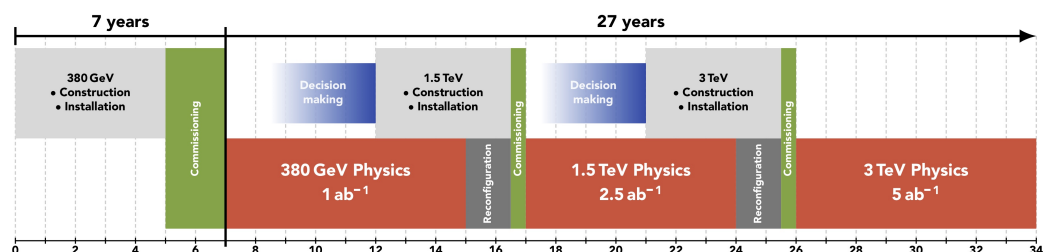


**Figure 3.5** Map of the CLIC program (top) with timeline of development, preparation and construction timeline and (middle) physics program with collision energy and corresponding luminosity timeline (bottom) [55].

### 3.2.1 CLIC Physics Program

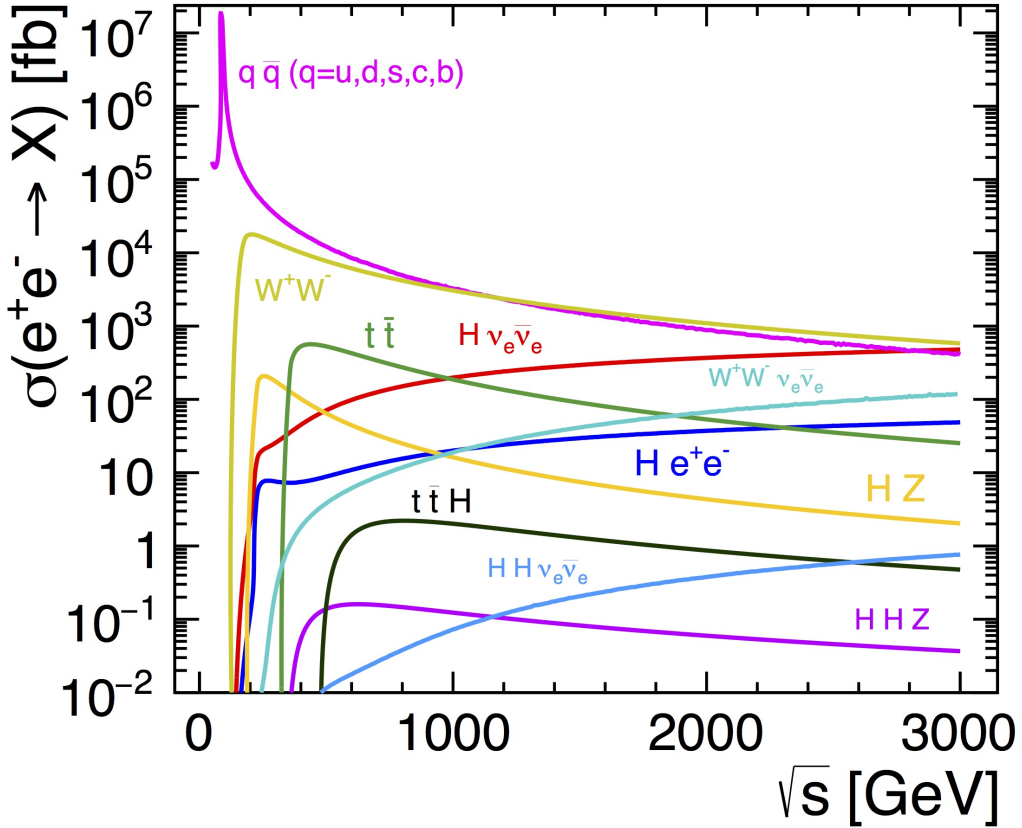


**Figure 3.6** The centre-of-mass dependencies of the cross-sections for the main Higgs production processes at an  $e^+e^-$  collider [55].

The different centre of mass energy stages of the proposed CLIC accelerator are optimised for different physics processes as illustrated in Figure 3.6. At the first stage of 380 GeV, with an integrated luminosity of  $1 \text{ ab}^{-1}$ , abundant top quarks and Higgs bosons can be produced via various processes such as  $t\bar{t}$  and  $HZ$ , which allow a  $t\bar{t}$  threshold scan as well as model independent measurements of Higgs cross-section to be performed [53]. A second stage reaches a centre of mass energy of 1.5 TeV providing a better sensitivity to rare Higgs processes such as Higgs production with a top pair ( $t\bar{t}H$ ) with an integrated luminosity of  $2.5 \text{ ab}^{-1}$ . The last stage of 3 TeV with an integrated luminosity of  $5 \text{ ab}^{-1}$  is achieved with extending its total length to 50 km. More rare Higgs processes can be accessed with precision measurements, examples are the  $HHWW$  quartic coupling and the Higgs self-coupling [52]. The higher energy stages are adapted to the results

and discoveries from the LHC (HL-LHC) and from the first stage of CLIC (shown as “Decision making” in Figure 3.5). If hints of new physics were observed, CLIC can change some of the accelerator parameters such as beam polarisation and collision energy to focus on studying the specific physics events.

### 3.2.2 CLIC Accelerator

CLIC uses a novel acceleration technology, a two beam acceleration scheme, to reach TeV-level energy stages [56]. Electrons and positrons beams (*main beams*) are accelerated by the two linear accelerators in opposite directions as shown in Figure 3.7. Two beams are then collided at the *Interaction Point (IP)* near the centre of the CLIC machine.

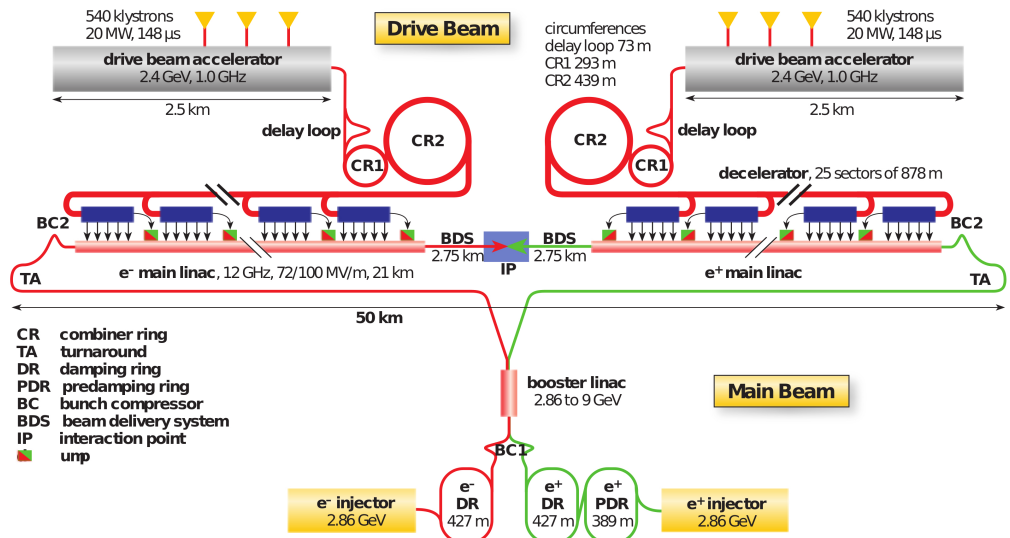


**Figure 3.7** Conceptual layout of CLIC at the highest energy stage  $\sqrt{s} = 3$  TeV [55]. A two beam acceleration scheme is built in both direction of the beam.

The main beams are structured in a bunch of trains as shown in Figure 3.8. The bunch trains are separated by 20 ms in time, resulting in a frequency of 50 Hz for the CLIC accelerator. Inside each bunch of trains are the 312 trains of electrons or positrons which are spaced 0.5 ns between each train (*bunch spacing*).

The acceleration gradient for CLIC is designed to be 100 MV/m to achieve the highest energy whilst minimising the length of the accelerator. The main beams are boosted in the copper accelerating cavities by creating a high field through

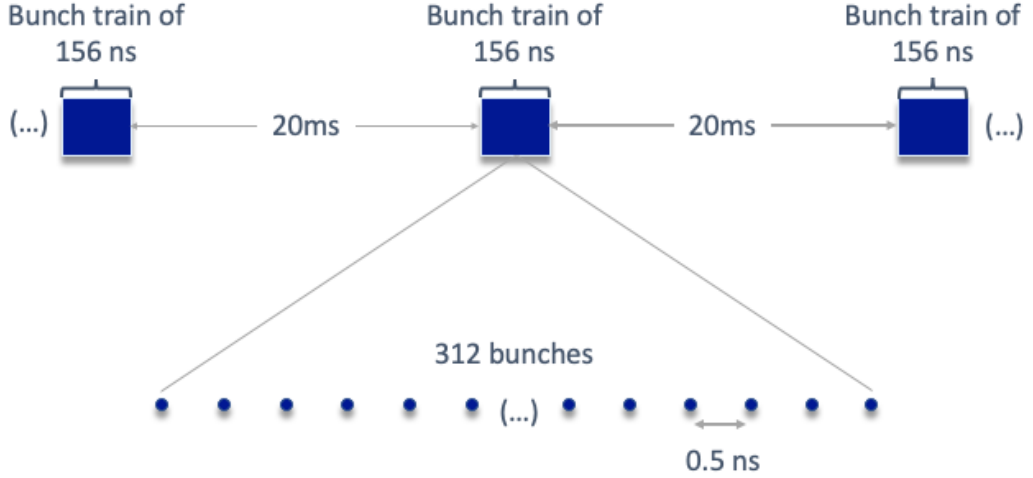


**Figure 3.8** Schematic sketch of the CLIC beam structure (not to-scale). Each bunch train is separated by 20 ms and each train consists of 312 bunches of electrons which are separated by 0.5 ns.

feeding *Radial Frequency* (RF) power with a frequency of 12 GHz [57].

A low-energy but high-intensity drive beam using the traditional Klystron technologies runs in parallel with each of the main beams (Figure 3.7). It is then fed into a sequence of *Power Extraction and Transfer Structures* (PETS) which can decelerate the drive beams and extract their energy. The RF energy is produced from this process and is transferred to the copper cavities to accelerate the main beams via waveguides.

The main beams are strongly focused at IP to produce a high luminosity. At a centre of mass energy of 3 TeV, the beams are focused to a transverse size of  $\sigma_x/\sigma_y \sim 40 \text{ nm}/1\text{nm}$ . Strong electromagnetic fields are created at the IP by these dense beam particles at high energy and cause the beam particles to emit radiations resulting *Bremsstrahlung*. As a result, the centre of mass energy of these particles will be lower than nominal energy and creating a *luminosity spectrum* as shown in Figure 3.9.

The  $e^+e^-$  beam travels with the photons inside the beam pipe. *Beam-beam interactions* arise when the photons interact with each other or with the electric field generated from the opposing beam. The main backgrounds produced from this effect are the hadrons produced from photon collisions from opposing beams ( $\gamma\gamma \rightarrow \text{hadrons}$ ). Due to the choice of an opening angle of the beam pipe of  $> 10^{-2} \text{ rad}$ , these hadrons and incoherent electron positron pairs are the main

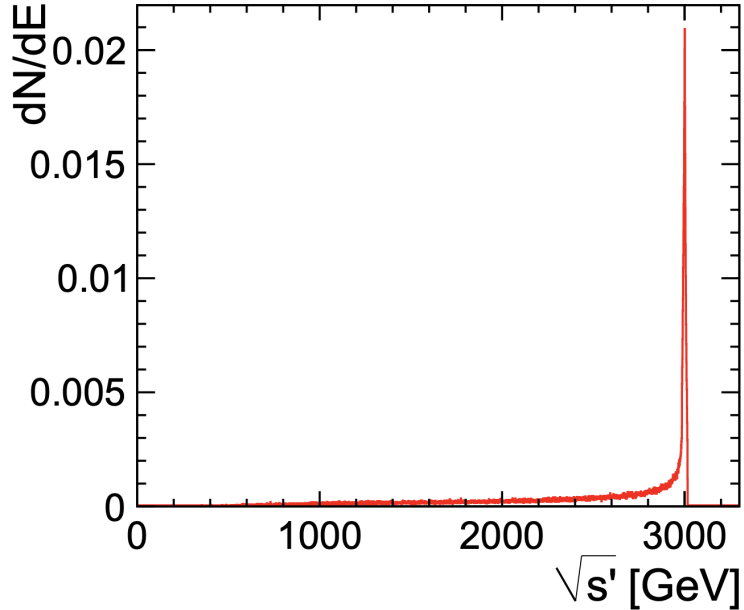


**Figure 3.9** The luminosity spectrum of CLIC at the highest energy stage with  $\sqrt{s} = 3$  TeV [58].

source of backgrounds that reach the detector region [59].

This high-rate of backgrounds can be suppressed by setting timing requirements to the CLIC detector and will be discussed in the following chapter.

### 3.2.3 CLIC Detector

CLIC\_ILD and CLIC\_SiD are the two detector concepts used for the CLIC physics studies [53, 54] adapted from the ILD [61, 62] and SiD [60, 62] detector concept for the ILC. CLIC detector concepts are optimised for 3 TeV and the designs modification is motivated by the high-energy collisions as well as the different beam conditions and the small bunch spacing. This thesis uses the CLIC\_SiD detector concept for the physics analysis and the description will be focused on the CLIC\_SiD. A schematic diagram is shown for CLIC\_SiD in Figure 3.10.

A silicon vertex detector is placed at the centre of the detector near the interaction point. This is covered by an all-silicon tracker which uses both pixel and strip detectors to track and identify charged particles that pass through.

Fine-grained electromagnetic and hadronic calorimeters (ECAL and HCAL) are

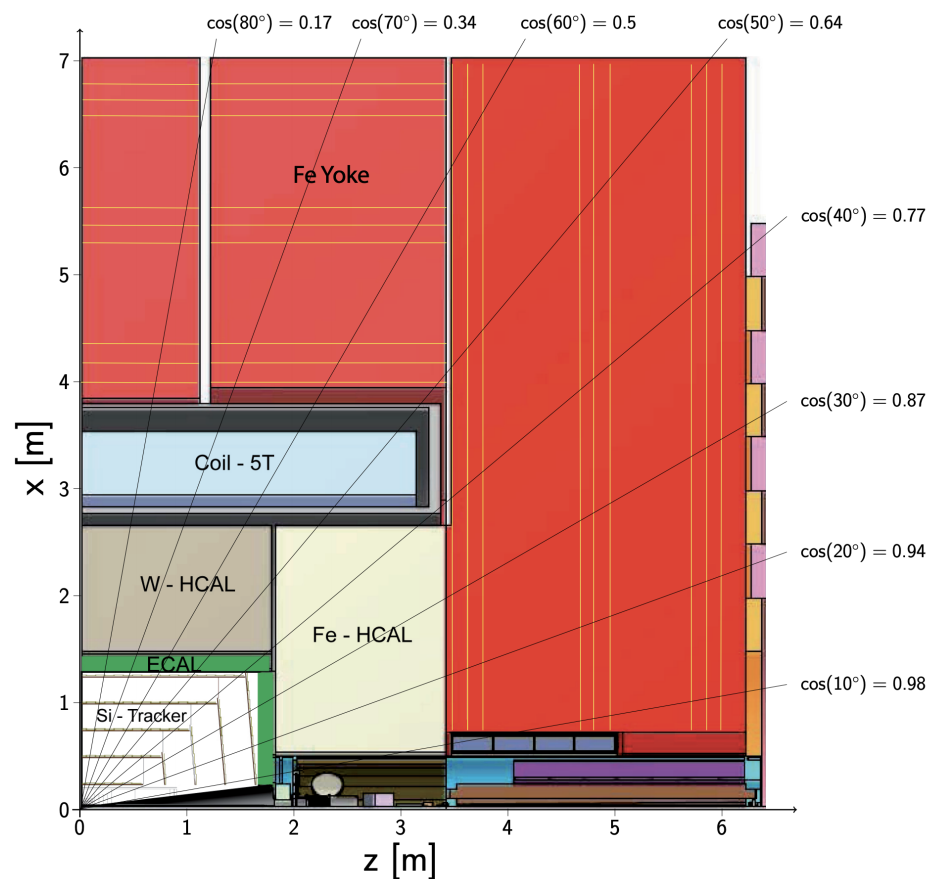
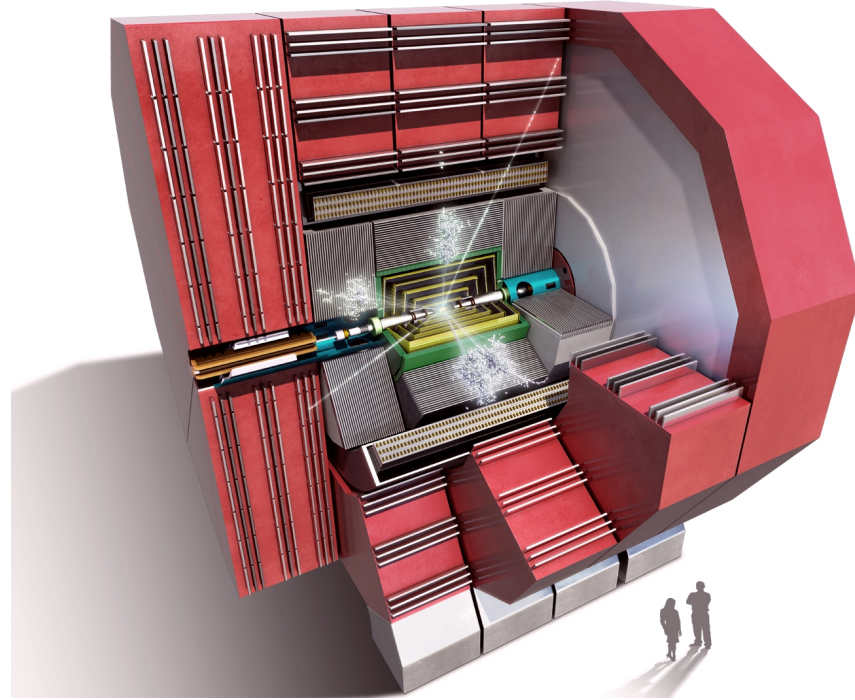


**Figure 3.10** Overview of the CLIC-SiD detector (top) and a schematic of the detector concept (bottom) [55, 60]

used for particle flow reconstruction. The ECAL and HCAL barrel uses tungsten as absorbing material, and HCAL endcap uses steel.

Outside the HCAL is the strong solenoidal magnet providing an axial magnetic field of 5 T inside CLIC-SiD. Momentum of the charged particles can be measured from the curvature of their tracks in the tracking system. Charged particles with low momentum will curve away before entering calorimeters under such high magnetic field to reduce occupancy in the detector.

Two compact ECALs, the luminosity calorimeter (LumiCal) and the beam calorimeter (BeamCal), are located in the forward region of the detector. The LumiCal is particularly useful in determining luminosity spectrum via measuring the energy and trajectory of electrons and positrons produced from Bhabha scattering [63]. The BeamCal measures forward electrons by extending the detector coverage up to 10 mrad in polar angle.

An iron return yoke, covering the whole detector, is instrumented with Resistive Plate Chambers (RPC). It is used to detect muons and support the calorimeters and the inner detectors.

## Detector Requirements of CLIC

The vertex and tracking system of CLIC-SiD provides a track momentum resolution of  $\sigma_{p_T}/p_T^2 \lesssim 2 \times 10^{-5} \text{ GeV}^{-1}$  needed for reconstructing high- $p_T$  charged leptons for accurate vertex reconstruction at high energy environment at CLIC [12]. Heavy flavour quarks, which have comparably long lifetimes, can be traced and reconstructed by this system. In a collision event, the primary vertex is defined as the collision point and the secondary vertex is defined at a displaced vertex where a particle starts to decay. The main requirement for the CLIC vertex detector is a precise measurement of the transverse impact parameter  $d_0$ , defined as the closest distance between the primary vertex and the reconstructed track.

The resolution of the transverse impact parameter  $\sigma_{d_0}$  is written as [12]

$$\sigma_{d_0} = \sqrt{a^2 + b^2 \cdot \text{GeV}^2/p^2 \sin^2 \theta}, \quad (3.2)$$

where  $p$  is the momentum and  $\theta$  is the polar angle.

For particles with high momenta at CLIC, the constant terms  $a$  and  $b$  dominate the impact parameter resolution and they are required to be  $\lesssim 5 \mu\text{m}$  and  $\lesssim 15 \mu\text{m}$  respectively [12].

Many of the physics processes at CLIC produce heavy flavour quarks in their final states, such as Higgs decays or top quark decays. These requirements on the impact parameters enable CLIC detector to perform flavour-tagging with clean separation of  $b$ -quark,  $c$ -quark and light-quark jets which is crucial for top-quark identification and background rejections. As shown in Figure 3.6,  $e^+e^- \rightarrow q\bar{q}$  ( $q = u, d, s, c, b$ ) is the most dominant process but considered as backgrounds in most of the physics analysis at CLIC. Some of the physics process such as  $t\bar{t}H$  has many jets in its final states, separating and identifying all the jets will significantly improve the significance of signal events and have a more precise measurement (discussed in Chapter 4).

Due to the relative large pixel size of traditional calorimeters, it is difficult to reconstruct particles within jets as particles are travelling very close to each other inside the calorimeters in high energy environment. CLIC uses fine-grained electromagnetic and hadronic calorimeters (ECAL and HCAL) which allows showers from individual particles to be separated. The particles can then be identified and tracked throughout the whole detector using particle flow reconstruction technique [64, 65]. Charged particles are measured most accurately in the tracker, photons are measured with good precision in ECAL and neutrons are measured less precisely in HCAL but only contribute to 10% of the jet energy measurements. This reconstruction technique yields optimal jet energy resolution. At CLIC-SiD, the jet resolution is  $\sigma_E/E \lesssim 3.5\%$  for isolated central light-quark jets with energy between 100 GeV and 1 TeV [54, 60].

## CLICdet

CLIC is developing its own detector model, CLICdet, as shown in Figure 3.11. It is optimised for the 3 TeV energy stage, where the backgrounds from beam-beam interactions are most challenging. The layout of CLICdet detector concept is based on full simulations with respect to the requirements from the experimental environment and the physics goals.

At the very centre of CLICdet is the vertex detector [66]. It comprises ultra-thin hybrid pixel sensors and uses air-flow cooling and power-pulsing to minimise the

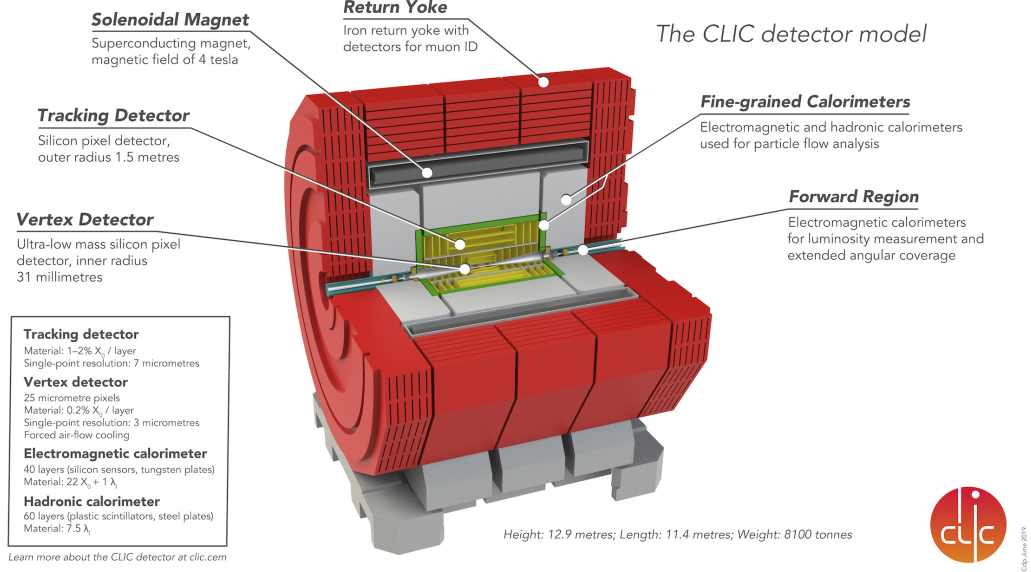


**Figure 3.11** Overview of the CLICdet [55]

material budget. Next to the vertex detector is the tracking system which is fully based on silicon pixel and strip technology. Fine-grained calorimetry is designed to enable particle flow analysis techniques. A 4 T solenoidal magnetic field is embedded around both calorimeters to minimise the material scattering. It is a cheaper option compared to the ATLAS detector where the magnet is built inside calorimeters. The outermost region is covered by an iron yoke to provide magnetic flux return and to measure particles that penetrated through.

The CLICdet has a similar layout as the CLIC-ILD and CLIC-SiD models. However, key parameters of CLICdet are different to other detector concepts, which are designed specifically to fit the CLIC program. Comparison of key parameters of different CLIC detector concepts can be found in [66].

### 3.3 Summary and Outlook of Future Colliders

The LHC is currently the most precise particle microscope that have ever built. Physicists continue to push the limit on extending our ability to understand the Universe. The proposed  $e^+e^-$  collider, CLIC, is expected to exhibit a cleaner analysis environment and make more precise measurements than the LHC or HL-LHC. It will exceed the collision energy limit of circular  $e^+e^-$  colliders by having a

linear accelerator powered with two drive beams. The collision energy is expected to be up to 3 TeV with an acceleration gradient of 100 MV/m. Many physics processes will be able to accessed at such high energy. Vertex detector is one of the most important parts for precision measurements. It defines the performance of flavour-tagging, which is a one of the key tools in physics analysis at CLIC. Potential physics processes motivate the design of CLIC machine. Meanwhile, performance of the future machine needs to be evaluated with benchmark studies to see its potential.

The next chapter will be using one of the most interesting physics processes,  $t\bar{t}H$ , to discuss the potential of a proposed linear  $e^+e^-$  collider, the CLIC, in precision measurements. Results will be compared with a  $pp$  collider, the LHC.

# Chapter 4

## Top - Yukawa Coupling and Higgs Boson CP Analysis

### 4.1 Top - Yukawa Coupling Measurement

Precision measurements of the coupling between the Higgs boson and the top quark could help us to gain a deeper understanding of the nature of Higgs boson, as well as the SM. The  $t\bar{t}H$  processes is a direct, and the most dominant, process to probe the coupling strength between the Higgs boson and top quarks. However, due to the large number of jets in the  $t\bar{t}H$  final state, it is crucial to identify each individual jet. Electron-positron colliders (such as CLIC), with a much cleaner background than the proton colliders (such as LHC), are more suitable for such precision measurements.

This chapter presents a precision measurement of the top - Yuakwa coupling in the  $e^+e^- \rightarrow t\bar{t}H$  process where  $H \rightarrow b\bar{b}$  at  $\sqrt{s} = 1.4$  TeV at CLIC. The analysis focuses on the 6 jets and 8 jets final states channels using particle flow techniques [64]. First, leptons are identified and the remaining particles are clustered into jets. These jets are then flavour-tagged to allow identification of  $b$ -quarks. Optimal selection are investigated to select leptons and to suppress the beam-induced backgrounds. Finally, a collection of variables are used as input to the BDT to select signals.

### 4.1.1 Analysis Strategy

The analysis strategy for the top-Yukawa coupling is briefly described below. SM Higgs bosons with mass of  $125 \text{ GeV}/c^2$  that decay into a pair of  $b\bar{b}$  ( $BR \simeq 56\%$ ) are considered. The top quark decays into a bottom quark and a  $W$  boson and the  $W$  boson subsequently decays into either quarks (68%) or leptons (32%) as shown in Figure 4.1. The search channels are classified according to number of charged leptons in their final state and is summarised in Table 4.1.

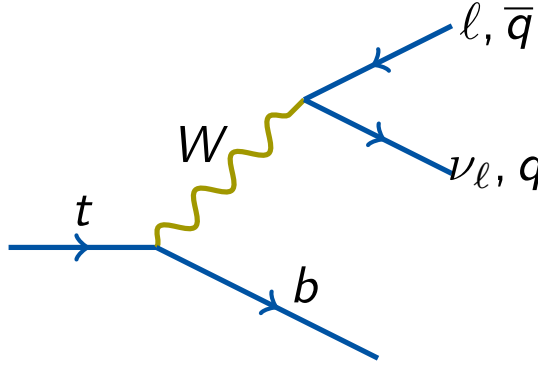


**Figure 4.1** Feynman diagram of the dominant decay product of the top quark and the subsequent  $W$  boson.

No. leptons	Process	Channel name	$BR$
0	$t\bar{t}H \rightarrow b\bar{b}qqqq + b\bar{b}$	Full-hadronic	46%
1	$t\bar{t}H \rightarrow b\bar{b}qql\nu + b\bar{b}$	Semi-leptonic	45%
2	$t\bar{t}H \rightarrow b\bar{b}\ell\ell\nu\nu + b\bar{b}$	Di-leptonic	9%

**Table 4.1** Searching channels classified using different number of leptons in the final states with corresponding branching ratio ( $BR$ ).  $q$ ,  $\ell$  and  $\nu$  represent quark, charged lepton and neutrino.

The di-leptonic channel is not considered in this analysis due to a much smaller cross-section. The procedure of the analysis is described as follow:

Particles that pass the lepton selection criteria are identified as leptons as described in Section 4.2. Each event is classified according to the number of charged leptons in its final state: events with 0 charged leptons are classified as fully-hadronic, events with 1 charged lepton are classified as semi-leptonic, and events with more than 1 charged lepton are be analysed further.

Particles that are not identified as leptons are clustered into specific number of

jets, 6 jets for semi-leptonic and 8 jets for full-hadronic. The  $k_T$  jet clustering algorithm [67] also identifies the incoming beam particles as jets. These jets are classified as “beam jets” and are removed from further consideration.

The **LCFIPlus** package [68] is used to perform flavour-tagging on jets as described in Section 4.6. Jets are combined to reconstruct the top quark,  $W^\pm$  and Higgs boson candidates. A multi-variant analysis using the **TMVA** package [69] is used to separate signal from backgrounds with selected variables as presented in Section 4.7.

### 4.1.2 Simulation Samples

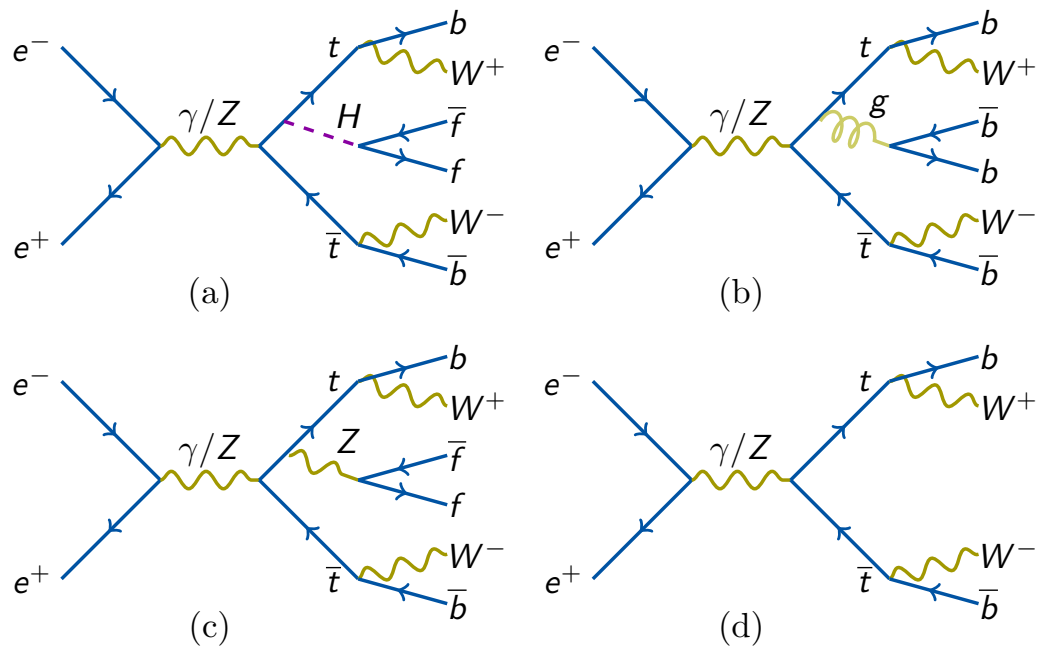


**Figure 4.2** Feynman diagrams of the backgrounds of  $e^+e^- \rightarrow t\bar{t}H$  where  $H \rightarrow b\bar{b}$ . (a) other decays of  $t\bar{t}H$  where  $H \not\rightarrow b\bar{b}$ , (b)  $t\bar{t}b\bar{b}$ , (c)  $t\bar{t}Z$  and (d)  $t\bar{t}$ .

All of the signal and background events are simulated with unpolarised beams. Hadronic signal events are simulated with 6 jets from  $t\bar{t}$  and 2  $b$ -jets from Higgs. Semi-leptonic signal events are simulated with 4 jets from  $t\bar{t}$  and 2  $b$ -jets from Higgs. Other final states of the  $t\bar{t}H$  system are considered as backgrounds. Irreducible backgrounds arise when the backgrounds have similar final states as the signal. These include  $t\bar{t}Z$  and  $t\bar{t}b\bar{b}$  that both have eight fermion final states as shown in Figure 4.2. The top quark in these processes radiates a  $Z$  boson or a hard gluon that can decay into a  $b\bar{b}$  pair. A significant background comes from

Process	Cross-section (fb)	Sample weight	Evt in 1.5 ab <sup>-1</sup>	Generator
$t\bar{t}H$ , 6 jets, $H \rightarrow bb$	0.431	0.03	647	Physsim
$t\bar{t}H$ , 4 jets, $H \rightarrow b\bar{b}$	0.415	0.03	623	Physsim
$t\bar{t}H$ , 6 jets, $H \not\rightarrow bb$	0.315	0.02	473	Physsim
$t\bar{t}H$ , 4 jets, $H \not\rightarrow b\bar{b}$	0.303	0.02	455	Physsim
$t\bar{t}H$ , 2 jets, $H \rightarrow b\bar{b}$	0.100	0.006	150	Physsim
$t\bar{t}H$ , 2 jets, $H \not\rightarrow b\bar{b}$	0.073	0.004	110	Physsim
$t\bar{t}Z$ , 6 jets	1.895	0.1	2843	Physsim
$t\bar{t}Z$ , 4 jets	1.825	0.1	2738	Physsim
$t\bar{t}Z$ , 2 jets	0.439	0.03	659	Physsim
$t\bar{t}b\bar{b}$ , 6 jets	0.549	0.03	824	Physsim
$t\bar{t}b\bar{b}$ , 4 jets	0.529	0.03	794	Physsim
$t\bar{t}b\bar{b}$ , 2 jets	0.127	0.008	191	Physsim
$t\bar{t}$	135.8	1.5	203700	PYTHIA

**Table 4.2** *Signal and background samples simulated for the analysis. Samples are simulated with unpolarised beams at  $\sqrt{s} = 1.4$  TeV and assuming a integrated luminosity of  $1.5 \text{ ab}^{-1}$ . All samples are simulated by assuming a Standard Model Higgs boson with  $125 \text{ GeV}/c^2$ . The first two rows are the  $t\bar{t}H$  signal channels. The number of jets refers to the decay of  $t\bar{t}$ . The event in  $1.5 \text{ ab}^{-1}$  is calculated from the sample weight and integrated luminosity.*

the six-fermion final state of  $t\bar{t}$  due to its huge relative cross-section compared to the signal. The  $t\bar{t}$  samples are generated using PYTHIA [70], other samples are simulated using Physsim [71]. ISR effect and CLIC luminosity spectrum are included. Details of the simulated samples can be found in Table 4.2.

## 4.2 Event Reconstruction

Output from the Monte Carlo simulations are processed through the **Marlin** framework [72]. **Marlin** is a reconstruction and analysis tool both for Monte Carlo-based physics analysis and for optimisation of detectors. First, the simulated tracks and calorimeter hits are digitised. Tracks are then reconstructed using the **MarlinReco** package [73] in **Marlin**. The reconstructed tracking information is used by **PandoraPFA** [74] to reconstruct particle flow objects (PFOs), as described in the following sections.

### 4.2.1 PandoraPFA

PandoraPFA is a reconstruction package that follows the *particle flow* concept [74] where every particle in a jet is identified and reconstructed. The energy of each particle is then extracted from the highest-resolution detector measurements, i.e. energies of charged particles are taken from the tracking information, whereas energies of neutral particles are taken from the calorimeter information.

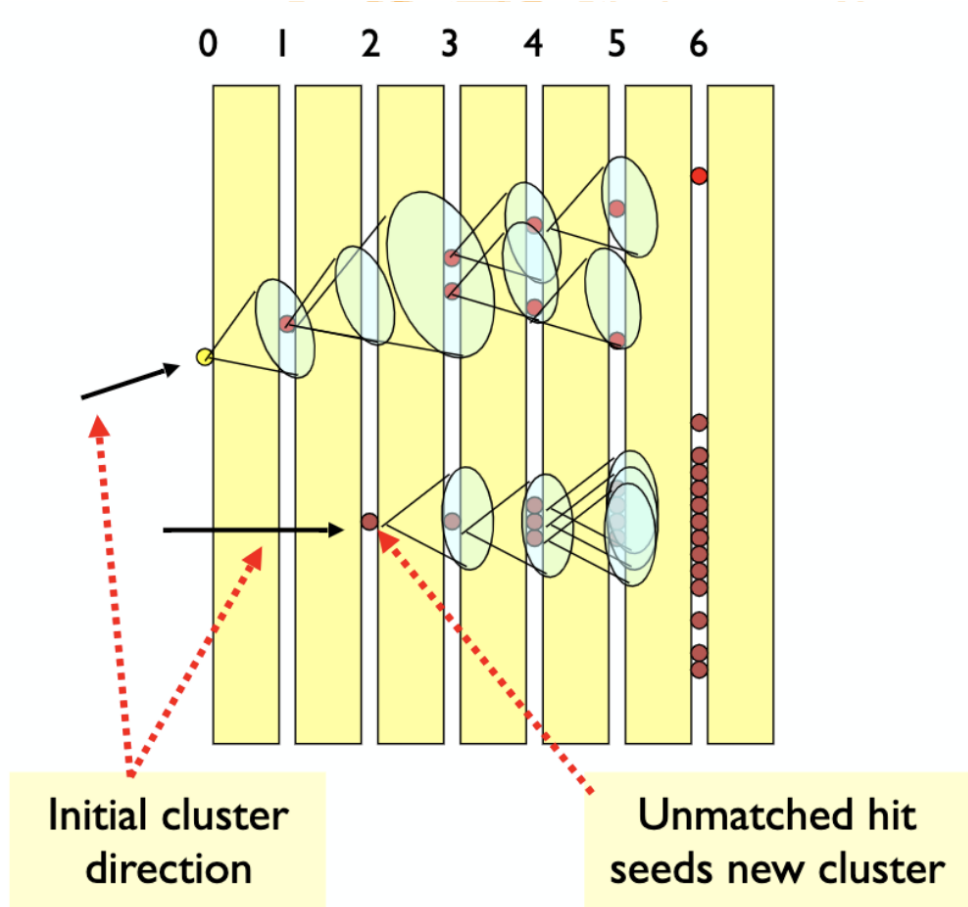


**Figure 4.3** Illustrations of PandoraPFA cone-based clustering algorithms. Picture taken from [75].

Cone-based clustering algorithms are used in PandoraPFA. These algorithms gather hit information from the calorimeters and group them into clusters. The division of energy deposits into particles starts by using a simple cone-based clustering algorithm. The clusters are seeded by projections of the reconstructed tracks pointing to the surface of the calorimeter. Starting at the innermost calorimeter layers, and working outwards, each calorimeter hit is considered in turn. If the hit lies within the cone defined by the existing cluster, it is added to the cluster; if the hit is unmatched, it is used to form a new cluster. This is

illustrated in Figure 4.3.

Once the clusters are defined, the Pandora track–cluster association algorithm looks for consistency between the clusters and the tracks. Tracks and clusters are matched by looking for close proximity between cluster and track positions, consistent track and initial cluster directions, and consistent track momentum and cluster energy.

A re-clustering step takes place to resolve ambiguities when several particles overlap and are initially reconstructed as one cluster. Using tracking and topological information, the re-clustering typically results in splitting the initial cluster into two or more lower-energy clusters.

Finally, particle flow objects (PFOs) are defined from the reconstructed tracks and their final associated clusters. PFOs can also be defined from cluster information without any associated tracks.

These **PandoraPFOs**, which are the final output of the event reconstruction, are used for subsequent analysis.

### 4.3 Beam-Induced Background Suppression

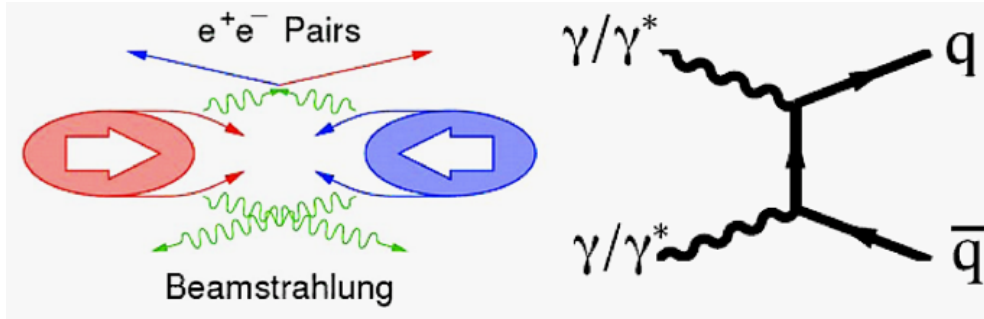


**Figure 4.4** Illustrations of beam induced backgrounds. (Left) Beamstrahlung and (Right)  $\gamma\gamma \rightarrow$  hadrons interactions.

At  $\sqrt{s} = 1.4$  TeV, there are, on average, 1.3  $\gamma\gamma \rightarrow$  hadrons interactions per bunch crossing occurring at the interaction point (Figure 4.4) [12]. They tend to have low transverse momenta and small angle to the beam axis. This background can deposit energies up to 200 GeV in the calorimeters. Although the majority of the particles have a very small angle to the beam axis, they still deposit approximately 20 GeV into the calorimeters. This effect will cause

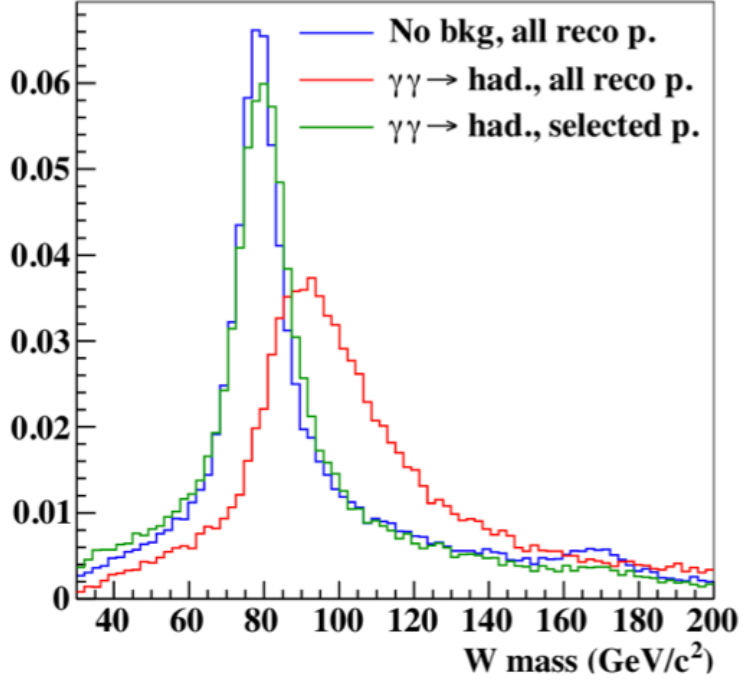


**Figure 4.5** Plot of reconstructed  $W$  mass and effects from  $\gamma\gamma \rightarrow \text{hadrons}$  interactions. A truth-matched reconstructed  $W$  mass without any backgrounds is shown in blue line. With an addition of  $\gamma\gamma \rightarrow \text{hadrons}$  interactions, the reconstructed  $W$  mass is plotted in red line. With timing and momentum cuts as well as background suppression, the reconstructed  $W$  mass is shown in green line.

an overestimation of the jet energy and smear the reconstructed hadronic  $W^\pm$  invariant mass distribution ( $M_{W_{qq}}$ ) as shown in Figure 4.5. To reduce such background, timing and momentum cuts are imposed on the reconstructed `PandoraPFO` objects (`TightSelectedPandoraPFOCollection`). A time window of 10 ns following the physics event is applied to the hits of the background event and physics event. This is to account for the expected detector timing resolution and integration times. All the hits within the time window are then proceeded to the reconstruction. The combination of timing and momentum cuts enables the background from  $\gamma\gamma \rightarrow \text{hadrons}$  to be reduced from 19 TeV per bunch train to approximately 100 GeV per reconstructed physics event. An illustration of the effect of this selection is also shown in Figure 4.6. Details of this background suppression can be found in [58].

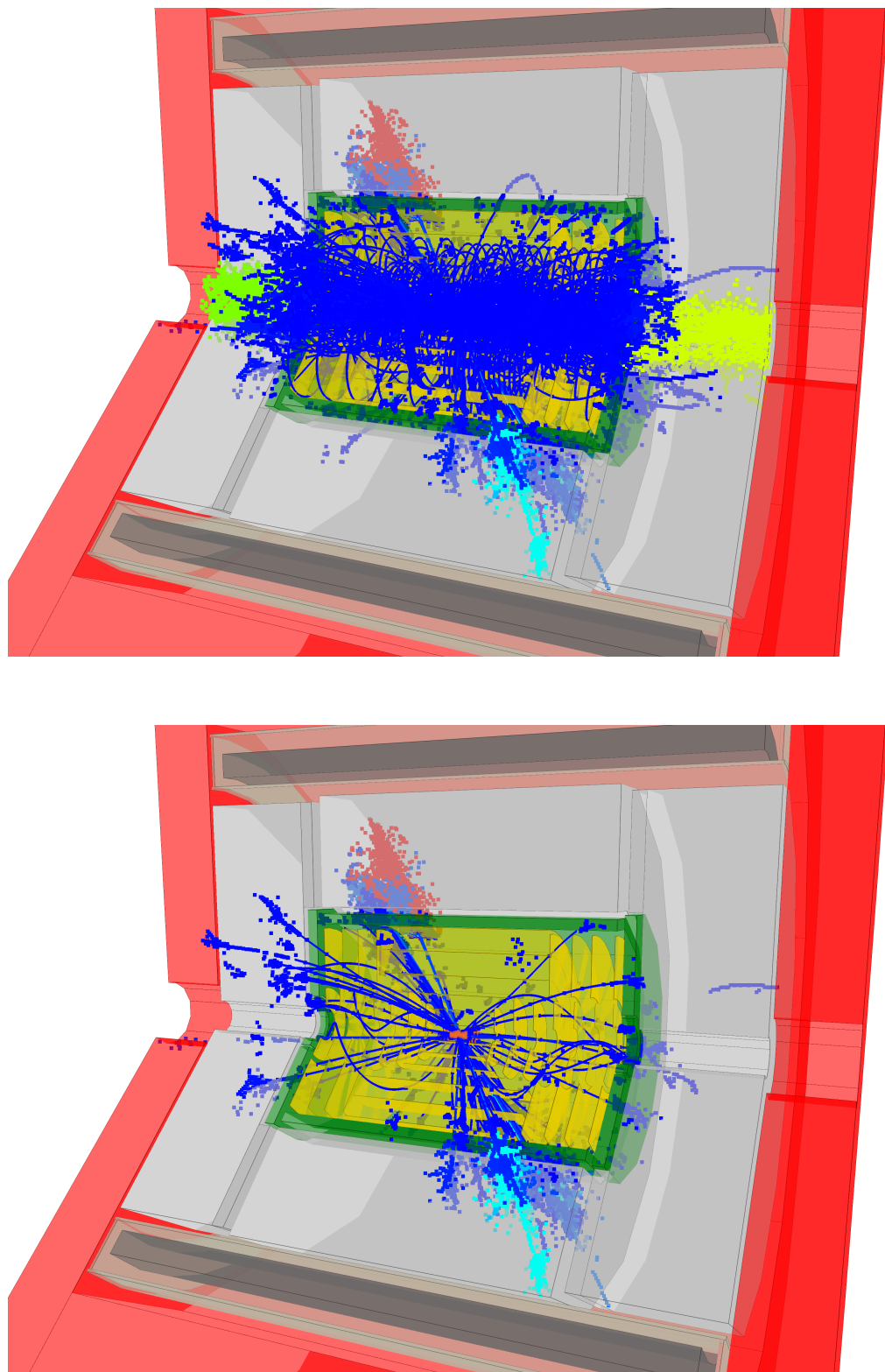


**Figure 4.6** Event display of  $t\bar{t}$  production at 3 TeV at CLIC. (top) Before and (bottom) after timing and momentum cuts as well as background suppression.

## 4.4 Lepton Identification

To classify the channels, leptons from  $W^\pm$  decays need to be identified and reconstructed from the events. The tau lepton decays rapidly before it reaches the detector due to its short lifetime and therefore is treated using a separate method. Firstly, isolated leptons (electrons and muons) are searched for by using a combination of impact parameter, track energy, calorimeter energy and isolation information. Then tau leptons are searched for by investigating the high-energy low-multiplicity jets that are isolated in the detector. The properties of the reconstructed leptons from  $W^\pm$  decays are determined by using the truth-matching method that matches generated particles with the reconstructed particles by using generator-level information.

### 4.4.1 Impact Parameter

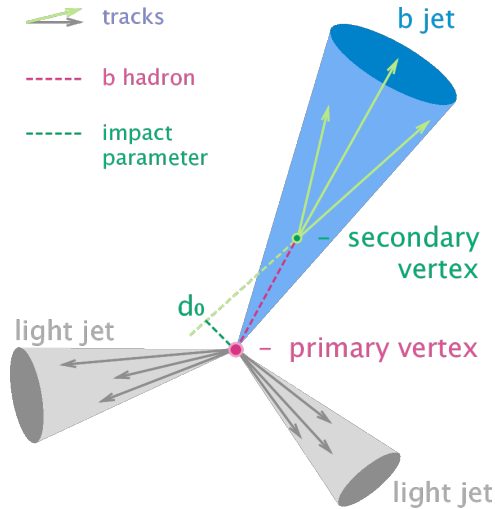


**Figure 4.7** Diagram of  $b$ -jet decay at a displaced vertex with indication of impact parameter,  $d_0$ .

Top quarks and  $W^\pm$  bosons have a very short lifetime, this causes electron and muons from the  $W^\pm$  decays appear to originate from the primary vertex (PV) of the event, whereas the decay products of the top quark and tau leptons from  $W^\pm$  originate at a displaced vertex due to their longer lifetime. An illustration of this effect is shown in Figure 4.7. This effect can be studied using the impact parameter (IP) which parameterises the relation between a track and the PV. The 3D IP is defined as

$$R_0 = \sqrt{Z_0^2 + d_0^2}, \quad (4.1)$$

where  $Z_0$  is the longitudinal component and  $d_0$  is the radial component. Isolated leptons tend to have relatively smaller impact parameters compare to particles from showers within jets and tau decay products. By constraining the 3D IP, the isolated leptons can be separated. From Figure 4.8, it is concluded that  $Z_0$ ,  $d_0$  and  $R_0$  are required to be less than 0.05 mm to separate out the isolated leptons.

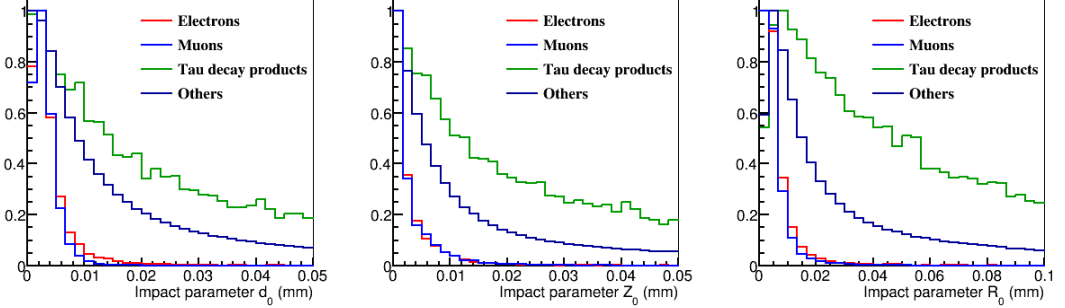


**Figure 4.8** Impact parameter distribution of truth-matched reconstructed charged leptons (a) radial component, (b) longitudinal component and (c) combined 3D IP for electrons (red), muons (blue), tau decay products (green) and all other reconstructed particles (black) that are not truth-matched to a lepton. Semi-leptonic  $t\bar{t}H$  sample is used.

#### 4.4.2 Track Energy and Calorimeter Energy

The reconstructed track energies of electrons and muons from  $W^\pm$  decays are typically within the range of 50 - 350 GeV (Figure 4.9 (left)), which are much larger than the energy of particle inside jets. Although the decay products of tau leptons do not have as high energy as the other two leptons, they are still significantly more energetic than other particles from showers within jets.

To distinguish leptons from hadrons, we look at the energy deposited in the ECAL and HCAL:

$$R_{CAL} = \frac{E_{ECAL}}{E_{ECAL} + E_{HCAL}}. \quad (4.2)$$

For example, it is likely to be an electron or photon if  $R_{CAL} \simeq 1$ . Although muons are detected by the iron yoke in the outmost layer of the detector, they still deposit a minimum amount of ionisation energy throughout the calorimeters which causes the peak around  $R_{CAL} \simeq 0.2$  (Figure 4.9(right)). Tau lepton shares a similar shape in  $R_{CAL}$  with hadrons as its decay products can be either leptonic or hadronic. This makes taus harder to be identified using this method. Therefore, the isolated leptons are selected using deposited calorimeter energies with  $R_{CAL} > 0.9$  and  $0.05 < R_{CAL} < 0.3$ .

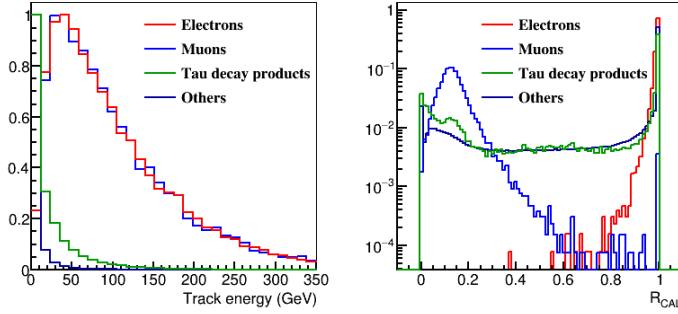


**Figure 4.9** (Left) Reconstructed track energies of truth-matched isolated charged leptons, tau decay products from  $W^\pm$  decays and other reconstructed particles which are not truth-matched to a simulated lepton. (Right) Calorimeter energy ratio of charged leptons and other reconstructed particles. Only 'Other' reconstructed particles are not truth-matched to a simulated signal lepton. Semi-leptonic  $t\bar{t}H$  sample is used.

Figure 4.9(left) suggests optimal the selections for isolated lepton is particle's track energy  $E_{track} > 15$  GeV as it cuts away majority of tau decay products and other reconstructed particles.

#### 4.4.3 Isolation Information

Another way to identify isolated leptons from other particles is to consider their isolation in the event. Most particles are reconstructed in the detector region with high occupancy, since most of the particles originate from showers within jets. Electrons and muons from  $W^\pm$  decays are expected to be more isolated whereas tau decay products are not isolated from each other.

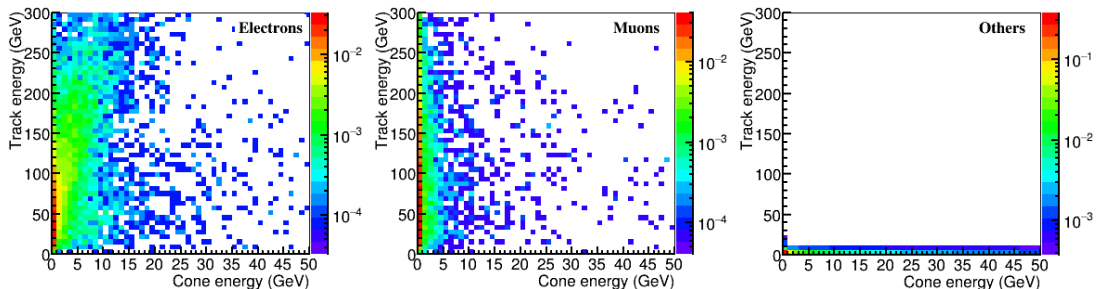


**Figure 4.10** Cone energy with cone size  $\cos \theta = 0.995$  vs track energy for (left) electrons, (middle) muons and (right) other reconstructed particles. Semi-leptonic  $t\bar{t}H$  sample is used.

The energy within a cone size of  $\cos \theta = 0.995$  around the particle's track direction is added to its cone energy,  $E_{cone}$ . The relationship between particle's cone

energy,  $E_{cone}$ , and particle's reconstructed track energy,  $E_{track}$ , is considered. Highly-isolated particles tend to have low cone energy (Figure 4.10(left, middle)) and electrons are observed to radiate more than muons. Both isolated leptons are more energetic and more isolated compare to other reconstructed particles (Figure 4.10(right)). This helps to identify highly energetic leptons which radiates photons at small angles.

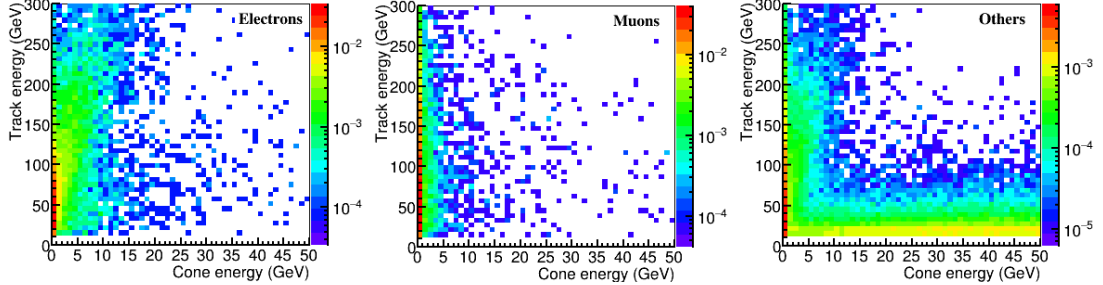


**Figure 4.11** Cone energy with cone size  $\cos \theta=0.995$  vs track energy after cut on impact parameters for (left) electrons, (middle) muons and (right) other reconstructed particles. Semi-leptonic  $t\bar{t}H$  sample is used.

An IP cut ( $|Z_0|$ ,  $|d_0|$  and  $R_0 < 0.05$  mm) is firstly applied (Figure 4.11). It is observed that a lot of the reconstructed particles, other than electrons and muons are still misidentified as leptons (Figure 4.11(right)) with low track energy spreading across a range of cone energy.

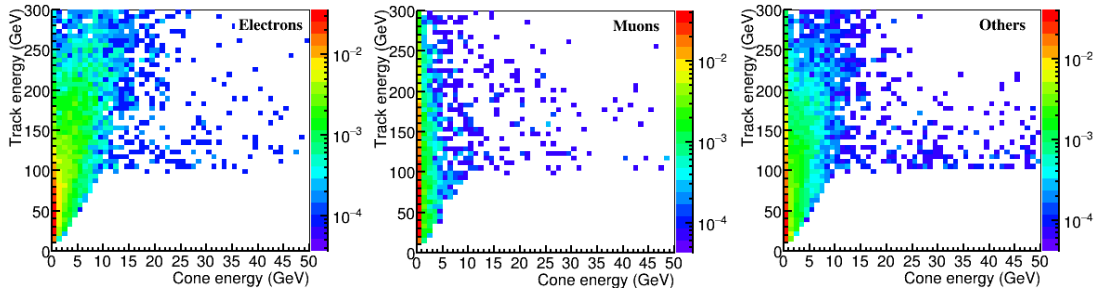


**Figure 4.12** Cone energy with cone size  $\cos \theta=0.995$  vs track energy after impact parameter cuts and polynomial isolation cut for (left) electrons, (middle) muons and (right) other reconstructed particles. Semi-leptonic  $t\bar{t}H$  sample is used.

Therefore, polynomial isolation cut is set to select the isolated leptons: (1) if the cone energy of a particle is larger than 10 GeV, then particle with track energy greater than 100 GeV will be selected; (2) if the particle's cone energy is lower than 10 GeV, then particle with track energy greater than 10 times the cone energy will be selected. The result of the combination of the cuts is shown in Figure 4.12. The combined selection criteria helps to remove majority of the

hadronic particles. The remaining reconstructed particles shown in Figure 4.12(c) has a large fraction of leptons coming from jets as they are not truth-matched to originate from  $W^\pm$  decays.

#### 4.4.4 Summary of Isolated Lepton Selections

For the electrons and muons from  $W^\pm$  decays, the `IsolatedLeptonFinder` `Marlin` processor [72] was used. The criteria to be selected as an electron or muon are summarised below:

- $|Z_0|, |d_0|$  and  $R_0 < 0.05$  mm,
- $E_{track} > 15$  GeV,
- $R_{CAL} > 0.9$  or  $0.05 < R_{CAL} < 0.3$ ,
- particle energy (GeV)  $> \begin{cases} 100 & \text{if cone energy} > 10\text{GeV} \\ 10 \times \text{cone energy} & \text{if cone energy} \leq 10\text{GeV.} \end{cases}$

The  $R_{CAL}$  cut removes particles which do not behave as isolated leptons. The last selection retains highly energetic leptons which radiate a photon whilst removing non-leptons. It is found that 87.3% of truth-matched electrons and muons are selected using a combination of these requirements, only 0.4% of other reconstructed particles that are not truth-matched to a lepton are selected.

#### 4.4.5 Summary of Tau Lepton Selections

The tau leptons are searched using the `Marlin TauFinder` [77] processor which uses `PandoraPF0s`. The following criteria are used when selecting tau leptons, definition of parameters are shown in Figure 4.13, examples of selection criteria are shown in Figure 4.14:

- a seed track of  $p_T > 10$  GeV/c,
- a cone angle,  $\theta_{sig}$ , of 0.04 rad to be added to the seed to form tau candidate,
- all particles to have  $p_T > 2$  GeV/c,
- $R_0$  to be within the range 0.01 mm–0.5 mm,
- the reconstructed tau to have invariant mass less than  $1.5$  GeV/c $^2$ ,
- isolation ring,  $\theta_{iso}$ , to be within  $0.04 - 0.25$  rad around tau seed,
- less than 5 particles within the isolation ring to have a total energy less than 5 GeV.

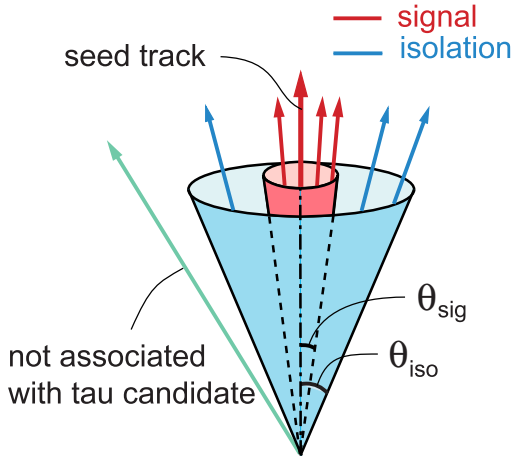


**Figure 4.13** An illustration of a tau lepton cone used to reconstruct a tau candidate. Red cone indicates the signal from a tau lepton, blue cone isolates the tau lepton signal from other particle traces, taken from [76].

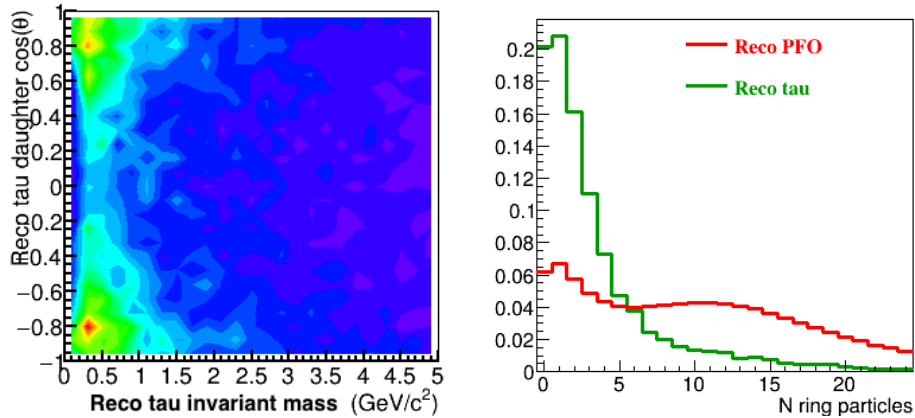


**Figure 4.14** Plots of investigation for tau lepton. (left) Reconstructed tau invariant mass, (right) comparison of number of ring particles of reconstructed tau and particle flow objects. Semi-leptonic  $t\bar{t}H$  sample is used.

#### 4.4.6 Performance of Lepton Selections

The lepton finders process all events to find charged leptons for all signal and background samples with selection criteria described above. A summary of the lepton finding rate is presented in Table 4.3. Approximately 86% of the events in the fully hadronic  $t\bar{t}H$  channel are classified with 0 leptons, and 69% in the semi-leptonic  $t\bar{t}H$  decays are classified with 1 lepton. In the semi-leptonic channel, 29.5% of the event with one lepton is identified as a tau candidate. The selection includes the impact from non-isotropic detector coverage and detection efficiency.

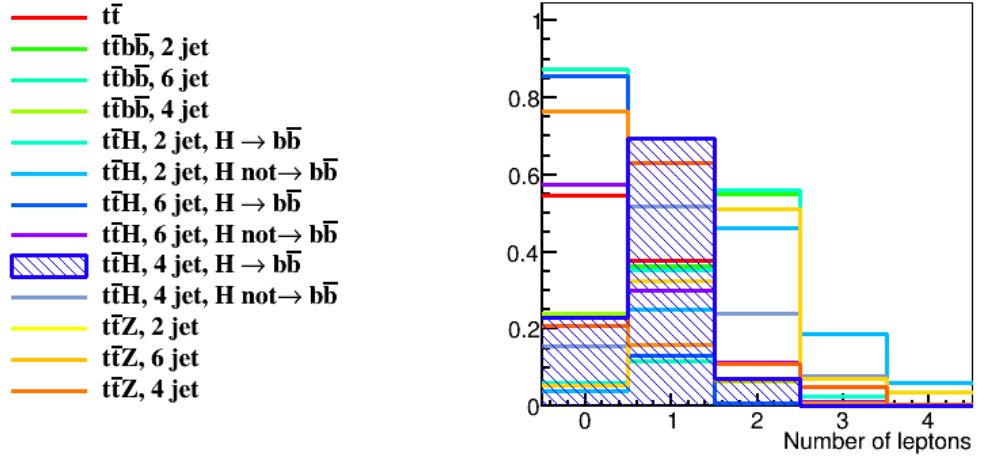


**Figure 4.15** The number of leptons are selected by using a number of criteria listed in Section 4.4.4 and 4.4.5. The shaded region indicates the  $t\bar{t}H$  semi-leptonic signal.

Process	Evt in $1.5 \text{ ab}^{-1}$	Evt with 0 leptons	Evt with 1 lepton
$t\bar{t}H$ , 6 jets, $H \rightarrow bb$	647	553 (85.6%)	86 (13.4%)
$t\bar{t}H$ , 4 jets, $H \rightarrow b\bar{b}$	623	144 (23.1%)	432 (69.4%)
$t\bar{t}H$ , 6 jets, $H \not\rightarrow bb$	473	271 (57.4%)	143 (30.2%)
$t\bar{t}H$ , 4 jets, $H \not\rightarrow b\bar{b}$	455	70 (15.4%)	237 (52.2%)
$t\bar{t}H$ , 2 jets, $H \rightarrow b\bar{b}$	150	9 (6.04%)	53 (35.6%)
$t\bar{t}H$ , 2 jets, $H \not\rightarrow b\bar{b}$	110	4 (4.02%)	27 (25.0%)
$t\bar{t}Z$ , 6 jets	2843	2177 (76.6%)	445 (15.7%)
$t\bar{t}Z$ , 4 jets	2738	567 (20.7%)	1726 (63.0%)
$t\bar{t}Z$ , 2 jets	659	36 (5.53%)	214 (32.5%)
$t\bar{t}bb$ , 6 jets	824	719 (87.3%)	95 (11.6%)
$t\bar{t}bb$ , 4 jets	794	190 (24.0%)	552 (69.5%)
$t\bar{t}bb$ , 2 jets	191	12 (6.07%)	70 (36.7%)
$t\bar{t}$	203700	110430 (54.2%)	76732 (37.7%)

**Table 4.3** Summary of the results from lepton identification. The last two columns show events that are selected with either 0 lepton or 1 lepton. The passing rate is presented as percentage. The number of jets refer to the decay of  $t\bar{t}$  only.

## 4.5 Jet Grouping and Particle Reconstruction

Particles that are not identified as leptons are clustered into eight (hadronic) or six (semi-leptonic) jets plus two beam jets. Beam jets from forward particles induced by the  $e^+e^-$  beams are removed (Figure 4.4). This is done by using the `FastJetProcessor` [78] with the implemented  $k_T$  algorithm [67] using `PandoraPF0s`.

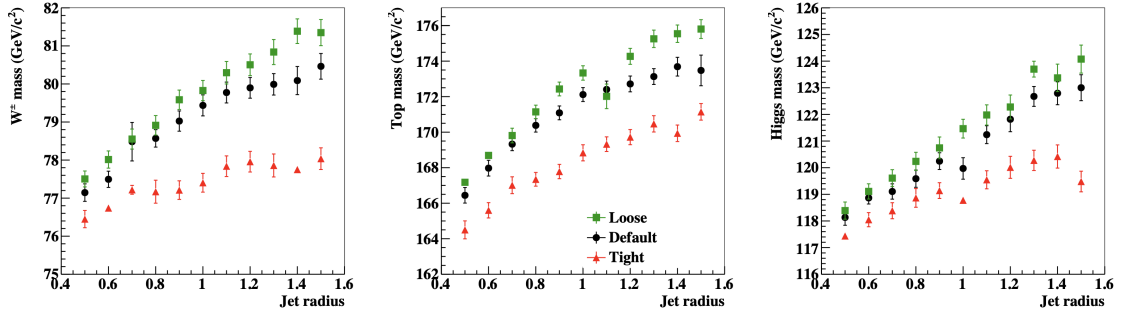


**Figure 4.16** *Fitted invariant mass distributions of truth-matched and reconstructed  $W$  boson, top quark and Higgs boson as a function of jet clustering radius with different levels of background suppression [79].*

In the jet clustering, jets originating from top quarks (3 jets) could be misclustered into 2 jets if the jet clustering radius is too large. This will cause a bump in the top mass region in  $M_{W_{qq}}$ . For this purpose, the optimal jet clustering radius is determined to be 1.0 rad as shown in Figure 4.16.

The clustered jets are then combined using kinematic information to form  $W$ , top and Higgs candidates. A  $\chi^2$  is defined to constraint reconstruction of the  $W^\pm$ ,  $t$  and  $H$  candidates:

$$\begin{aligned} \chi_6^2 &= \frac{(M_{12} - M_{W^\pm})^2}{\sigma_{W^\pm}^2} + \frac{(M_{123} - M_t)^2}{\sigma_t^2} + \frac{(M_{45} - M_H)^2}{\sigma_H^2} \\ \chi_8^2 &= \frac{(M_{12} - M_{W^\pm})^2}{\sigma_{W^\pm}^2} + \frac{(M_{123} - M_t)^2}{\sigma_t^2} + \frac{(M_{45} - M_{W^\pm})^2}{\sigma_{W^\pm}^2} \\ &\quad + \frac{(M_{456} - M_t)^2}{\sigma_t^2} + \frac{(M_{78} - M_H)^2}{\sigma_H^2} \end{aligned} \quad (4.3)$$

where the indices of the mass  $M$  indicate each of the reconstructed jets and  $\sigma$  is the resolution of the reconstructed candidate. Each reconstructed jet  $i$  is combined with another jet  $j$  to form an invariant mass  $M_{ij}$ . The  $W^\pm$ ,  $t$  and

Higgs candidates are selected through iterating all combinations of reconstructed jets to find the smallest value of  $\chi^2$  determined in Equation 4.3.

Since the shapes of the invariant mass distributions are slightly asymmetric as shown in Figure 4.17, the values of  $\sigma$  and mass  $M$  for the reconstructed  $W^\pm$ ,  $t$  and Higgs candidates are determined by fitting with a modified Gaussian:

$$f = \exp \left\{ \left( \frac{-(x - \mu)^2}{g} \right) \right\} \begin{cases} g = 2\sigma_L^2 + \alpha_L(x - \mu)^2, & x < \mu \\ g = 2\sigma_R^2 + \alpha_R(x - \mu)^2, & x > \mu \end{cases} \quad (4.4)$$

with mean  $\mu$ , width  $\sigma_{L,R}$  and tail modification parameter  $\alpha_{L,R}$ . Examples of the fitted distribution is shown in Figure 4.17 for truth-matched reconstructed candidates.

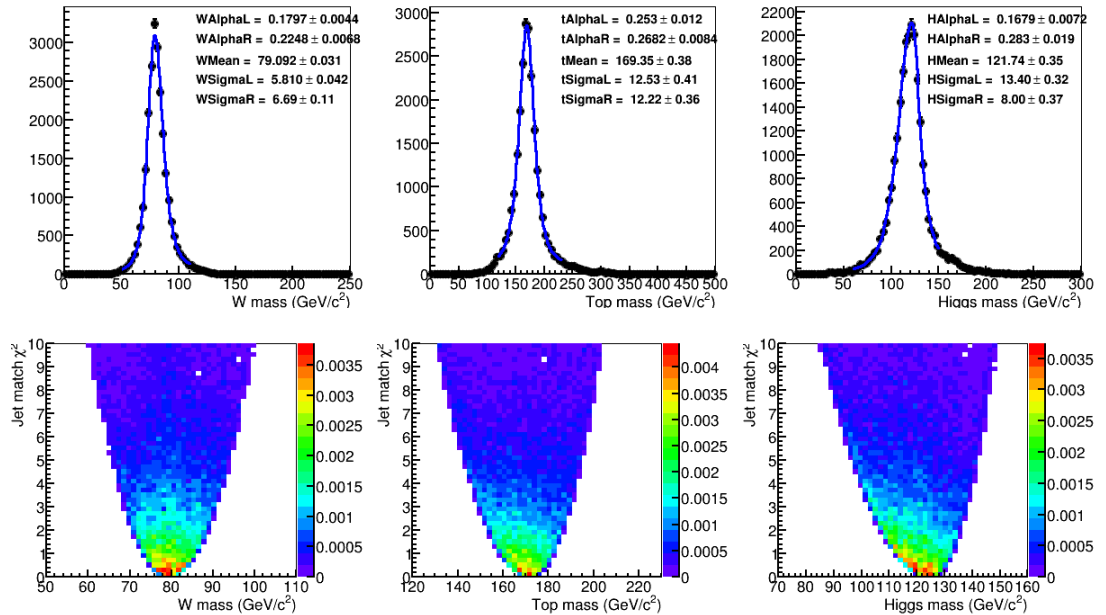


**Figure 4.17** The fitted distribution of the truth-matched reconstructed  $W^\pm$ , top and Higgs candidates using Equation 4.4 from the semi-leptonic  $t\bar{t}H$  sample. The top right corner indicates the values of mean  $\mu$ , width  $\sigma_{L,R}$  and  $\alpha_{L,R}$ . Second row shows  $\chi^2$  values (calculated in equation 4.3) from all possible combinations of jets versus the corresponding reconstructed invariant mass in the semi-leptonic channel for  $W^\pm$ , top and Higgs candidates.

The values obtained from the fitting distributions using Equation 4.4 are insert back into Equation 4.3 to further constrain the selection of particle candidates. The performance of the  $\chi^2$  method (Figure 4.17) shows the majority of the  $W^\pm$ , top and Higgs candidates sit close to the expected value with minimal  $\chi^2$  values.

As shown in Figure 4.17, the masses of reconstructed  $W^\pm$ , top and Higgs candidates are not reconstructed to their true values. This is due to tighter background suppression and energy loss when reconstructing jets. For the latter reason, it can be fixed by adding energy correction to the jets when reconstructing the candidates. However this will not affect the performance of the BDT training and testing as we only care about the shape of the variables, therefore this correction is not implemented in this analysis.

The missing transverse momentum,  $\cancel{p}_T$ , is calculated by summing the momentum of all visible particles in the system:

$$\cancel{p}_x' = - \sum_{i=1}^n p_x^i, \quad \cancel{p}_y' = - \sum_{i=1}^n p_y^i, \quad \cancel{p}_T' = \sqrt{\cancel{p}_x'^2 + \cancel{p}_y'^2}, \quad (4.5)$$

where  $n = 7$  or  $8$  and  $i$  runs over all the jets and the lepton, where present. It accounts for momentum of the neutrinos in the system, particularly useful in separating semi-leptonic  $t\bar{t}H$  channel from other backgrounds.

## 4.6 Flavour Tagging

It is important to identify the  $b$ -jets as many background events do not have four  $b$ -jets in their final states. The dominant background  $t\bar{t}$  events contain at most two  $b$ -jets, as do about 80% of  $t\bar{t}Z$ . This makes flavour tagging a very useful tool in discriminating signal from backgrounds. The flavour tagging is implemented in the `LCFIPplus` package [68] and is tuned by using  $e^+e^- \rightarrow qqqqqq$  samples with the same flavour for all quarks.

Particles are clustered using the Durham algorithm [80]. Flavour tagging are performed for each jet using `LCFIPplus`.  $b$ -tag and  $c$ -tag values are calculated using MVA selections implemented in the `LCFIPplus` package. Large values of  $b$ -tag ( $c$ -tag), close to 1, indicate the jet is likely to be a  $b$ -jet ( $c$ -jet). Figure 4.18 illustrates the value of the  $b$ -tag calculated by `LCFIPplus` for the jet with the 3rd highest value of  $b$ -tag, and the  $c$ -tag value of the jet with the highest value of  $b$ -tag. The major background,  $t\bar{t}$ , has 2  $b$ -jets in the final states whilst our signal,  $t\bar{t}H$ , has 4  $b$ -jets in its final states. Therefore, the 3rd highest value of  $b$ -tag will be the most effective discriminating variable to separate our signal from this huge background.

The distance between the two closest jets,  $y_{ij}$ , is used in distinguishing signal from lower jet multiplicity backgrounds such as  $t\bar{t}$  events. The distance  $y_{ij}$  between jet  $i$  and jet  $j$  ( $j = i + 1$ ) is defined as:

$$y_{ij} = \frac{\min(E_i^2, E_j^2)(1 - \cos \theta_{i,j})}{s}, \quad (4.6)$$

with centre of mass energy  $\sqrt{s}$ , angle  $\theta$  between the two jets and jet energy  $E_{i,j}$  that choose to minimise the distance between the two jets which are merged. Due to many jets in both of semi-leptonic and fully-hadronic signal channels ( $>4$  jets), signals can be separated from low jet multiplicity backgrounds by looking at  $y_{45}$ ,  $y_{56}$  and  $y_{67}$ .

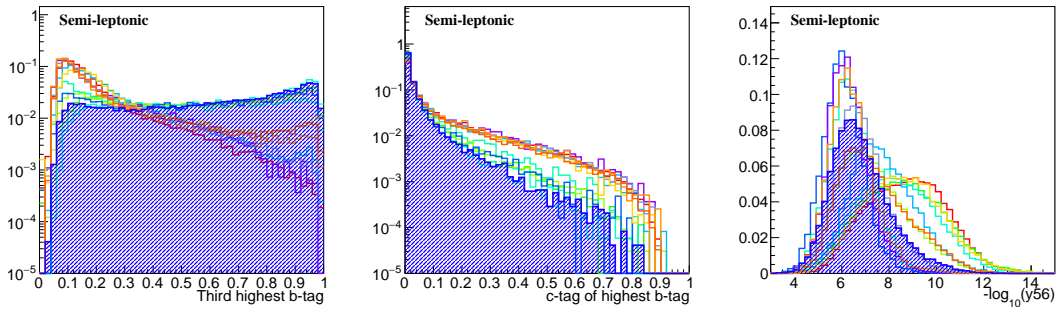


**Figure 4.18** Jet information used to train the BDTs (left) third highest b-tag probability, (middle)  $c\text{-tag}/(c\text{-tag}+b\text{-tag})$  for the third highest b-tag and  $c\text{-tag}$  values and (right) distance between two merged jets  $y_{56}$ . Colour labels follows Figure 4.15 where shaded area indicates the semi-leptonic signal.

## 4.7 Signal Selection using Multivariate Analysis

Signal events are selected using a Boosted Decision Tree Gradient (BDTG) classifier implemented in TMVA [69]. The samples for signal and background are separated randomly into two sets. The first half of the sample is used to train and test the BDTG and the second half of the sample is used as “real” data samples where the weight from BDTG is applied. This prevents any bias in the MVA selection. In the first half of the sample, a pre-selection is applied to constrain to exactly 0 or 1 isolated leptons and to either 6 or 8 jets. The following variables are used as input to train and test the BDTG.

- number of reconstructed particles in the event;

- visible energy contained within jets;
- missing transverse momentum  $\cancel{p}_T$ ;
- reconstructed Higgs mass,  $m_H$ ;
- $\chi^2$  of combined jets as defined in Equation 4.3;
- four highest  $b$ -tag and  $c$ -tag values;
- distance between two closest jets  $y_{ij}$  as described in Equation 4.6, specifically  $y_{45}, y_{56}, y_{67}$ ;
- cosine of the angle of between the two  $b$  quarks from  $H \rightarrow b\bar{b}$  decay;
- cosine of the angles between the Higgs and each of the top quark.

Additionally for the semi-leptonic channel, we make use of the lepton information:

- cone energy of the isolated lepton with cone size  $\cos\theta = 0.995$ ;
- ratio of the calorimeter energy  $R_{CAL}$  as defined in Equation 4.2.

For the fully-hadronic channel, we make use of the jet information:

- energy of the four lowest-energy jets;
- cosine of the angle between the two jets that are closest to the beam axis.

All the samples are weighted assuming an integrated luminosity of  $1.5 \text{ ab}^{-1}$ . Using the first half of the samples, the BDTG response of the testing and training samples are found (see Figure 4.19(left)). No sign of overtraining is observed. The weight from BDTG training is then applied to the other half of the samples which act as “real data”. The BDTG response for each of the signal and background events is then calculated as shown in Figure 4.19(right).

The optimal selection on the signal events is calculated by finding the maximum significance. Significance defined as  $S/\sqrt{S+B}$  where  $S$  is the yield of selected signal events and  $B$  is the yield of selected background events after the MVA cut. All the  $t\bar{t}H$  events are considered as signal in the significance calculation. By looping over a range of MVA cut values, the best cut which yield the maximal significance is found to be  $> 0.069$  for the semi-leptonic channel (Figure 4.20) and  $> 0.181$  for hadronic channel. This gives a significance of 9.00 for semi-leptonic channel and 10.44 for hadronic channel.

The summary of results from both pre-selection and MVA selection are shown in Table 4.4. Most backgrounds are reduced to less than 10%, while a high proportion of signal events remain 56.8% (Had) and 43.4% (SL). The largest background,  $t\bar{t}$ , has the least signal-like events and has been cut by 99.6% (SL) and

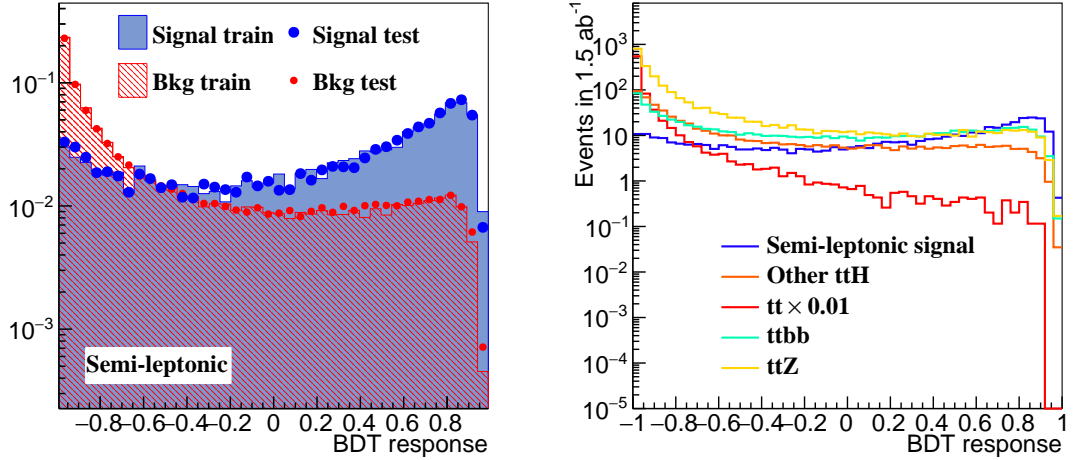


**Figure 4.19** The BDTG response for signal and background samples. (left) Normalised BDTG response to check the overtraining (right) Scaled BDTG to number of events expected in  $1.5 \text{ ab}^{-1}$  with second half of the samples by applying weight from (left).

99.8% (Had). The irreducible background from  $t\bar{t}b\bar{b}$  still remains with relatively high percentage due to the  $b$ -tagging. A dedicated study into how to separate the  $t\bar{t}b\bar{b}$  from  $t\bar{t}H$  signals could improve the result.

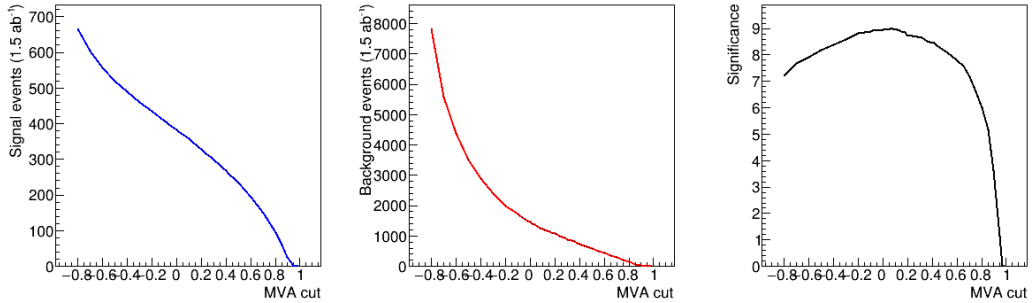


**Figure 4.20** The optimal significance is calculated with the best MVA cut value (right),  $S/\sqrt{S+B}$ , by looping over a range of MVA values for signal and background samples.

Process	Evt in 1.5 ab <sup>-1</sup>	Evt with 0 Lepton	Evt with 1 Lepton	Pre-selection + Had BDT	Pre-selection + SL BDT	Evt pass Evt pass
$t\bar{t}H$ , 6 jets, $H \rightarrow b\bar{b}$	647	555 (85.9%)	86 (13.4%)	367 (56.8%)	38 (5.91%)	
$t\bar{t}H$ , 4 jets, $H \rightarrow b\bar{b}$	623	208 (33.4%)	432 (69.4%)	1 (0.14%)	270 (43.4%)	
$t\bar{t}H$ , 6 jets, $H \not\rightarrow b\bar{b}$	473	276 (58.4%)	143 (30.2%)	54 (11.4%)	11 (2.32%)	
$t\bar{t}H$ , 4 jets, $H \not\rightarrow b\bar{b}$	455	70 (15.4%)	237 (52.2%)	8 (1.85%)	22 (4.88%)	
$t\bar{t}H$ , 2 jets, $H \rightarrow b\bar{b}$	150	9 (6.18%)	53 (35.6%)	2 (1.65%)	22 (14.8%)	
$t\bar{t}H$ , 2 jets, $H \not\rightarrow b\bar{b}$	110	4 (3.90%)	27 (25.0%)	0 (0.11%)	1 (1.19%)	
$t\bar{t}Z$ , 6 jets	2843	2133 (75.0%)	445 (15.7%)	345 (12.1%)	34 (1.21%)	
$t\bar{t}Z$ , 4 jets	2738	571 (20.9%)	1726 (63.0%)	59 (2.14%)	217 (7.94%)	
$t\bar{t}Z$ , 2 jets	659	36 (5.49%)	214 (32.5%)	1 (0.22%)	16 (2.45%)	
$t\bar{t}b\bar{b}$ , 6 jets	824	720 (87.5%)	95 (11.6%)	326 (39.5%)	26 (3.14%)	
$t\bar{t}b\bar{b}$ , 4 jets	794	193 (24.3%)	552 (69.5%)	57 (7.15%)	226 (28.54%)	
$t\bar{t}b\bar{b}$ , 2 jets	191	11 (5.84%)	70 (36.7%)	2 (0.82%)	18 (9.70%)	
$t\bar{t}$	203700	116181 (57.0%)	76732 (37.7%)	498 (0.24%)	742 (0.36%)	
total $t\bar{t}H$ signal	2458	1123 (45.7%)	978 (39.8%)	433 (17.6%)	365 (14.8%)	
total background	211749	119846 (56.6%)	79834 (36.3%)	1287 (0.61%)	1280 (0.60%)	

**Table 4.4** Selection efficiency for each of the signal and background samples in both channels. Column 3 shows the number of events after the pre-selection (Section 4.4.6) with passing rate indicated in percentage. Column 4 shows the number of events that passes the pre-selection and the MVA selection, the passing rate is a combined result with pre-selection. Total number of signal and background after cuts are summarised at the bottom. Number of jets is refer to  $t\bar{t}$  decays.

## 4.8 Results on Precision of Top-Yukawa Coupling

The uncertainty on the cross-section is calculated from the inverse of the signal significance. This gives a combined (leptonic+hadronic) precision of 7.3% for measuring the cross-section by assuming an integrated luminosity of  $1.5 \text{ ab}^{-1}$ .

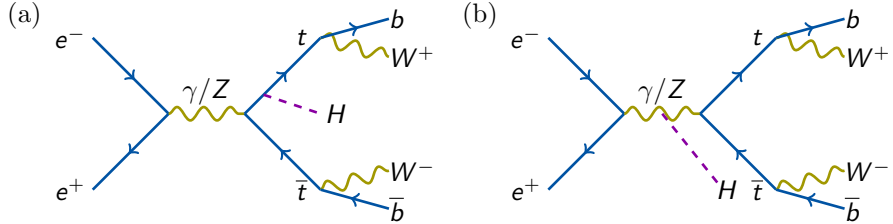


**Figure 4.21** Feynman diagrams for the  $e^+e^- \rightarrow t\bar{t}H$  process with (a) a Higgs boson radiates from the top quark and (b) a Higgs boson radiates from the Z boson which is also called the Higgs-strahlung process  $e^+e^- \rightarrow Z^*H$  with  $Z^* \rightarrow t\bar{t}$ .

The precision on the top-Yukawa coupling ( $g_{t\bar{t}H}$ ) is calculated from the uncertainty measurement on the  $t\bar{t}H$  cross-section ( $\sigma$ ). However, the Higgs-strahlung process  $e^+e^- \rightarrow ZZH$  with  $Z \rightarrow t\bar{t}$  as shown in Figure 4.21(b) needs to be taken into account. It contributes a small, but non-negligible, contribution to the total cross section, but is independent of  $g_{t\bar{t}H}$ . We can evaluate this by plotting the predicted cross-section against the corresponding top-Yukawa coupling. A linear approximation

$$\Delta g_{t\bar{t}H}/g_{t\bar{t}H} = \kappa \cdot \Delta\sigma/\sigma, \quad (4.7)$$

and  $\kappa = 0.53$  is found with the presence of the diagram at  $\sqrt{s} = 1.4 \text{ TeV}$  at LO (see Figure 4.22). This is due to the interference between the two Feynman diagrams in Figure 4.21. If the interference didn't exist,  $\kappa = 0.5$  [81]. This suggests a non-negligible contribution from the Higgs-strahlung diagram to the total cross-section at high centre of mass energies.

### 4.8.1 LO to NLO Correction

The latest NLO prediction for the parameter  $\kappa$  has been produced to translate the uncertainty on the  $t\bar{t}H$  cross-section to an uncertainty of the top-Yukawa coupling [81]. A modified version of WHIZARD 2.6.2 was used at NLO QCD which gives  $\kappa = 0.4886 \pm 0.0013$  with linear fit (as done in [81]) and  $\kappa = 0.5032 \pm 0.0005$  with quadratic fit (as done in Figure 4.22).

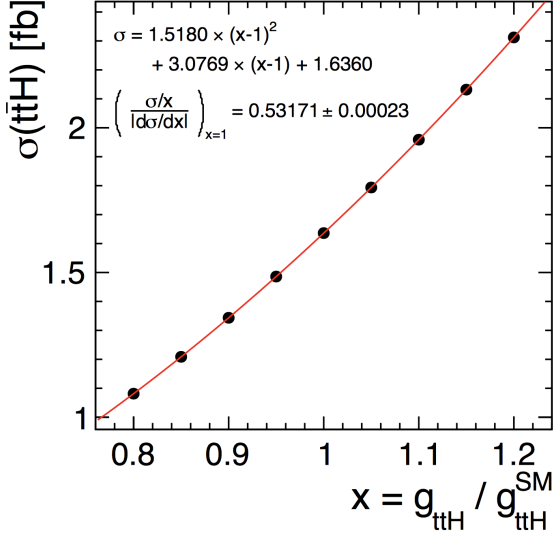


**Figure 4.22** The cross-section of the  $e^+e^- \rightarrow t\bar{t}H$  process as a function of the top-Yukawa coupling values  $g_{t\bar{t}H}$  at  $\sqrt{s} = 1.4$  TeV, including the Higgs-strahlung effect [79].

As all of the simulation studies are done under LO where  $\sigma_{LO}^{QCD} = 1.5589 \pm 0.0014$  fb. The cross sections are scaled to NLO with  $\sigma_{NLO}^{QCD} = 1.4625 \pm 0.0015$  fb. This leads to a NLO cross-section measurement of 7.5%. The precision on the top-Yukawa coupling can then be extracted by using the factor  $\kappa = 0.5032 \pm 0.0005$ :

$$\frac{\Delta g_{t\bar{t}H}}{g_{t\bar{t}H}} = 0.503 \frac{\Delta \sigma(t\bar{t}H)}{\sigma(t\bar{t}H)}. \quad (4.8)$$

This gives an uncertainty of 3.8% on the top-Yukawa coupling measurement in NLO by combining results from both fully-hadronic and semi-leptonic  $t\bar{t}H$  channels at  $\sqrt{s} = 1.4$  TeV without polarisation.

#### 4.8.2 CLIC Luminosity Scheme with Polarised Beam

An updated CLIC luminosity scheme proposes an integrated luminosity of  $2.5 \text{ ab}^{-1}$  using a polarised electron beam. An integrated luminosity of  $2.0 \text{ ab}^{-1}$  is taken with  $P(e^-) = -80\%$  and  $0.5 \text{ ab}^{-1}$  with  $P(e^-) = +80\%$ . With this new scheme, the uncertainty on the cross-section is improved to 5.4% and the uncertainty on the top-Yukawa coupling is improved to 2.7% due to the increased cross-section in  $t\bar{t}H$  signal. The new results are obtained from recalculating the significance ( $S/\sqrt{S+B}$ ) by scaling the signal and the backgrounds. These results

are comparable with a similar study carried out by ILC that obtains statistical precision of 4.5% on the top-Yukawa coupling at  $\sqrt{s} = 1$  TeV using unpolarised beam [82].

The statistical uncertainty of the measurement of the cross-section (5.4%) is expected to dominate over the systematic uncertainty due to the relatively clean environment. Sources of systematic uncertainty such as jet energy scale, lepton reconstruction and flavour-tagging are expected to be very small (well below 10%) compare to the cross-section measurement. A previous study of systematic uncertainty of the luminosity spectrum reconstruction was found to be small at  $\sqrt{s} = 1.4$  TeV [83].

## 4.9 Higgs Boson CP Analysis

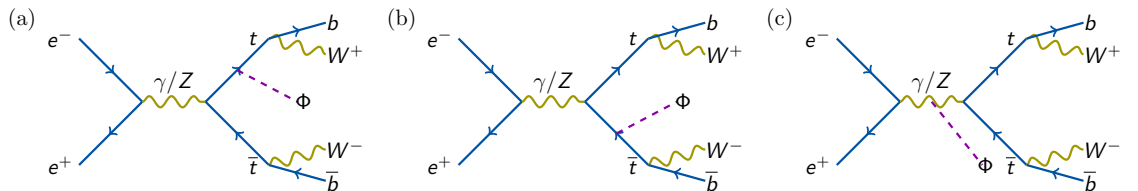


**Figure 4.23** Feynman diagrams for the  $e^+e^- \rightarrow t\bar{t}\Phi$  process with (a) a CP-violating Higgs boson  $\Phi$  radiates from the top quark, (b)  $\Phi$  radiates from  $\bar{t}$  and (c)  $\Phi$  radiates from the  $Z$  boson which will cause interference with (a) and (b).

An extension of the  $t\bar{t}H$  study looking at the CP properties of the Higgs boson is presented in this section. As introduced in Section 2.6.1, the Higgs boson is a mixed state of scalar and pseudoscalar components, which is written as  $\Phi$ . The  $t\bar{t}\Phi$  coupling can be then described as

$$C_{\Phi t\bar{t}} = -ig_{Ht\bar{t}}(a + ib\gamma_5). \quad (4.9)$$

Setting  $a = \cos \phi$  and  $b = \sin \phi$ , this reduces the free parameter to a mixing angle  $\phi$ . A measurement of  $\phi$  will give direct indication of CP-violation in the Higgs boson.

### 4.9.1 Event Generation

Samples are generated using Physsim [71] with different values of  $\sin^2 \phi$  for both hadronic and semi-leptonic channels. This is to be consistent with the top-Yukawa coupling measurement presented in Section 4.8 where the result will be used in the CP study. The centre-of-mass energy is 1.4 TeV with unpolarised beams. ISR and beamstrahlung effects are included. The CLIC luminosity spectrum [63] is employed and 12 samples are produced in total. The  $ZZ\Phi$  is included in the cross-section calculation with  $c = 1$  in Equation 2.24.

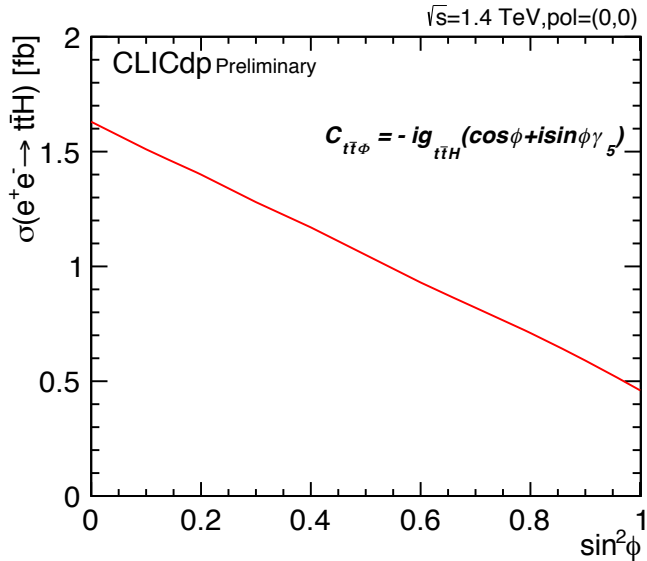


**Figure 4.24** The cross-section calculation for simulated  $e^+e^- \rightarrow t\bar{t}\Phi$  samples with mixing angle,  $\phi$ ,  $0 \leq \sin^2 \phi \leq 1$  with unpolarised beam at  $\sqrt{s} = 1.4$  TeV, including contribution from  $ZZ\Phi$ .

### 4.9.2 Cross-Section Measurement

The coupling strength becomes weaker as the proportion of pseudoscalar Higgs increases, since the coupling between  $ZZ$  and CP-odd Higgs is zero at tree level. This leads to a reduction in the total cross section. The signal and backgrounds samples used in this analysis are the same as shown in Table 4.2. To translate the expected number of events to the corresponding  $\sin^2 \phi$  value, a scale factor  $\sigma_{CP}/\sigma_{SM}$  (values can be found in [84]) is applied to all possible  $t\bar{t}\Phi$  decay samples and the branching ratio of  $H \rightarrow b\bar{b}$  is assumed to be unchanged. The expected cross-section measurements from simulation for all  $\sin^2 \phi$  values are presented in Figure 4.24.

### 4.9.3 Results on Sensitivity to CP-Mixing in Higgs Boson

The precisions on the cross-section are obtained separately for hadronic and semi-leptonic samples with the same  $\sin^2 \phi$  value. The cross-section measurements are performed with same procedure as described in Section 4.7 to all semi-leptonic samples with different CP values whereas for hadronic channel the results are extrapolated by only applying the  $\sigma_{CP}/\sigma_{SM}$  scale factor. The results from both channels are combined to give a better precision measurement.

The cross-section measurements become less precise as  $\sin^2 \phi$  increases, with an uncertainty of  $\sim 24\%$  for a pure pseudoscalar Higgs boson. This is due to decreasing total cross-section of the  $t\bar{t}\Phi$  at higher  $\sin^2 \phi$  values. If assuming any reduction in the observed cross-section is due to CP mixing, then this effect can be used to discriminate the pseudoscalar Higgs boson from the scalar Higgs boson. With the CLIC machine, measurements can be performed to a very high precision. By using the cross-section measurement used in top-Yukawa coupling analysis, the precision on the cross-section for different  $\sin^2 \phi$  values can be determined.

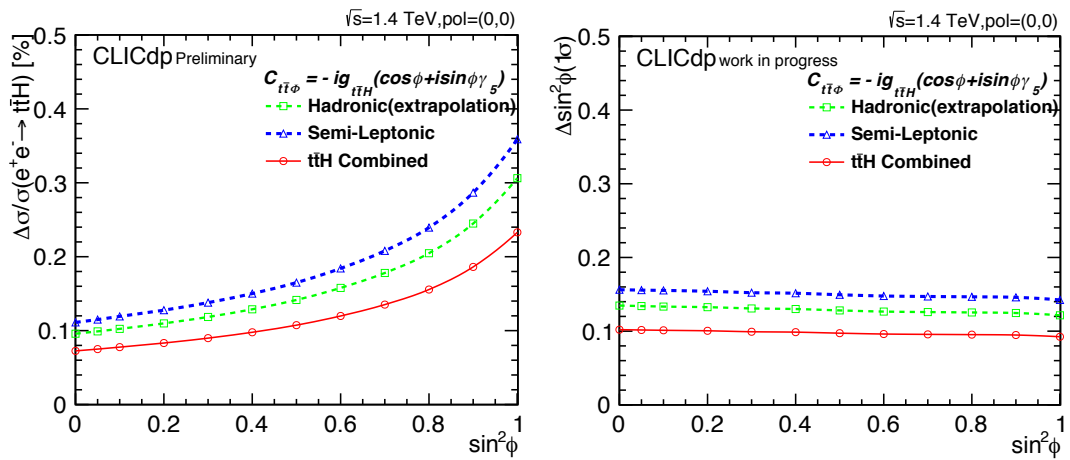


**Figure 4.25** (Left) Measurements on the precision of cross-section for mixing angle,  $\phi$ ,  $0 \leq \sin^2 \phi \leq 1$  with unpolarised beam at  $\sqrt{s} = 1.4$  TeV with luminosity of  $1.5 \text{ ab}^{-1}$ . (Right) The calculated uncertainty on  $\sin^2 \phi$  for CP-violating Higgs boson  $\Phi$  using Equation 4.10. Results obtained for semi-leptonic channel is from cross-section measurement, results for hadronic channel are from extrapolation. Data points are connected with lines of best fit.

Firstly, measurements of cross-section of mixing angle  $0 \leq \sin^2 \phi \leq 1$  are produced (Figure 4.24). Then a linear fit,  $\sigma = k \sin^2 \phi + c$ , is applied to relate the cross-section with  $\sin^2 \phi$ . This then allows us to deduce the uncertainty on  $\sin^2 \phi$  by error propagation:

$$\Delta(\sin^2 \phi) = \frac{1}{k} \frac{\Delta\sigma_\phi}{\sigma_\phi} \sigma_\phi, \quad (4.10)$$

where  $k$  is the gradient of the slope in Figure 4.24,  $\sigma_\phi$  is the cross-section at specific  $\phi$  value and  $\Delta\sigma_\phi/\sigma_\phi$  becomes the precision on cross-section measurements at specific  $\phi$  value. This can be directly obtained from data points in Figure 4.25.

The result from Figure 4.25 shows the uncertainty of  $\Delta \sin^2 \phi$  or  $\Delta \cos^2 \phi$  (from  $\cos^2 \phi + \sin^2 \phi = 1$ ) can be constrained to around 0.1 with unpolarised beam and an integrated luminosity of  $1.5 \text{ ab}^{-1}$  at  $\sqrt{s} = 1.4 \text{ TeV}$ . In other words, the contribution from pure CP-odd Higgs can be measured to  $\sim 10\%$  accuracy at  $1\sigma$ .

#### 4.9.4 Angular Observable: Up-Down Asymmetry

The up-down asymmetry is defined by the angle between the  $\bar{t}$  direction and the top-electron plane where the electron is the electron beam. This observable is sensitive to CP violation as it accounts for the interference between the on-shell process and the off-shell process as in Figure 4.23 according to [39]. The up-down angle  $\zeta$  between the  $\bar{t}$  and the top-electron plane is given by

$$\sin \zeta = \frac{\vec{p}_{\bar{t}}(\vec{q}_{e^-} \times \vec{p}_t)}{|\vec{p}_{\bar{t}}||\vec{q}_{e^-} \times \vec{p}_t|}, \quad (4.11)$$

and the up-down asymmetry is defined as

$$A_\zeta = \frac{N(\sin \zeta > 0) - N(\sin \zeta < 0)}{N(\sin \zeta > 0) + N(\sin \zeta < 0)}, \quad (4.12)$$

where  $N(\sin \zeta > 0)$  denotes the number of events that  $\bar{t}$  is above the plane and  $N(\sin \zeta < 0)$  denotes the number of events that  $\bar{t}$  is below the plane.

The semi-leptonic channel where the charge of the lepton in the final state can be used to identify the  $t$  and  $\bar{t}$  candidates is used. Then the  $t$  and  $\bar{t}$  can be identified as follows: if the lepton charge is negative, the reconstructed leptonic candidate ( $bl\nu$ ) is assigned to be a  $t$  and the hadronic candidate ( $bq\bar{q}$ ) is assigned as an  $\bar{t}$ , vice versa. The 4-momentum of the reconstructed  $t$  and  $\bar{t}$  are obtained in their rest frame and are boosted to the  $t\bar{t}\Phi$  rest frame to calculate  $\sin \zeta$ .

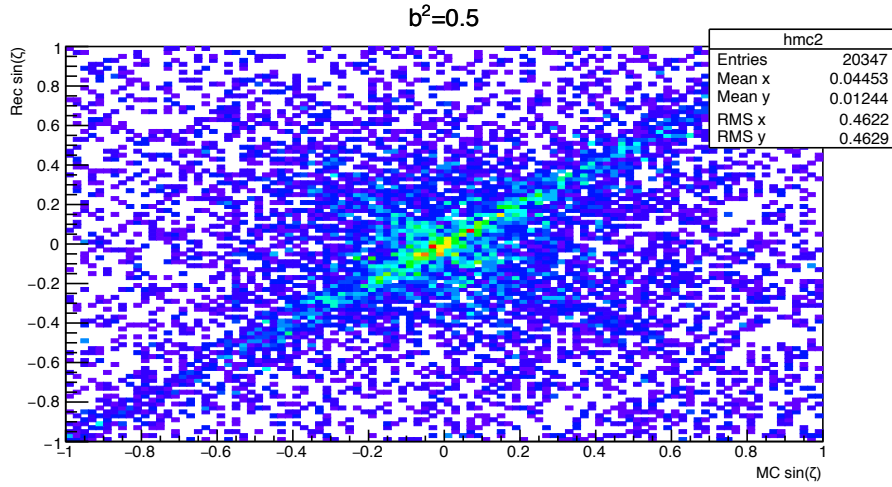


**Figure 4.26** Correlation of up-down  $\sin \zeta$  in Equation 4.11 between reconstruction and MC at  $\sin^2 \phi = 0.5$  before cuts using semi-leptonic  $t\bar{t}H$  sample.

To match the reconstruction events to the MC events, cuts are investigated by looking at events passing or failing the requirement  $|\sin \zeta_{rec} - \sin \zeta_{mc}| < 0.05$ , MVA cuts obtained from cross-section measurements for different CP values are applied to the corresponding CP samples by default. As shown in Figure 4.26, a clear diagonal line is expected from  $(-1, -1)$  to  $(1, 1)$ . The off-diagonal line is due to the mis-identification of the charge of the top quark, the backgrounds are due to the mis-reconstruction of the top quark. Final state leptons include hadronic tau leptons for which the charge are hard to reconstruct, this causes mis-identification of the top quark. Therefore, events with tau lepton in the final states are removed. The jet matching  $\chi^2_6$  defined in Equation 4.3 is constrained below 10 to reduce the mis-reconstructed top quarks. Another cut that can be applied to improve the matching is to constraint the mass of leptonic top quark  $m_{t_{lep}}$ . This is because the reconstruction of a leptonic top is by combining jet information together with an isolated lepton and a neutrino. If jets and neutrino are mis-reconstructed and mis-assigned to a leptonic quark, the value of  $\sin \zeta_{rec}$  in Equation 4.11 will be mis-calculated. However, due to the high tail of the leptonic top mass distribution Figure 4.27 (right), this will cut away a lot of signals and thus reduce the precision.

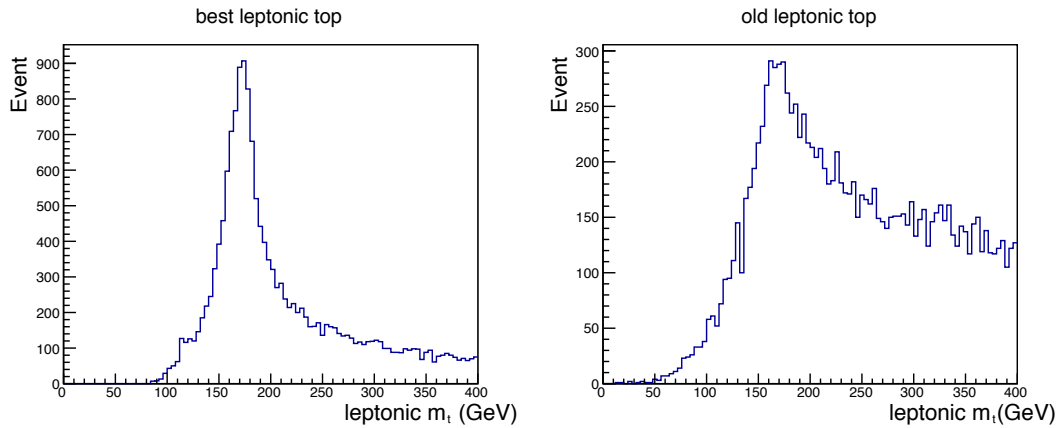


**Figure 4.27** Reconstructed leptonic top mass distribution with (left) new neutrino reconstruction method with jet matching  $\chi^2_6 < 10$  and  $m_{t_{lep}} < 220$  GeV, and (right) old method. Semi-leptonic  $t\bar{t}H$  sample is used.

#### 4.9.5 Neutrino Reconstruction

The cause of the high tail in the leptonic top mass distribution is found to be the reconstructed neutrino. The traditional method of reconstructing the neutrino is to assign all the missing momentum to the neutrino. This method includes the ISR effect and thus cause a high tail in the reconstructing leptonic top mass as illustrated in Figure 4.27 (right). A new method is implemented to constraint the neutrino  $p_T$  such that the neutrino-lepton invariant mass is above the  $W$  boson mass. Then a solution that is closest to the top mass is selected after combining with other jets. With the new reconstruction method, the cuts are investigated again. As shown in Figure 4.27 (left), the high tail of leptonic top mass issue has been resolved. MVA cuts are applied and tau leptons are removed. The best cuts are found to be (1) jet matching  $\chi^2_6 < 10$  and (2)  $m_{t_{lep}} < 220$  GeV.

The newly investigated cuts are applied to select the signals. As shown in Figure 4.28, the reconstructed up-down angle distribution matches the MC distribution. The correlation of  $\sin\zeta$  between reconstruction and MC (Figure 4.29) shows a much clearer diagonal line, indicating a higher level of matching. Finally, the up-down asymmetry with different CP values shows a better agreement between the reconstruction and MC after investigation into neutrino reconstruction as shown in Figure 4.30.

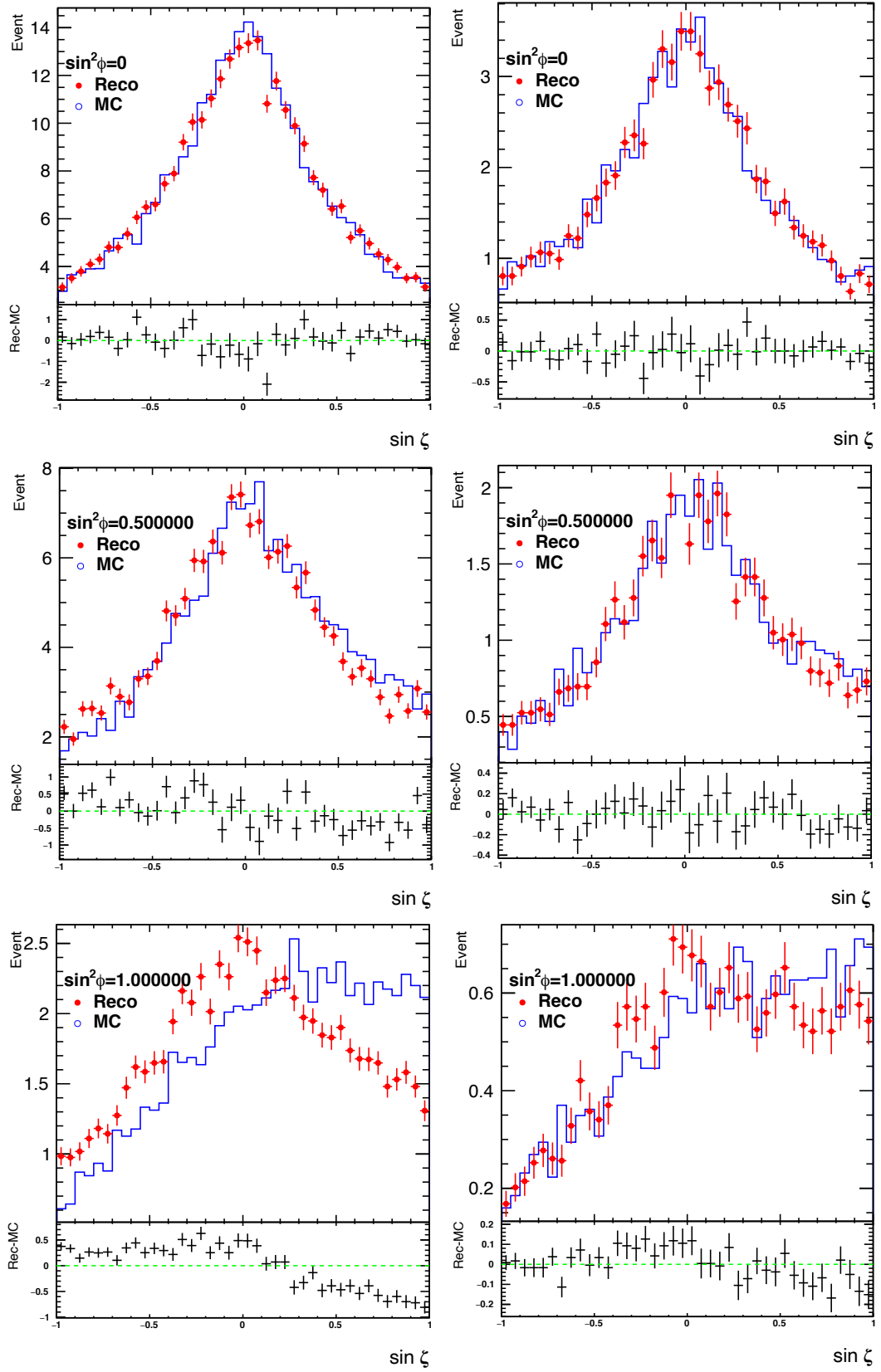


**Figure 4.28** Up-down angle distribution of  $\sin \zeta = 0$  (top),  $\sin \zeta = 0.5$  (middle) and  $\sin \zeta = 1$  (bottom) with no cuts (left) and tight cuts (right) (1) remove taus, (2) jet matching  $\chi^2_6 < 10$ , (3)  $m_{t_{lep}} < 220$  GeV.

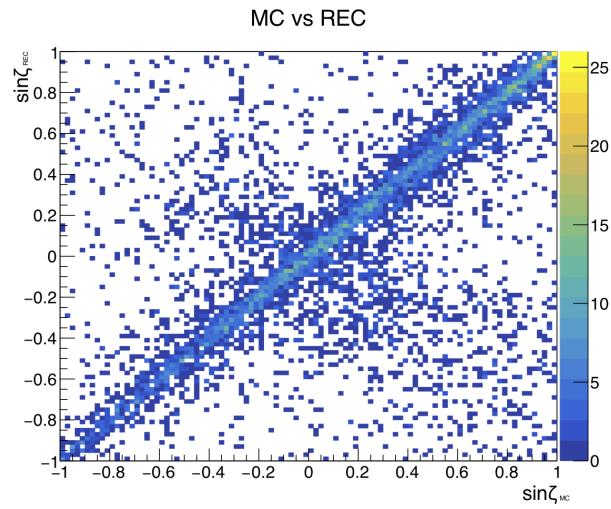


**Figure 4.29** Correlation of  $\sin \zeta$  between reconstruction and MC at  $\sin^2 \phi = 0.5$  with cuts (1) remove taus, (2) jet matching  $\chi^2_6 < 10$ , (3)  $m_{t_{lep}} < 220$  GeV with semi-leptonic  $t\bar{t}H$  sample.

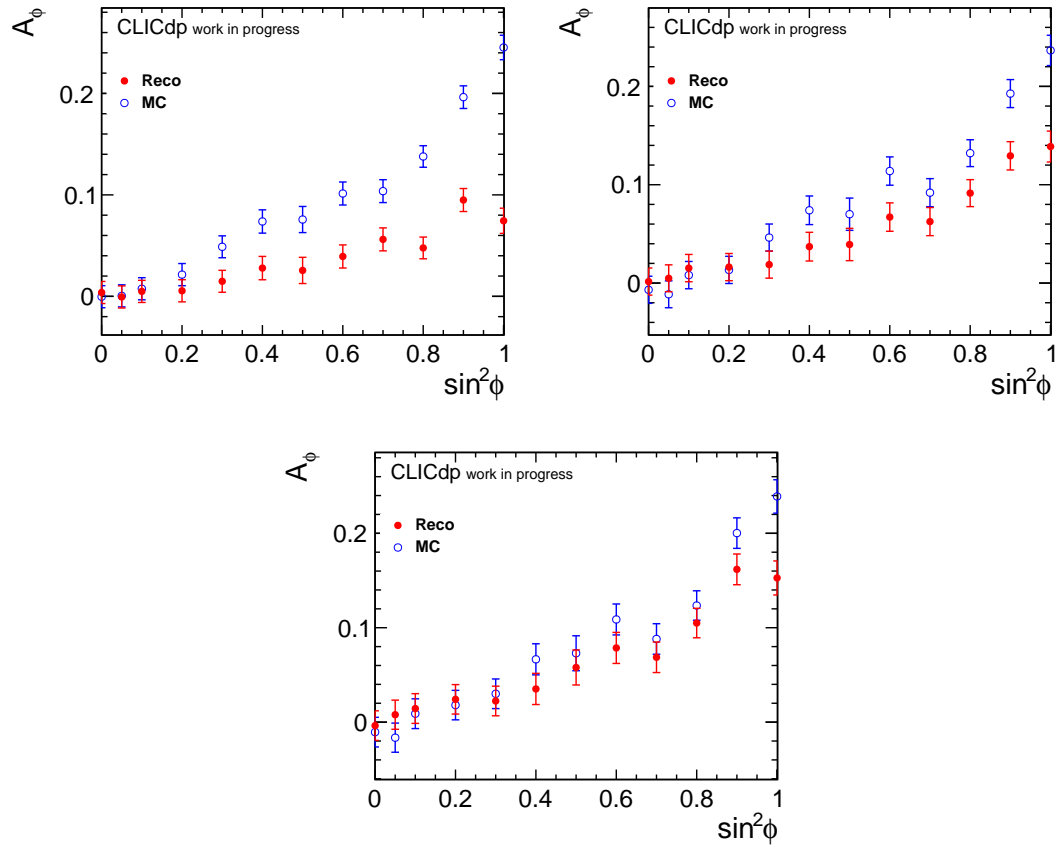


**Figure 4.30** Up-down asymmetry with (top left) no cuts, (top right)  $m_{t_{lep}} < 220$  GeV, (bottom)  $m_{t_{lep}} < 220$  GeV and jet matching  $\chi^2_6 < 10$ . Then up-down asymmetry is calculated using Equation 4.12.

## 4.9.6 $\chi^2$ Template Fit

To extract the uncertainty measurement of  $\sin^2 \phi$  from up-down asymmetry, a  $\chi^2$  template fit is used:

$$\chi_n^2(\sin^2 \phi = 0.5) = \sum_{i=1}^{nbins} \left( \frac{O_{data(\sin^2 \phi=0.5)} - O_{MC(n)}}{\sigma(data)} \right)^2, \quad (4.13)$$

where  $n$  is the different  $\sin^2 \phi$  samples ( $\sin^2 \phi = 0.5$  is an example that we are calculating  $\chi^2$  value for  $\sin^2 \phi = 0.5$ ),  $O_{data}$  is the number of reconstructed events in the bin,  $O_{MC}$  is the number of MC events in the same bin of different  $\sin^2 \phi$  samples and  $\sigma_{data}$  is the error of  $O_{data}$ . For example, if  $\chi^2$  is calculated with reconstructed data points at  $\sin^2 \phi = 0.5$  and MC data points at  $\sin^2 \phi = 0.2$ , this will give the forth  $\chi^2$  value in Figure 4.31(right).

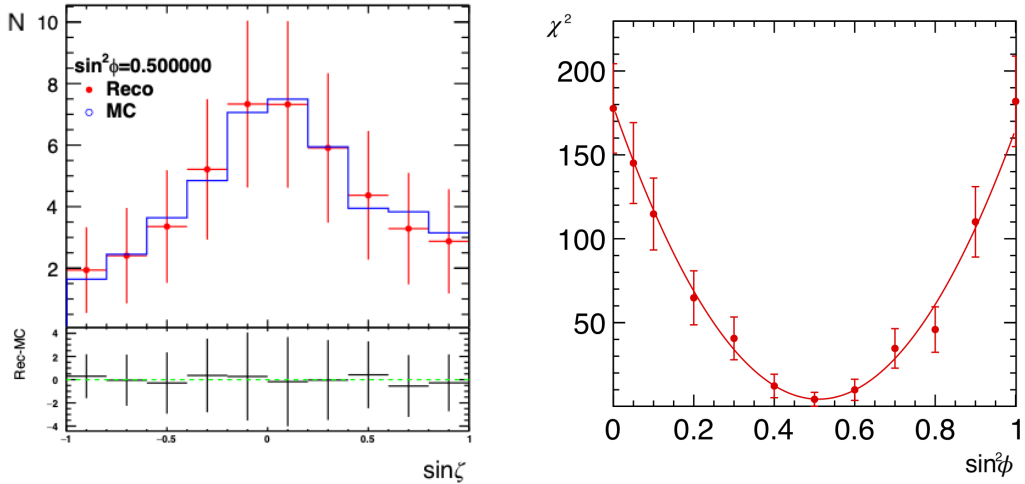


**Figure 4.31** Results of template fit as discussed in Section 4.9.6. (left) weighted  $\sin \zeta$  distribution with mixing angle  $\sin^2 \phi = 0.5$ , (right) calculated  $\chi^2$  at  $\sin^2 \phi = 0.5$  with best polynomial fit.

The measurement of  $\sin^2 \phi$  is obtained by using a polynomial fit to find the minimum point of the  $\chi^2$  curve. By smearing the reconstructed data point  $O_{data}$  within its uncertainty  $\sigma_{data}$ , we can perform pseudo experiments to obtain more measurements of  $\sin^2 \phi$ . The data points are smeared as Poisson distribution as most of the bin entries are below 10 counts. Measurements of  $\sin^2 \phi$  obtained from each pseudo experiment is then filled into a histogram as in Figure 4.32.

The uncertainty measurements of  $\sin^2 \phi$  can then be extracted from Figure 4.32 and are determined by fitting with a modified Gaussian as in Equation 4.4. Due

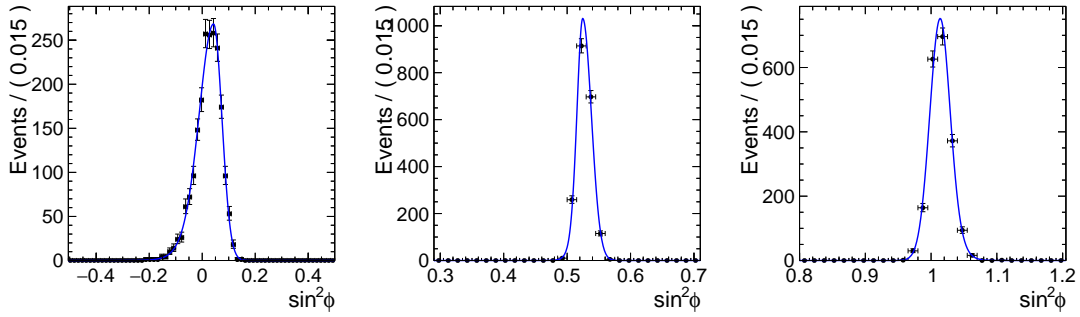


**Figure 4.32** *Pseudo experiments of  $\sin^2 \phi$  with (a) pure CP even  $\sin^2 \phi = 0$ , (b) 50% mixing of CP even and CP odd  $\sin^2 \phi = 0.5$ , (c) pure CP odd  $\sin^2 \phi = 1$ .*

to the definition of  $\sin^2 \phi$  in Equation 2.23,  $\sin^2 \phi$  value can only lie within 0 and 1. Therefore, uncertainty measurements of  $\sin^2 \phi$  near point  $\sin^2 \phi = 0$  will take  $\sigma_L$  and points near  $\sin^2 \phi = 1$  will take  $\sigma_R$ .

---

$\sin^2 \phi : 0 - 0.1$	$\sin^2 \phi : 0.2 - 0.8$	$\sin^2 \phi : 0.9 - 1$
$\Delta \sin^2 \phi = \sigma_R$	$\Delta \sin^2 \phi = \frac{FWHM}{2\sqrt{2 \ln 2}}$	$\Delta \sin^2 \phi = \sigma_L$

---

**Table 4.5** *Uncertainty estimation of  $\sin^2 \phi$  according to the definition of  $\sin^2 \phi$  for being within range  $[0,1]$ .*

### 4.9.7 Sensitivity to CP Properties of the Higgs Boson

By collecting all the uncertainty measurements presented above, we can compare the results between traditional method and new method of reconstructing neutrinos (described in Section 4.9.5) as well as old luminosity scheme with  $1.5 \text{ ab}^{-1}$  and new luminosity scheme with  $2.5 \text{ ab}^{-1}$  as shown in Figure 4.33(left). The improved neutrino reconstruction has increased the number of events passing the selection cuts and therefore improves the  $\Delta \sin^2 \phi$  measurements and has improved the results by around 20%. The new luminosity scheme with  $2.5 \text{ ab}^{-1}$  improves the  $\Delta \sin^2 \phi$  measurements in a similar way by having more  $t\bar{t}H$  signal events.

With the luminosity plan for  $2.5 \text{ ab}^{-1}$  ( $2 \text{ ab}^{-1}$  of  $+80\%$  electron polarisation and  $0.5 \text{ ab}^{-1}$  of  $-80\%$  electron polarisation), the precision of measuring  $\Delta \sin^2 \phi$  can be measured up to  $\Delta \sin^2 \phi \simeq 0.07$  with cross-section as an observable only from both semi-leptonic and hadronic channels. Adding an additional angular observable, the up-down asymmetry, can improve the precision up to  $\Delta \sin^2 \phi \simeq 0.03$  in the semi-leptonic channel.

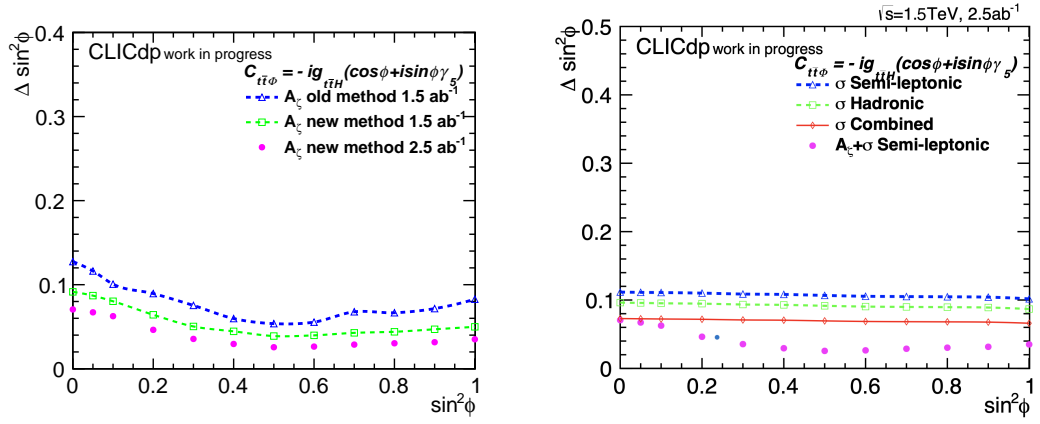


**Figure 4.33** Measurements of  $\Delta \sin^2 \phi$  by using template fit. (Left) Results are compared between new method of reconstructing neutrinos with no polarisation (green) and new luminosity scheme with polarised beam and  $2.5 \text{ ab}^{-1}$  (purple). (Right) Results of  $\Delta \sin^2 \phi$  extracted from cross-section measurements (dotted and straight lines) from both semi-leptonic channel and hadronic channel as well as results extracted from up-down asymmetry plus cross-section measurements from semi-leptonic channel (purple dots) with  $1.5 \text{ TeV}$  and  $2.5 \text{ ab}^{-1}$ .

#### 4.9.8 Other Observables

Further observables that are sensitive to the CP property of the Higgs boson can be combined to further improve the uncertainty measurement on the CP-mixing parameters. Examples like top polarisation and differential cross-section can be investigated in future [39].

### 4.10 Comparison with the LHC and Conclusion

The  $t\bar{t}H$  process was first observed with a significance over  $5\sigma$  in 2017 at the LHC [15]. Much more  $t\bar{t}H$  signals will be observed in the upcoming HL-LHC phase. The projected statistical precision on the top-Yukawa coupling from the LHC is expected to reach  $14\% - 15\%$  with  $300 \text{ fb}^{-1}$  of data and  $7\% - 8\%$  using  $3000 \text{ fb}^{-1}$  of data [85]. At a proposed linear  $e^+e^-$  collider, CLIC, the uncertainty of the top-Yukawa coupling can be lower to  $2.7\%$ . Hence, CLIC is a better option for precision measurements on the top-Yukawa coupling.

With the observation of  $t\bar{t}H$  over  $5\sigma$ , the LHC now has the access to this channel

to directly study the CP properties of the Higgs boson via  $t\bar{t}H$  process. A similar study on the CP properties of the Higgs boson is carried out by the ATLAS experiment at  $\sqrt{s} = 13$  TeV with  $139 \text{ fb}^{-1}$  [40].

The results show that a pure CP-odd coupling between the Higgs boson and top quark is excluded at  $3.9\sigma$ , and CP-mixing angle  $|\alpha| > 43^\circ$  is excluded at 95% CL [40]. The  $\kappa_t \sin(\alpha)$  in Equation 2.25 is similar to the notation that we used in Equation 2.23 where we used  $\phi$  for representing the mixing angle. From Figure 2.10, the uncertainty of  $\kappa_t \sin(\alpha)$  approximately equals 0.7. If assuming  $\kappa_t = 1$ , the ATLAS result can be translated into  $\Delta \sin^2(\alpha) \simeq 0.5$  whereas CLIC is able to achieve  $\Delta \sin^2(\alpha) \lesssim 0.07$ . This shows a significant advantage of using the CLIC machine for precision studies of the CP properties of the Higgs boson.

# Chapter 5

## The ATLAS ITk Pixel detector

CLIC is a future project to be approved and constructed. However, the HL-LHC phase of the LHC is due to operate in the next few years. It will provide us with much more data to study the  $t\bar{t}H$  process as well as potential discoveries for guiding the direction of physics in the future. In order to cope with the new challenging environment of the HL-LHC, the current detectors are upgrading and preparing for new measurements.

### 5.1 The Large Hadron Collider

The Large Hadron Collider (LHC) is world's largest circular collider with circumference of about 27 km spanning across the Franco-Swiss boarder near Geneva [43]. One of the motivations for building the LHC is to reach high enough energy to observe the Higgs boson.

The LHC primarily collides proton beams, but also collides heavy ions such as lead. A schematic of proton acceleration is shown in Figure 5.1. Proton sources are hydrogen atoms that are produced by stripping the electrons of the hydrogen gases using an electric field. The protons are first accelerated to 50 MeV by the linear accelerator LINAC2. The beam is then injected into the Proton Synchrotron Booster (PSB) to increase its energy to 1.4 TeV followed by the Proton Synchrotron (PS) to boost to 25 GeV. Then the proton beams accelerated further to 450 GeV inside the Super Proton Synchrotron (SPS) before entering the main ring of LHC. Two beams of protons are circulating in opposite directions

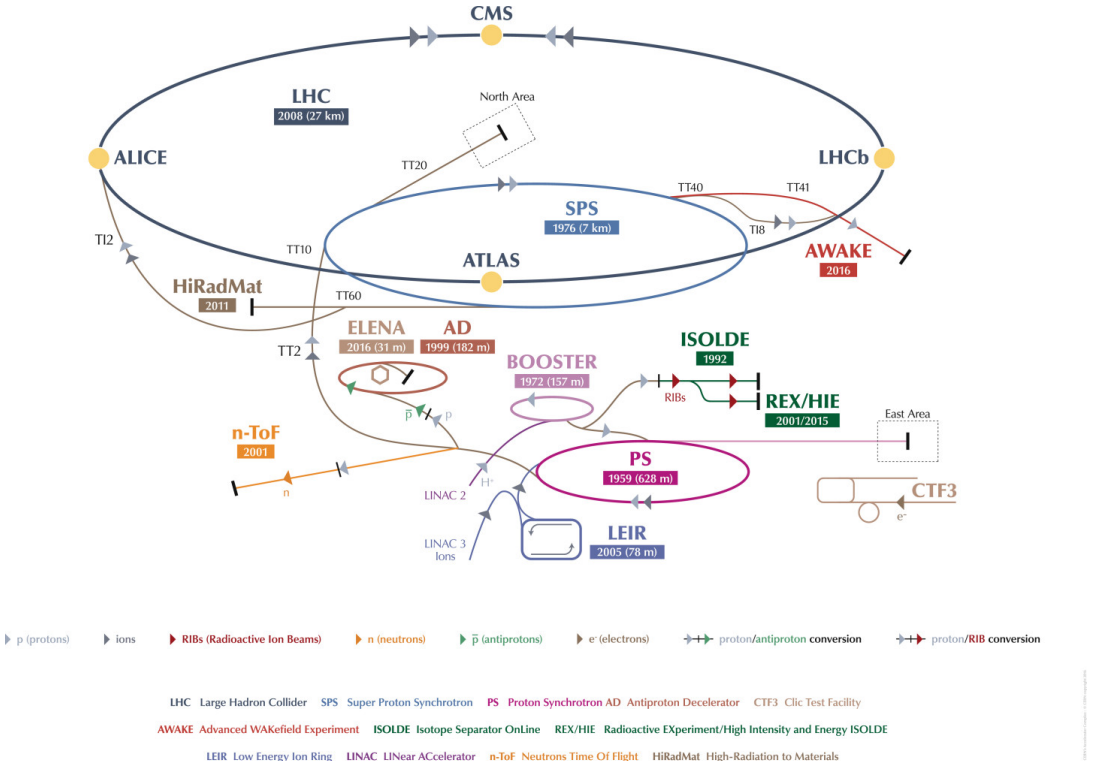


**Figure 5.1** *LHC accelerator complex [86].*

inside the main ring of the LHC to accelerate further to its maximum energy. The highest energy at which the LHC was operated by far reaches 6.5 GeV per proton beam, which results in a collision energy of  $\sqrt{s} = 13$  TeV. Each proton bunch consists of  $10^{11}$  hydrogen atoms and are accelerated with a bunch spacing of 25 ns which translates to a collision rate of 40 MHz.

The proton beams are brought to collision at four locations of the LHC main ring. Four major detectors have been constructed at these intersection points located 100 m beneath the ground, as illustrated in Figure 5.1. Each of the detectors focuses on specific fields of research which are all independent collaborations. Two general-purpose detectors, *A Toroidal LHC Apparatus* (ATLAS) and *Compact Muon Solenoid* (CMS), have the same direction of research but provide independent measurements for cross-checking each others' results. In 2012, both ATLAS and CMS collaborations announced the discovery of the Higgs boson that complete the last puzzle for the SM [4, 5]. Additionally, the *LHC-beauty* (LHCb) experiment specialises in measuring the parameters of CP violation from the interactions of *b*-hadrons in order to explain the matter-antimatter asymmetry in the universe. The last major detector, *A Large Ion Collider Experiment* (ALICE), is designed to study the heavy-ion (Pb) collisions

that is able to produce quark-gluon plasma. Such conditions are believed to have existed shortly after the Big Bang at which quarks and gluons are free before bounding together to form heavy particles. This will help us understand the history of the universe and reveal the mystery of the Big Bang. For this purpose, the LHC will collide heavy ions for a period of time during each run.

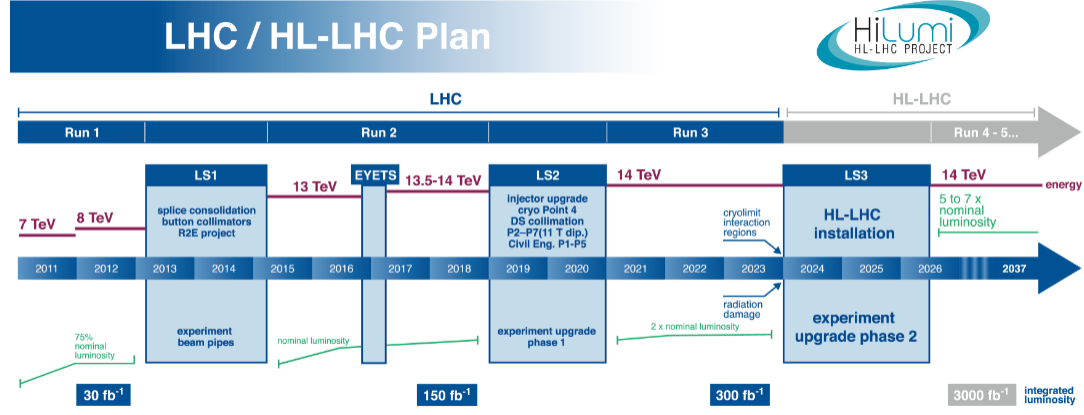


**Figure 5.2** Timeline of the LHC program. In Run 1 7-8 TeV with  $30 \text{ fb}^{-1}$ , Run 2 13-14 TeV with  $150 \text{ fb}^{-1}$ , Run 3 at 14 TeV with  $300 \text{ fb}^{-1}$  and finally HL-LHC at 14 TeV with  $3000 \text{ fb}^{-1}$  [87]

The LHC has a scientific program that spans over 20 years as shown in Figure 5.2. It is undergoing a series of upgrades which will eventually lead to an accumulated integrated luminosity for  $pp$  collisions of  $3000 \text{ fb}^{-1}$ . The necessary upgrades for achieving this performance will be realised during long shut downs where there will be no beams accelerating inside the LHC tunnel. Long Shutdown 3 (LS3) starting from the end of 2023 will implement major improvements of the accelerator as well as some of major detector components preparing for the *High-Luminosity LHC* (HL-LHC).

### 5.1.1 The ATLAS Experiment

The ATLAS detector is a general-purpose detector that measures a broad range of physics [88, 89]. It is world's largest particle detector and has a cylindrical shape with 46 meters in length, 25 meters in diameter and weights around 7000 tonnes. ATLAS is located at one of the intersection points of the proton beams at LHC close to the main CERN site at Meyrin, Geneva.

The detector is built around the collision point where proton beams collide as

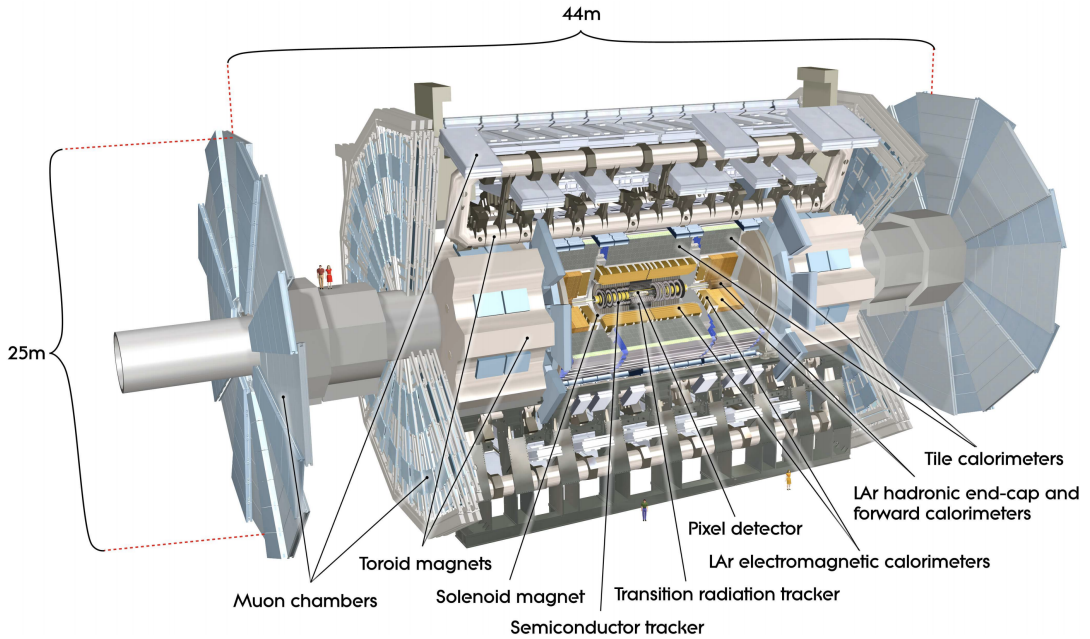


**Figure 5.3** Overview of the ATLAS detector [90].

illustrated in Figure 5.3. The current ATLAS detector has four major parts: the Inner Detector, the Calorimeters, the Muon Detectors and the Magnet Systems. In addition, ATLAS employs the Trigger and Data Acquisition system to select only interesting data for analysis from the huge amount of data produced from  $pp$  collisions.

The HL-LHC will present an extreme challenging environment for the ATLAS experiment. The anticipated increased luminosity, along with the associated high data rate and the damage from radiation will make the current ATLAS inner tracker inoperable. The Inner Detector currently used situated at the heart of ATLAS will be replaced with a new all-silicon tracker to maintain tracking performance under a high-occupancy environment and resist the much higher integrated radiation.

### 5.1.2 Coordinate System

The ATLAS detector is described by a common coordinate system. The origin is situated at the IP in the centre of the detector. The z-axis is along the beam line while the x-y plane is perpendicular to the beam direction and is called the transverse plane. The azimuth angle  $\phi$  is defined around the beam axis and polar angle  $\theta$  is defined from the beam line. The positive x axis is pointing from the IP to

the centre of the LHC while the positive y axis pointing upwards. Pseudorapidity,  $\eta$ , an additional parameter used to describe the angle of a particle relative to the beam axis is defined as

$$\eta = -\ln\left(\tan\frac{\theta}{2}\right). \quad (5.1)$$

The value of  $\eta = 0$  represents the perpendicular direction to the beam axis and  $|\eta| = \infty$  describes direction along the beam axis. In hadron collider physics, pseudorapidity is a preferred parameter as particle flux is constant as a function of pseudorapidity at IP.

The ATLAS detector provides a hermetic coverage in  $\phi$  up to  $|\eta| = 2.7$ . Sub detectors extend the range to cover more physics data along the beam line, e.g. the ECAL extends to  $|\eta| = 3.2$  and the HCAL to  $|\eta| = 4.9$ .

## 5.2 The ATLAS Inner Tracker

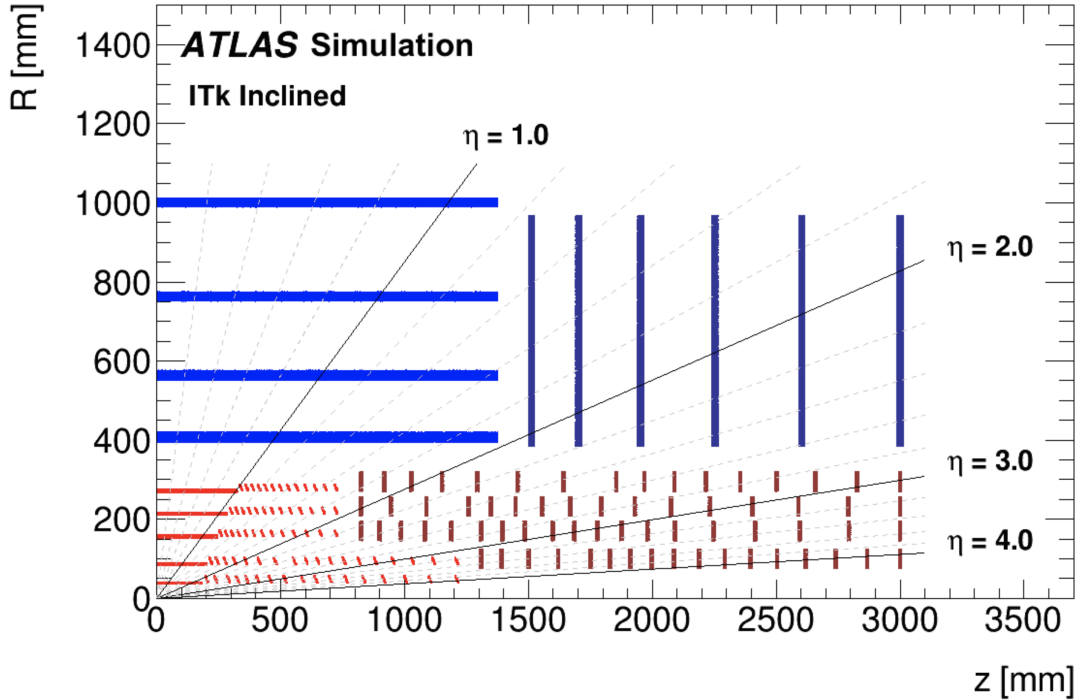


**Figure 5.4** Schematic layout of the ATLAS ITk tracker for the HL-LHC phase. Only one quadrant and only active detectors elements are shown here. The horizontal axis,  $z$ , is the axis along the beam direction with zero being at the interaction point. The vertical axis,  $R$ , is the radius of the detector measured from the interaction point. [91]

The new ATLAS Inner Tracker (ITk) is designed for 10 years of operation at HL-LHC environment with instantaneous luminosity of  $\mathcal{L} = 7.5 \times 10^{34} \text{ cm}^{-2}\text{s}^{-1}$ , 25 ns between bunch crossing and an integrated luminosity of  $3000 \text{ fb}^{-1}$ [91]. It will replace the existing Inner Detector.

The ITk detector is built around the interaction point with cylindrical silicon detectors around the beam axis up to the solenoid bore. The innermost part has five layers of pixel detectors followed by two short-strip paired stereo modules and then two-long paired stereo modules. Six strip disks and a number of pixel rings will be positioned at the forward regions. A schematic layout of the ITk detector is shown in Figure 5.4. The total silicon surface of pixel detector will be almost ten times of current detector reaching about  $13 \text{ m}^2$ .

Despite higher particle density in the HL-LHC, the current level of occupancy per pixel can be maintained by reducing the pixel size from  $50\mu\text{m} \times 250\mu\text{m}$  and  $50\mu\text{m} \times 400\mu\text{m}$  to  $50\mu\text{m} \times 50\mu\text{m}$  or  $25\mu\text{m} \times 100\mu\text{m}$ . The thickness of planar sensors are also reduced from 200  $\mu\text{m}$  and 250  $\mu\text{m}$  to 100  $\mu\text{m}$  and 150  $\mu\text{m}$ . This reduces the required bandwidth for the readout of data. Furthermore, it also leads to an increased radiation tolerance and reduced power dissipation as lower bias voltage is required for operation and leakage current is reduced.

## Sensor Technologies

Silicon pixel and strip sensors are used for detecting charged particles. As a charged particle passes through the sensor area, electrons and holes are created from ionisation. These electrons and holes drift towards the n and p junction by the electric field for readout.

Different silicon sensor technologies will be implemented in the pixel detectors (Figure 5.5) to cope with the requirements for HL-LHC to balance the required radiation tolerance and production costs. The planar sensor uses a n-in-p technology as sketched in Figure 5.6(left) which makes it easy to handle and fast in production (low cost). The 3D-sensor has n-type and p-type pillars built vertically across the sensor as shown in Figure 5.6(right). This kind of structure provides a better radiation tolerance compare to planar sensors due to the shorter collection distance. However, the complex structure makes the production process much longer and more expensive than the planar sensors. Therefore, 3D silicon sensors are employed in the innermost layer of the pixel detector and planar silicon

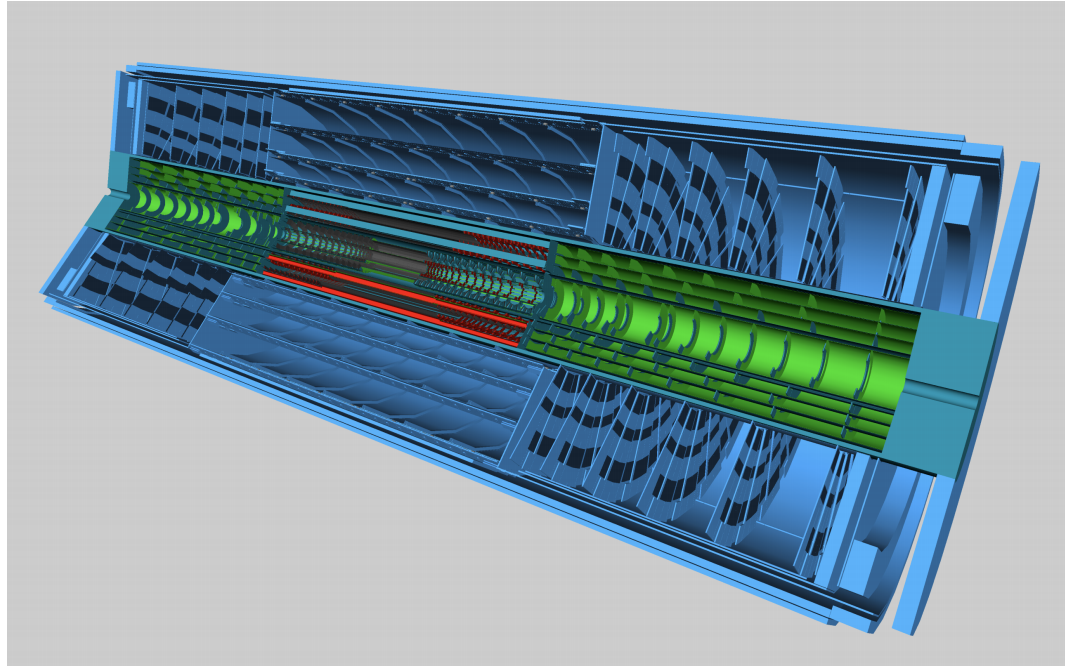


**Figure 5.5** Schematic layout of the ATLAS ITk tracker for the HL-LHC phase. [92]

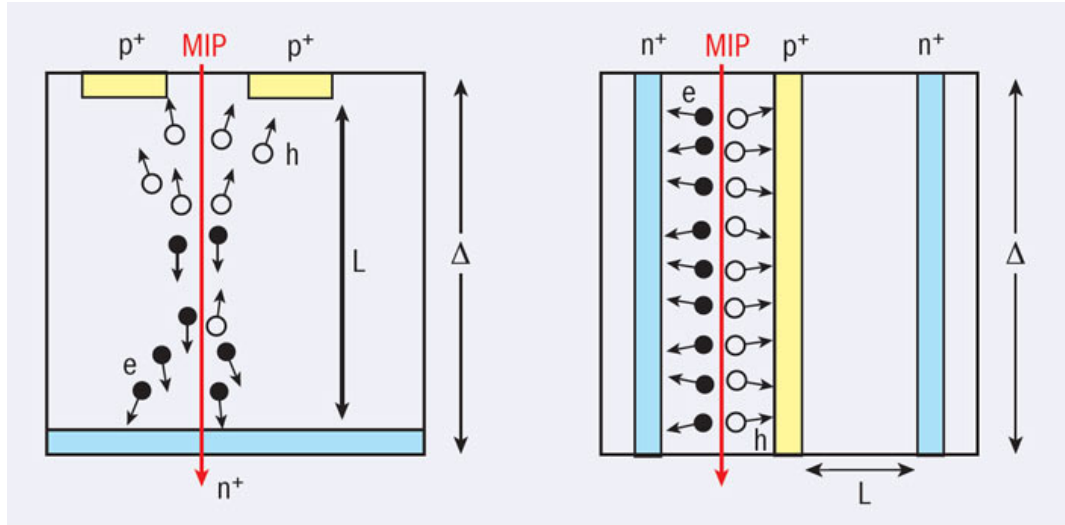


**Figure 5.6** Schematic cross-sections of (left) a planar sensor design and (right) a 3D sensor, showing how the active thickness ( $\Delta$ ) and collection distance,  $L$ , are decoupled in the latter.  $p^+$ ,  $n^+$  means  $p$ -doped and  $n$ -doped [93].

sensors with thickness between  $100 \mu\text{m}$  and  $150 \mu\text{m}$  are used in the remaining layers.

A new type of Front End (FE) chip, RD53A, has been developed by the RD53

collaboration [94] using 65 nm CMOS technology for the ATLAS and CMS experiments at the HL-LHC. The performance of RD53A chip is designed to be low noise rate with low threshold (less than  $10^{-6}$  at a threshold of  $600\text{ }e^-$ ) with a data transmitting rate of 1.28 Gbps. The characteristics and features of the RD53A chip such as efficiency is evaluated by testbeam and the results are represented here.

## 5.3 Test Beam Facility

A test beam provides a realistic environment for measurements of the property and performance of a prototype module, RD53A. Particles are accelerated, focused and directed into a test beam telescope. A telescope consists of several well-known pixel sensors, these are used to reconstruct the trajectory of the test beam particles, and the hit position of the particles can be interpolated for the device under test (DUT). With these information, the DUT can then be studied further and properties like hit efficiency can be determined.

The test beam measurements for this study is performed at the German Electron Synchrotron (DESY) in December 2018 with EUDET telescope [95]. The EUTelescope software is used to reconstruct the tracks of particles and the TBMon2 framework is used to do the final analysis for the DUT [96–98].

### 5.3.1 DESY

The DESY II synchrotron situated in Germany operates an electron-positron accelerator with energies up to 7 GeV. It feeds high energy electron and positrons into the storage rings DORIS and PETRA as well as the testbeam facility. The primary beam generates bremsstrahlung photons by hitting a  $25\text{ }\mu\text{m}$  thick carbon-fibre target. These photons consequently convert into electron-positron pairs by a metal converter target. A dipole magnet spreads out the electron and positron beams into a horizontal fan. The final beam is sliced with a collimator and directed to the experiment areas as shown in Figure 5.7. The final beam has a particle energy range of 1-6 GeV with a 5% energy spread and an angular divergence of 5 mrad [99].

A beam energy of around 4 GeV is usually selected to ensure a good compromise of

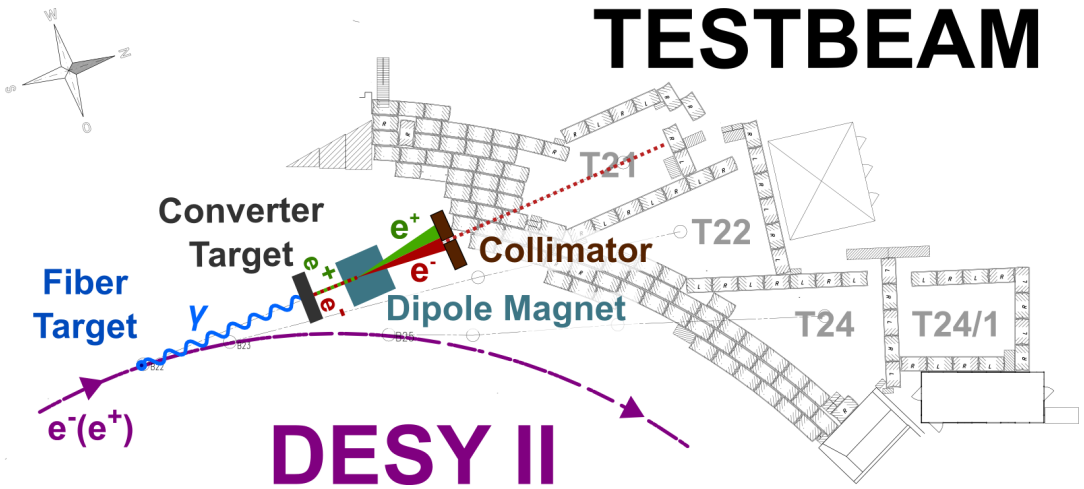


**Figure 5.7** Schematic layout of DESY testbeam facility indicating the beam generation process.

intensity and energy. At low energies, the telescope space-resolution deteriorates as particles deviate from its original trajectory when passing through matter due to Coulomb scattering.

### 5.3.2 The EUDET Telescope

The EUDET telescope consists of 6 sensor planes using MIMOSA 26 monolithic active pixel devices sitting on two arms with one DUT in the middle and a reference plane at the far end of the telescope as shown in Figure 5.8 and 5.9. The geometry defines the telescope resolution. The highest resolution depends on the beam energy and the thickness of the DUT. Therefore, different DUTs have specific configuration. For the RD53A, the first three MIMOSA planes are placed 100 mm apart while the last three MIMOSA planes together with the reference planes FE-I4 are sitting 50 mm apart. The DUT is placed 100 mm after the third MIMOSA plane and 180 mm before the forth MIMOSA plane.

After alignment, DUTs are placed inside a light-weight Styrofoam cooling box for taking measurements at a low temperature. Temperatures below  $-50^{\circ}\text{C}$  are achieved with dry ice blocks. The dry ice is replaced every few hours to maintain low temperature environment for measurements.

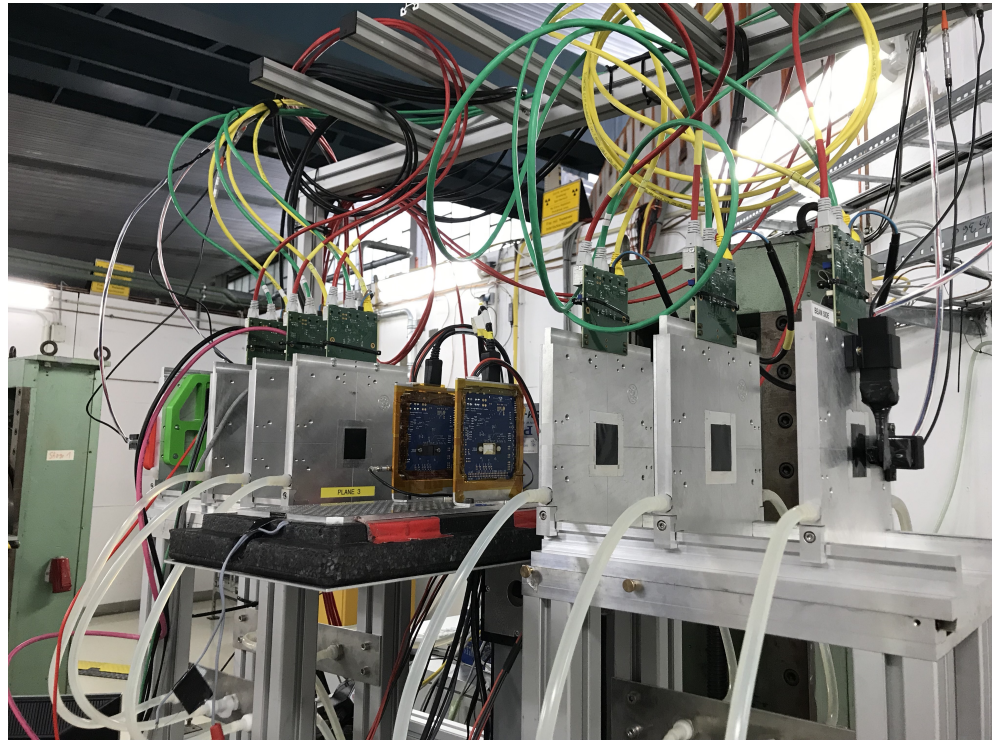


**Figure 5.8** *Photograph of the EUDET telescope at DESY with 6 MIMOSA26 planes and one DUT in the middle and a reference plane FE-I4 at the far end. This picture is taken on a different testbeam which had a different setup.*

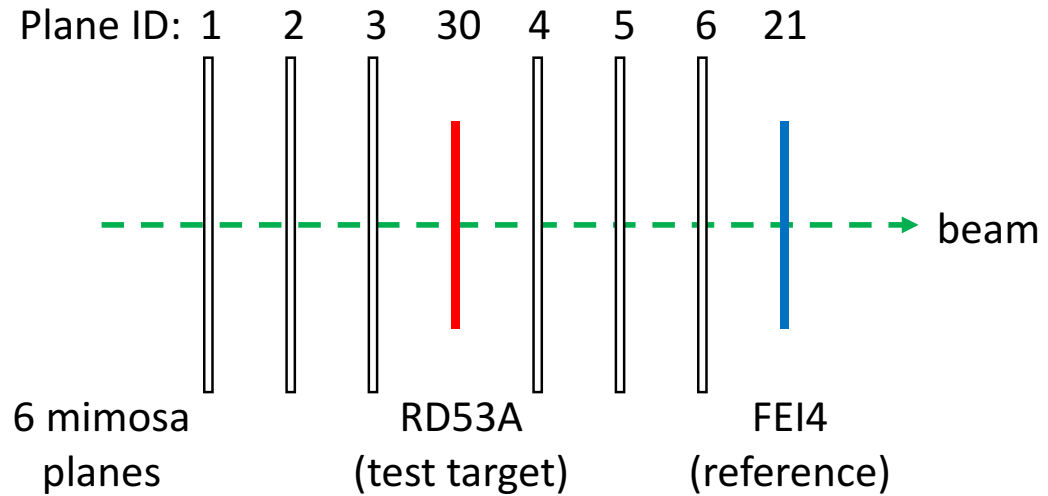


**Figure 5.9** *Schematic of the EUDET telescope setup (not to scale). Plane 1-6 are MIMOSA Planes, Plane 30 is the DUT (RD53A), Plane 21 is the reference plane (FE-I4).*

## 5.4 Track Reconstruction

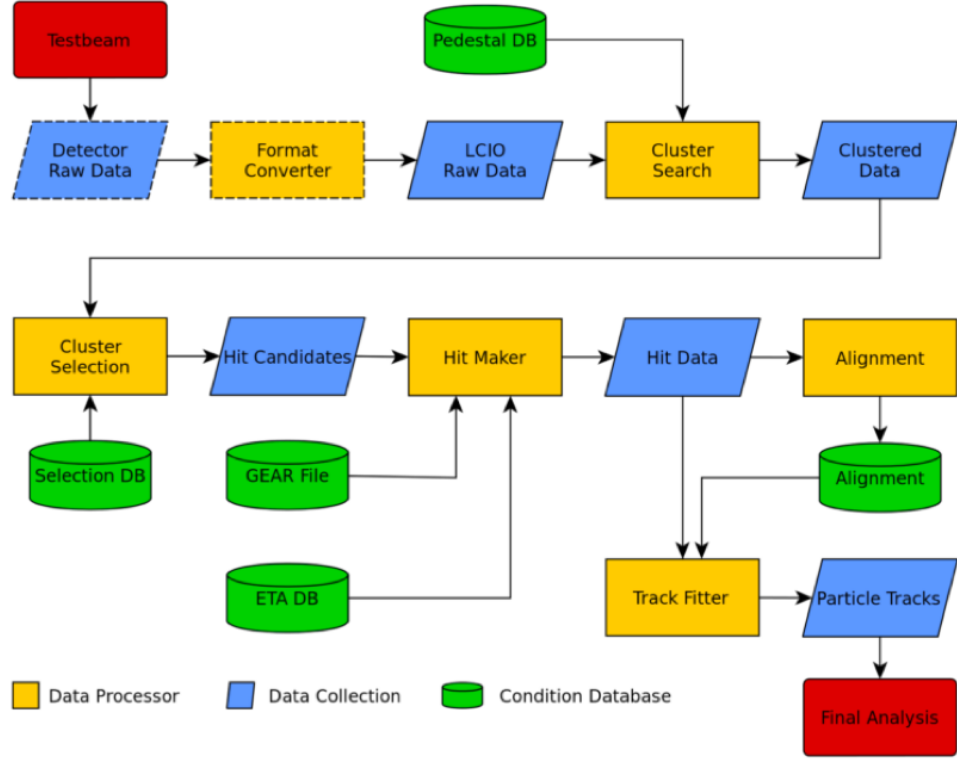


**Figure 5.10** Framework of EUTelescope consisting of five steps: data conversion, clustering, hit making, alignment and track fitting.

Tracks are reconstructed using the EUTelescope software framework [100] from raw telescope data. The construction consists of five steps: data conversion, clustering, hit making, alignment and track fitting as illustrated in Figure 5.10. After processing all steps, the data is ready to perform post-reconstruction analysis.

### Data Conversion

Raw data from the telescope is decoded into LCIO (linear collider input/output) format for further reconstruction and analysis in the first step. This is achieved by using the Native Reader provided by EUDAQ software. Firing frequency cuts are used to identify the noisy pixels in the MIMOSA planes, FE-I4 and DUT and the noisy pixels will be masked in the clustering step.

## Clustering

The clustering step converts single hits into clusters. In each plane, pixels that are hit by the same incident particle are grouped together to form clusters. The constrained cluster size can pick which hits belong to the same cluster. The identified noisy pixels are masked in this step.

## Hit Maker

In this step, the global hit position of the clusters is obtained. Clusters are converted to hit information. Correlations plots between hits and neighbouring planes are obtained to allow a prealignment of the telescope. This allows us to check the positions and rotation of the DUT and reference plane (FE-I4). In the prealignment, positions of the hits are compared between different planes to minimise the difference between planes as shown in Figure 5.11. A new gear file which describes the geometry of the DUT will be produced in this step. A fine alignment of the telescope is made in the next step.

## Alignment

The position of the sensors needs to be known more accurately than just using mechanical measurements. The tracks are fitted by comparing the grouped hits among all planes. The distance between the fitted tracks and the point of hits in each plane, known as the residual, is determined to find the right parameters for alignment. This is performed by using a  $\chi^2$  minimisation from the `MillepedeII`. Goodness-of-the-track is tuned with this  $\chi^2$  cut. The reconstructed tracks are shifted by the offset value calculated from the difference between the residuals and hit positions.

The alignment is performed few times. Each iteration gives a better starting point in guessing the alignment position.

## Track Fitting

After the alignment, an entire reconstruction chain needs to be performed with the full dataset and the new aligned geometry. All step excluding alignment

has been rerun with an additional track fitter step at the end to reconstruct the tracks. A root file is produced for post-reconstruction analysis.

The tracks are obtained only using the MIMOSA planes, and the track positions in the DUT are extrapolated. This avoids any bias to the track position by excluding the hit information from the DUT. The mean of the residuals should be close to 0 if the alignment is correct. A misalignment can be observed if the mean deviates from 0.

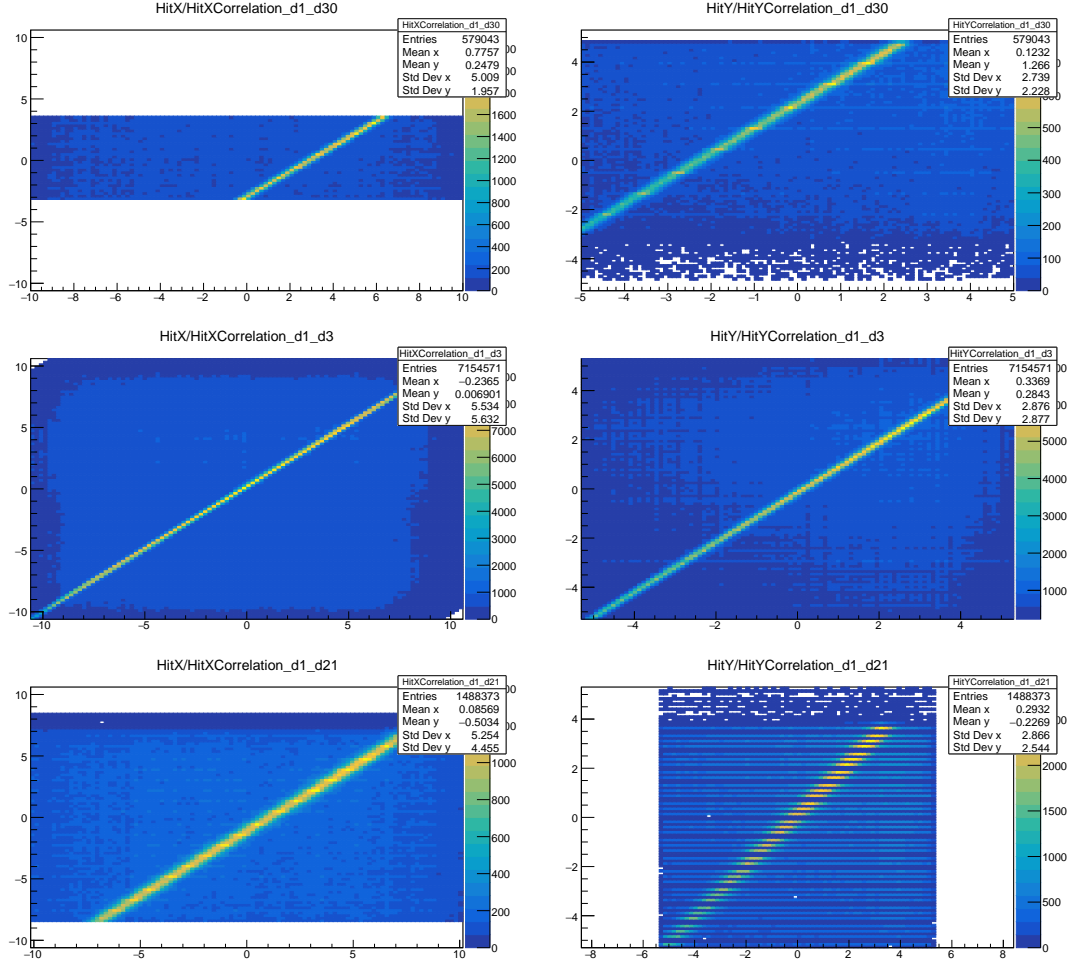


**Figure 5.11** Correlation plots from the hit maker step of the first MIMOSA plane d1 with RD53A d30 (top), third MIMOSA plane d3 (middle) and reference plane FE-I4 d21 (bottom). Mismatch of pitch size gives artificial structure, obvious in plane FE-I4.

## 5.5 Post-Reconstruction Analysis

A post-reconstruction analysis framework, **TBMon2** [101], is used to extract properties of the DUTs such as hit efficiencies from the reconstruction data. The track and hit information from **EUTelescope** are analysed to match hits with tracks. It is considered inefficient if a hit is matched with a track and the track has no corresponding hit.

### 5.5.1 **TBmon2**

After the adjustment of the reconstructed track position, several criteria are applied to the selection of good tracks. An important one is if the track is matched. Matched means that an interpolated track is associated with a hit in pixel within a certain range. Additionally, a matched track in the reference plane, FE-I4, is required. After a trigger signal is send by the two scintillators located on the telescope, the active time window of DUT and telescope are different. The readout time of the MIMOSA planes is about  $112\ \mu\text{s}$  whereas the DUT readouts every 25 ns. As a result, each track that passes through the MIMOSA planes can be associated with multiple hits in the DUT (less readout time). Therefore, a reference plane is needed to ensure a time stamp to allow the track in the MIMOSA planes to match with the hit on the DUT. FE-I4 with  $16 \times 25\ \text{ns}$  (16 bits) readout time is used for this purpose. Only tracks within the active time of the FE-I4 are considered for analysis.

The selection criteria of a good track is summarised as follows (selecting from matched track):

- A matched track in the reference plane is required to be within the active time span of the FE-I4 readout chip.
- The  $\chi^2$  of the track fit needs to be below a certain value to assure a good track fit quality. The default value is set to be 15.
- The track is required to not hit a masked pixel to affect the total cluster charge.
- The track needs to be in the central region and not near an edge pixel.

**TBMon2** uses these information to perform several analyses for the DUT. One of the most important one is the hit efficiency of the DUT.

## 5.6 Properties of RD53A

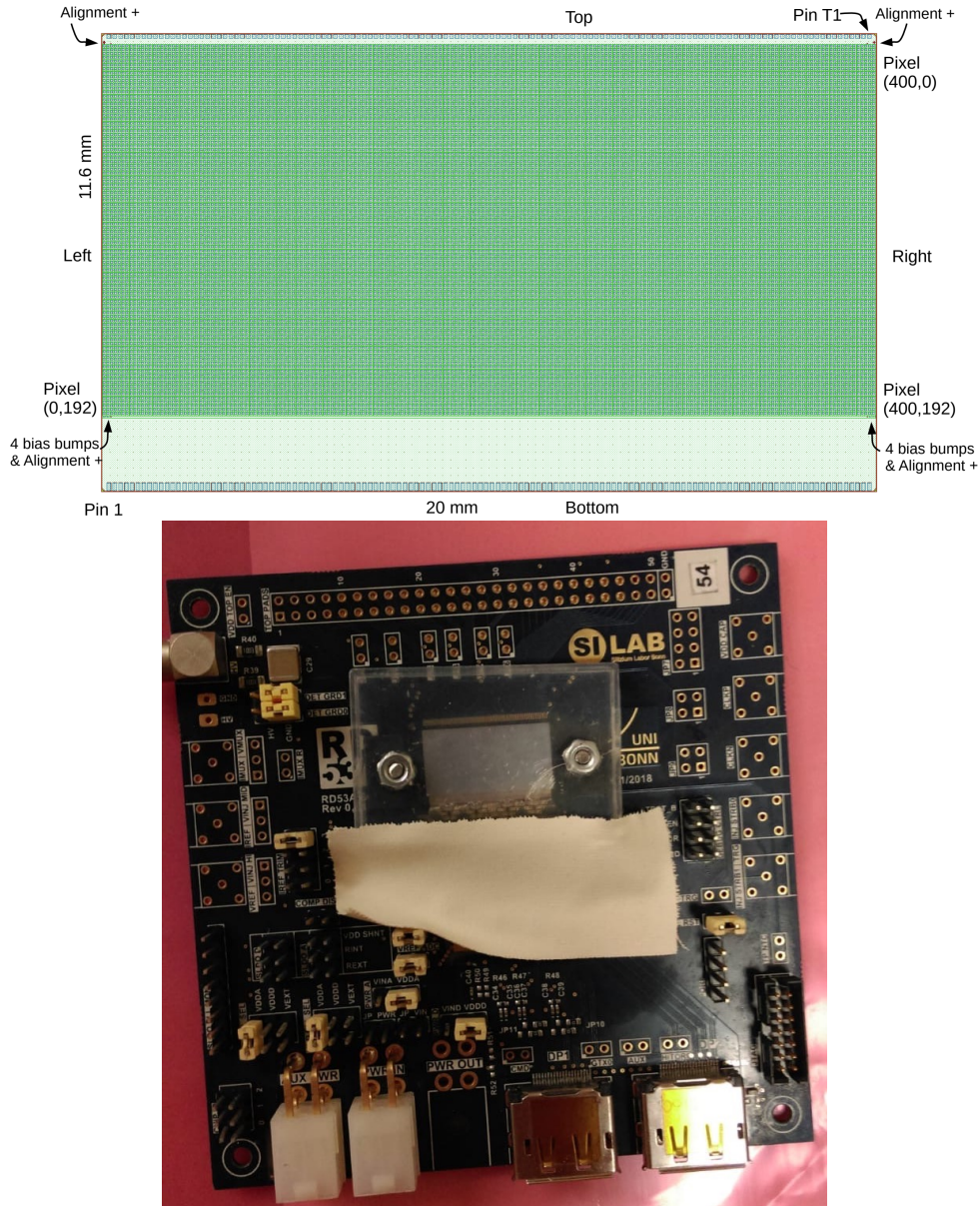


**Figure 5.12** RD53A layout from top view. The height is 11.6 mm and 192 pixels, and the width is 20.0 mm and 400 pixels [94].

The DUT in this thesis uses one of RD53A prototypes, UK module 3292-01-45. It is arranged as a matrix of  $192 \times 400$  pixels with cell size of  $50 \mu\text{m} \times 50 \mu\text{m}$  and a total active area of  $20.0 \mu\text{m} \times 11.8 \mu\text{m}$  with thickness of  $150 \mu\text{m}$  as illustrated in Figure 5.12. Data used in this analysis is taken from testbeam runs in December 2018 at DESY with a bias voltage of 400 V and threshold of 1027 e.

### 5.6.1 Residual

Transverse momentum ( $p_T$ ) of charged particles is one of the most important measurements in physics analysis and BSM searches. Therefore, a precise measurement in the x-y direction of RD53A is prioritised compared to z direction.

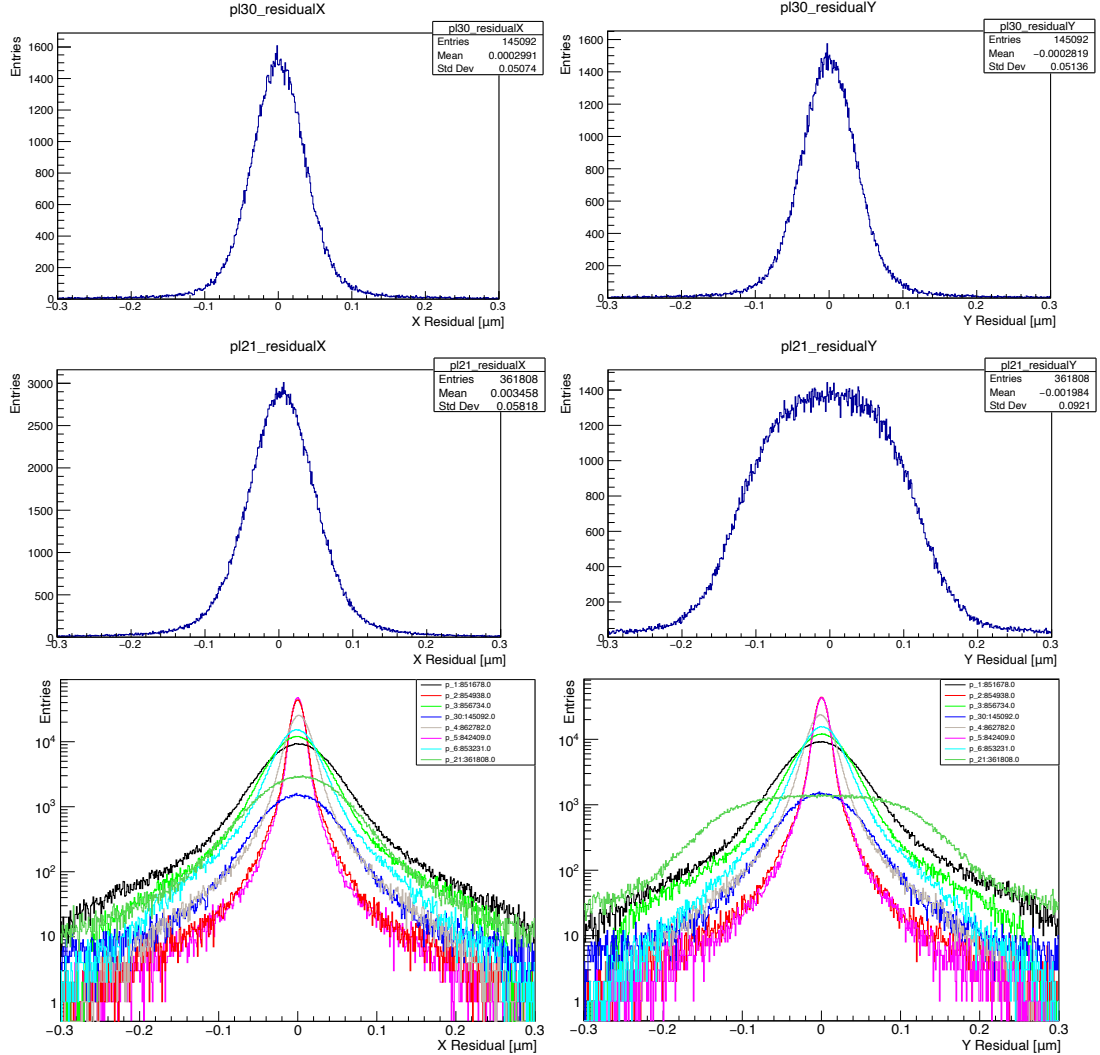


**Figure 5.13** Residuals for RD53A (top), FE-I4 (middle) and all MIMOSA planes (bottom) after track reconstruction.

Figure 5.13 presents the residuals of hits to fitted tracks on RD53A ( $50\mu\text{m} \times 50\mu\text{m}$ ), FE-I4 and all 6 MIMOSA Planes. The resolution, extracted standard deviation of the residual distribution, is achieved by folding the device itself with uncertainties coming from the beam telescope and other experimental sources such as multiple scattering. The resolution for a pixel detector with pitch size  $p$  can be calculated

as [102]

$$\sigma_{position} = \frac{p}{\sqrt{12}}. \quad (5.2)$$

Table 5.1 summarises the theoretical and measured resolutions of RD53A and FE-I4 with corresponding pitch sizes. The experimental resolution is bigger than the theoretical prediction as it includes both telescope and experimental uncertainties. One of the reasons is due to the non-ideal operation such as bias and threshold settings. The effect from multiple scattering also affects the efficiency calculation of the DUTs, especially with relatively low momentum particles from DESY testbeam facility ( $\approx 5$  GeV electrons).

DUT	Pitch [ $\mu\text{m}$ ]	Theoretical resolution [ $\mu\text{m}$ ]	Experimental resolution [ $\mu\text{m}$ ]
FE-I4	50 (x)	14.4	58.2
	250 (y)	72.2	92.1
RD53A	50 (x)	14.4	50.7
	50 (y)	14.4	51.3

**Table 5.1** *Residual values of RD53A and FE-I4. Theoretical resolution is calculated using Equation 5.2.*

## 5.6.2 Efficiency

The DUT hit efficiency is calculated by the number of good tracks with matched DUT hit divided by the total number of good tracks and is calculated per pixel and overall efficiency. There are two parameters directly affect the efficiency calculation. One of the controlling parameter is the MatchX/Y in the config file, this opens a window with a certain size around the cluster centre when assigning a track to a cluster. And a good track is the one that minimises the distance to the cluster centre. Another parameter is the MatchPixelMargin which opens a global window around the pixels by checking the tracks that passes through. This allows us to study the edge efficiency. The size of the window is calculated as `pixel_size+MatchPixelMargin`. Increasing this parameter leads to an increase in the number of good tracks. However, too large of this value could lead to allow far tracks to pass the selection which leads to high rate of mismatching.

To make a fair comparison with other measurements of different bias voltage, a suitable combination of the settings need to be pre-defined. The MatchX/Y is set to have a size of double the pitch size and the MatchPixelMargin is set to be half of the pitch size. For RD53A with pitch size of  $50 \mu\text{m}$ , the MatchX/Y are set

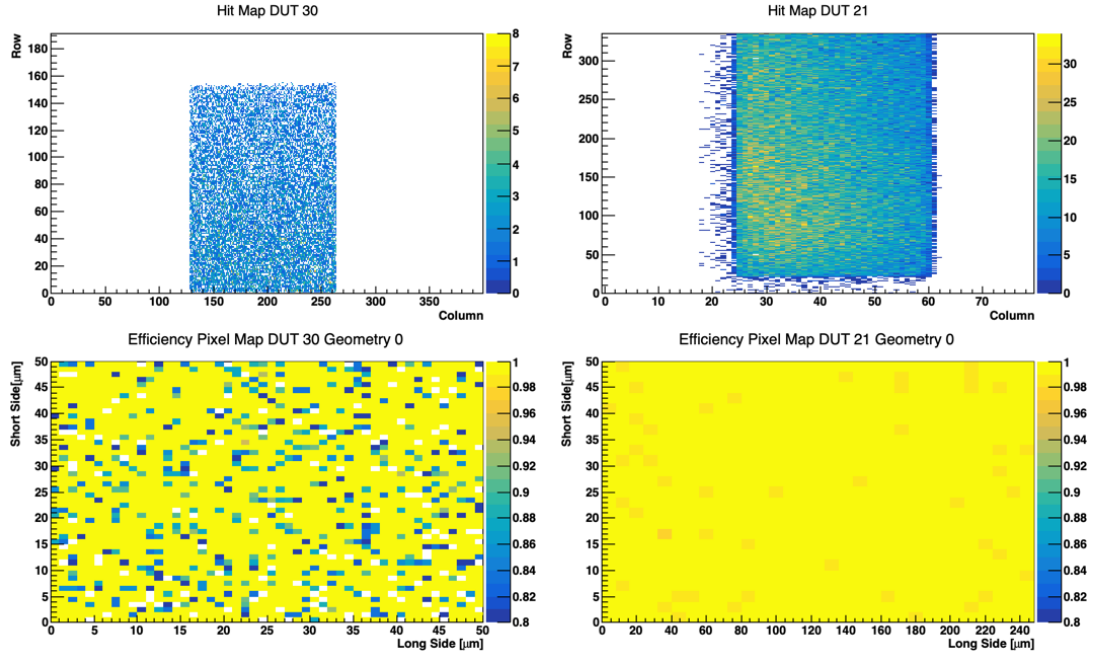


**Figure 5.14** Top two are the hit maps for RD53A (DUT30) and FE-I4 (DUT21), bottom two are the in pixel efficiency maps. This is for run 457, bias = 400V, with RD53A as DUT and FE-I4 as reference/timing plane.

to 100  $\mu\text{m}$  and MatchPixelMargin are set to 25  $\mu\text{m}$ . The track and hit matching is set to be below 15.

Hit maps and efficiency pixel maps of DUT RD53A and reference plane FE-I4 are shown in Figure 5.14 (single run) and Figure 5.16 (all runs). As shown in Figure 5.15, efficiencies of both RD53A and FE-I4 remains constant for a consecutive measurements with the same bias voltage and threshold. Using data collected at bias voltage of 400 V and a threshold of 1027 e in December 2018 at DESY, the overall efficiency of DUT RD53A is measured to be 97.65% and the efficiency of reference plane FE-I4 is measured to be 99.86% as summarised in Table 5.2. The results have met the required hit efficiency of >97% at 400V for  $2 \times 10^{15} \text{ n}_{eq}/\text{cm}^2$  for an irradiated device with a thickness of 150  $\mu\text{m}$ .

DUT	Tracks	Tracks w/ hit	Efficiency	Uncertainty
RD53A	190967	186482	97.651%	0.035%
FE-I4	1099920	1098390	99.861%	0.004%

**Table 5.2** Efficiencies of RD53A and FE-I4 measured from test beam data (all runs) collected at bias voltage of 400V in December 2018 at DESY.

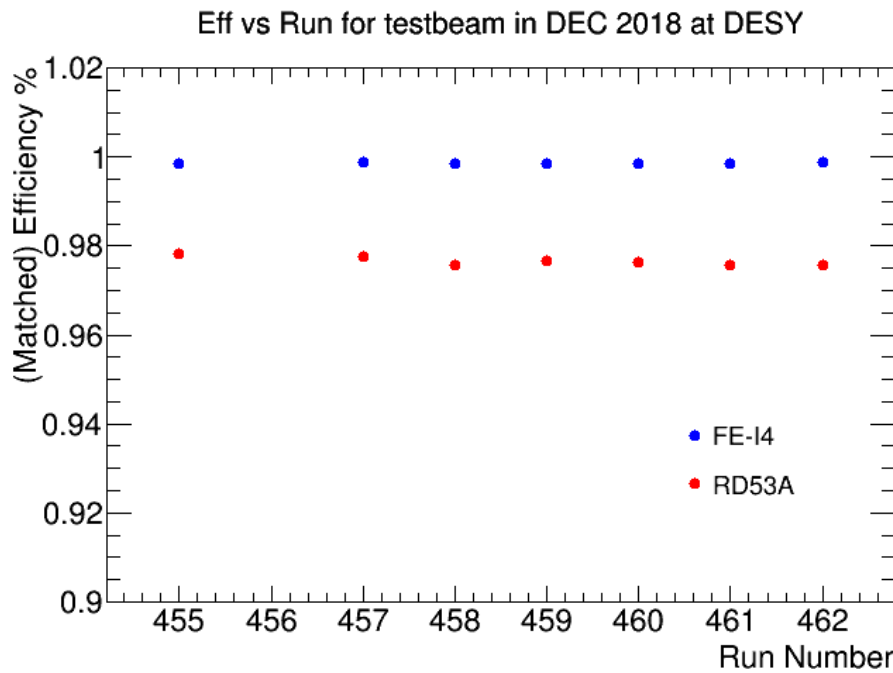


**Figure 5.15** *Efficiencies against run numbers for testbeam data collected in December at DESY with bias voltage of 400V. The uncertainties of efficiencies are too small to be shown on plots.*

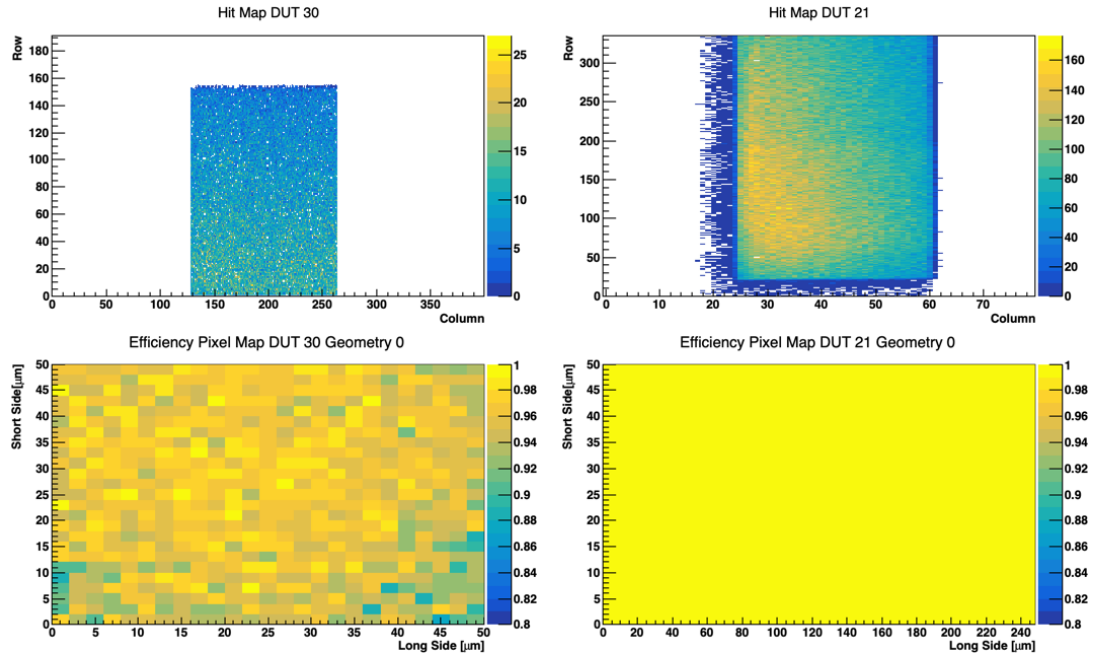


**Figure 5.16** *Top two are the hit maps for RD53A (DUT30) and FE-I4 (DUT21), bottom two are the in pixel efficiency maps (larger bins) for all runs with bias voltage of 400V, with RD53A as DUT and FE-I4 as reference and timing plane.*

## 5.7 Outlook from the Results

Hit information from the RD53A are successfully reconstructed into tracks using the `EUTelescope` software framework. After telescopes alignment, the residuals of DUT RD53A are measured to be  $50.7 \mu\text{m}$  in x-direction and  $51.3 \mu\text{m}$  in y-direction. The experimental resolution is bigger than the theoretical prediction as it includes both telescope and experimental uncertainties such as the non-ideal operation of the telescopes and the effect from multiple scattering.

Reconstructed track information are evaluated using the `TBmon2` analysis software. Tracks are selected through various criteria and matched hit information to the reference plane FE-I4. The overall efficiency of RD53A is measured to 97.651% with an uncertainty of 0.035%. The efficiency of the reference plane, FE-I4, is measured to be 99.861% with an uncertainty of 0.004%. Result shows a high consistency for a consecutive data taking runs whilst retaining high efficiency and meeting the hit efficiency requirement for the HL-LHC.

Overall, the preliminary results from the UK RD53A module successfully passed the requirement for the HL-LHC phase. However, the study of the RD53A module is still during the R&D phase, meaning that sensor design, reconstruction and analysis softwares are still under development. Next step that is currently being carried out by the UK RD53A group is to improve the reconstruction software. The improvement will directly reflect on the reduced residual value of the testing module. Different designs of RD53A modules will be tested for market survey research.

# Chapter 6

## Summary and Conclusion

A proton-proton collider is able to reach a much higher collision energy and luminosity than an electron-positron collider, therefore it is usually used for discovery of new particles. In contrast, an  $e^+e^-$  collider has relatively lower luminosity but its collision environment is much cleaner with well-defined initial states. This allows a more precise measurement of physics quantities. Although a circular  $e^+e^-$  collider retains high luminosity, it will reach a limited collision energy due to bremsstrahlung loss. In order to achieve higher collision energy, linear  $e^+e^-$  colliders are a more favourable option by extending tunnel length or increasing acceleration gradient. CLIC is one of the proposed projects for this purpose to make precise measurements of SM physics and potentially observe evidences from BSM.

As the  $t\bar{t}H$  physics process is first observed in 2017 [103], the next physics goal would be to make precise measurement of  $t\bar{t}H$  process to extract more information about the Higgs boson. The second phase of the CLIC experiment, with collisions at 1.5 TeV, allows the production of  $t\bar{t}H$ . In this thesis, the analysis is performed with fully-hadronic and semi-leptonic channels of  $t\bar{t}H$  which account for  $\sim 91\%$  of total  $t\bar{t}H$  cross-section. The analysis uses **MARLIN** for event reconstruction and **TMVA** for event selection. The uncertainty of measurement on the  $t\bar{t}H$  cross-section is determined to  $\Delta_{\sigma(t\bar{t}H)} = 7.5\%$  with unpolarised beam and an integrated luminosity of  $1.5 \text{ ab}^{-1}$  at  $\sqrt{s} = 1.4 \text{ TeV}$ . With polarised beams and an integrated luminosity of  $2.5 \text{ ab}^{-1}$  ( $80\%$  of  $P(e^-) = -80\%$  and  $20\%$  of  $P(e^-) = +80\%$ ) at  $\sqrt{s} = 1.5 \text{ TeV}$ , the uncertainty of cross-section is improved to  $\Delta_{\sigma(t\bar{t}H)} = 5.37\%$ . The uncertainty on the top-Yukawa coupling measurement

is deduced using factor  $\kappa = 0.5032 \pm 0.0005$  (Equation 4.8) giving a value of  $\sigma_{g_{t\bar{t}H}} = 2.7\%$ . Comparing to HL-LHC projection of 7%-8% with  $3000 \text{ fb}^{-1}$ , the CLIC experiment is able to measure more precisely on the top-Yukawa coupling to study the properties of Higgs boson.

High precision measurement of the  $t\bar{t}H$  process gives us a great window to study CP properties of Higgs boson. In the  $e^+e^- \rightarrow t\bar{t}\Phi$  process, where  $\Phi$  is the CP-mixing Higgs boson, the total cross-section decreases linearly as the amount of CP-odd Higgs increases as shown in Figure 4.24. With the proposed CLIC luminosity scheme of  $2.5 \text{ ab}^{-1}$  and polarised beam, the contribution from pure CP-odd Higgs can be measured to  $\sim 7\%$  accuracy at  $1\sigma$  (Figure 4.33) with cross-section as an observable. The CP properties of Higgs can be measured more precisely with additional observables, e.g. up-down asymmetry  $A_\zeta$ . This can further improve measurement of CP-mixing angle to  $\Delta \sin \phi^2 \simeq 0.03$ . Additional observables can further improve the sensitivity to CP-mixing angle. In conclusion, the CLIC experiment would be an ideal tool for making precise measurements and has great potential to search for physics beyond the SM.

While waiting for approval of the CLIC experiment, the LHC is upgrading to HL-LHC for a much higher luminosity (up to  $3000 \text{ fb}^{-1}$ ) whilst keeping the same collision energy of  $\sqrt{s} = 14 \text{ TeV}$ . In order to cope with the new collision environment, one of the most important tasks of the ATLAS experiment is to upgrade its Inner Detector to a full-silicon Inner Tracker (ITk).

A new front end chip, RD53A, has been developed by the RD53 collaboration to be implemented in the ATLAS ITk pixel sensor system using 65 nm CMOS technology. Properties of a UK RD53A module with cell size of  $50 \times 50 \mu\text{m}^2$  are tested with testbeam dataset collected in December 2018 at DESY using EUDET telescope. Residuals of this chip is found to be symmetrical with  $50.7 \mu\text{m}$  in x-axis and  $51.3 \mu\text{m}$  in y-axis. Although the theoretical resolution is  $14.4 \mu\text{m}$ , the deviation is expected from non-ideal operation (bias and threshold settings), and multiple scattering of tracks through the telescope. Especially the testbeam at DESY has a relatively low energy ( $\sim 5 \text{ GeV}$  electrons) compared to e.g. CERN with  $120 \text{ GeV}$  pions.

The hit efficiency in Technical Specification document for testbeam qualification is required to be over 97% for irradiated DUTs. Efficiency of the RD53A module in this thesis is determined to be  $97.651\% \pm 0.035\%$  using TBmon2 analysis which satisfies the requirement. The study of the ATLAS ITk pixel sensor is still in

the R&D phase, i.e. operation conditions such as bias voltage, sensor design, reconstruction and analysis softwares are still under development. The main purpose of the study is to set up the system and perform preliminary studies.

The LHC is usually referred to as the discovery collider, whilst  $e^+e^-$  colliders such as CLIC are expected to be the most powerful particle microscopes for precision measurements. Now that the LHC has finished its job of discovering the  $t\bar{t}H$  process, it is time for CLIC, and other high-energy  $e^+e^-$  colliders, to help us gain more knowledge about the Higgs boson and the Standard Model. Hopefully, even a mere hint of Beyond the Standard Model physics will emerge from these powerful machines that could disclose the blueprint of the Universe.

# Bibliography

- [1] P. W. Higgs. Broken symmetries and the masses of gauge bosons. *Phys. Rev. Lett.*, 13:508–509, Oct 1964.
- [2] F. Englert and R. Brout. Broken symmetry and the mass of gauge vector mesons. *Phys. Rev. Lett.*, 13:321–323, Aug 1964.
- [3] G. S. Guralnik, C. R. Hagen, and T. W. B. Kibble. Global conservation laws and massless particles. *Phys. Rev. Lett.*, 13:585–587, Nov 1964.
- [4] G. Aad, T. Abajyan, B. Abbott, J. Abdallah, S. Abdel Khalek, A. A. Abdelalim, O. Abdinov, R. Aben, B. Abi, M. Abolins, and et al. Observation of a new particle in the search for the Standard Model Higgs boson with the ATLAS detector at the LHC. *Physics Letters B*, 716:1–29, September 2012.
- [5] S. Chatrchyan, V. Khachatryan, A. M. Sirunyan, A. Tumasyan, W. Adam, E. Aguilo, T. Bergauer, M. Dragicevic, J. Erö, C. Fabjan, and et al. Observation of a new boson at a mass of 125 GeV with the CMS experiment at the LHC. *Physics Letters B*, 716:30–61, September 2012.
- [6] ATLAS and CMS Collaborations. Combined Measurement of the Higgs Boson Mass in  $pp$  Collisions at  $\sqrt{s} = 7$  and 8 TeV with the ATLAS and CMS Experiments. *Phys. Rev. Lett.* 114, 191803 (2015), May 2015.
- [7] D. M. Asner et al. ILC Higgs White Paper. In *Proceedings, 2013 Community Summer Study on the Future of U.S. Particle Physics: Snowmass on the Mississippi (CSS2013): Minneapolis, MN, USA, July 29-August 6, 2013*, 2013.
- [8] L. Canetti, Marco Drewes, and Mikhail Shaposhnikov. Matter and antimatter in the universe. *New Journal of Physics*, 14(9):095012, Sep 2012.
- [9] H. Yukawa. On the Interaction of Elementary Particles I. *Proc. Phys. Math. Soc. Jap.*, 17:48–57, 1935.
- [10] D. Atwood, S. Bar-Shalom, G. Eilam, and A. Soni. CP violation in top physics. *Phys. Rept.*, 347:1–222, June 2001.

- [11] P. S. Bhupal Dev, A. Djouadi, R. M. Godbole, M. M. Mühlleitner, and S. D. Rindani. Determining the cp properties of the higgs boson. *Physical Review Letters*, 100(5), Feb 2008.
- [12] P. Lebrun, L Linssen, A Lucaci-Timoce, D Schulte, F Simon, S Stapnes, N Toge, H Weerts, and J Wells. The CLIC Programme: Towards a Staged  $e^+e^-$  Linear Collider Exploring the Terascale: CLIC Conceptual Design Report. Technical Report arXiv:1209.2543. CERN-2012-005. ANL-HEP-TR-12-51. KEK-Report-2012-2. MPP-2012-115, CERN, Geneva, 2012. Comments: 84 pages, published as CERN Yellow Report <https://cdsweb.cern.ch/record/1475225>.
- [13] The ATLAS Collaboration. Combined measurements of higgs boson production and decay using up to  $80 \text{ fb}^{-1}$  of proton–proton collision data at  $\sqrt{s} = 13 \text{ tev}$  collected with the atlas experiment. Technical Report ATLAS-CONF-2019-005, CERN, Geneva, Mar 2019.
- [14] A. M. Sirunyan, A. Tumasyan, W. Adam, F. Ambrogi, E. Asilar, T. Bergauer, J. Brandstetter, M. Dragicevic, J. Erö, A. Escalante Del Valle, and et al. Combined measurements of higgs boson couplings in proton–proton collisions at  $\sqrt{s} = 13 \text{ tev}$ . *The European Physical Journal C*, 79(5), May 2019.
- [15] M. M. Aaboud, G. Aad, B. Abbott, O. Abdinov, B. Abeloos, D.K. Abhayasinghe, S.H. Abidi, O.S. AbouZeid, N.L. Abraham, H. Abramowicz, and et al. Observation of higgs boson production in association with a top quark pair at the lhc with the atlas detector. *Physics Letters B*, 784:173–191, Sep 2018.
- [16] S. L. Glashow. Partial-symmetries of weak interactions. *Nuclear Physics*, 22(4):579 – 588, 1961.
- [17] R. P. Feynman. Mathematical formulation of the quantum theory of electromagnetic interaction. *Phys. Rev.*, 80:440–457, Nov 1950.
- [18] H David Politzer. Asymptotic freedom: An approach to strong interactions. *Physics Reports*, 14(4):129 – 180, 1974.
- [19] H. D. Politzer. Reliable perturbative results for strong interactions? *Phys. Rev. Lett.*, 30:1346–1349, Jun 1973.
- [20] A. Djouadi. The anatomy of electroweak symmetry breaking tome ii: The higgs bosons in the minimal supersymmetric model. *Physics Reports*, 459(1-6):1–241, Apr 2008.
- [21] L. Boyle. Standard model of particle physics, 2014.
- [22] Q. R. Ahmad et al. (SNO Collaboration). Direct evidence for neutrino flavor transformation from neutral-current interactions in the sudbury neutrino observatory. *Phys. Rev. Lett.*, 89:011301, Jun 2002.

- [23] Super-Kamiokande Collaboration. Evidence for oscillation of atmospheric neutrinos. *Phys. Rev. Lett.*, 81:1562–1567, Aug 1998.
- [24] M. Aker, K. Altenmüller, M. Arenz, M. Babutzka, J. Barrett, S. Bauer, M. Beck, A. Beglarian, J. Behrens, T. Bergmann, and et al. Improved upper limit on the neutrino mass from a direct kinematic method by katrin. *Physical Review Letters*, 123(22), Nov 2019.
- [25] N. Cabibbo. Unitary symmetry and leptonic decays. *Phys. Rev. Lett.*, 10:531–533, Jun 1963.
- [26] M. Kobayashi and Toshihide Maskawa. CP-Violation in the Renormalizable Theory of Weak Interaction. *Progress of Theoretical Physics*, 49(2):652–657, 02 1973.
- [27] M. Tanabashi and et al. (Particle Data Group). Review of particle physics. *Phys. Rev. D*, 98:030001, Aug 2018.
- [28] B. P. Abbott, R. Abbott, T. D. Abbott, M. R. Abernathy, F. Acernese, K. Ackley, C. Adams, T. Adams, P. Addesso, R. X. Adhikari, and et al. Observation of gravitational waves from a binary black hole merger. *Physical Review Letters*, 116(6), Feb 2016.
- [29] D. J. Gross and Frank Wilczek. Ultraviolet behavior of non-abelian gauge theories. *Phys. Rev. Lett.*, 30:1343–1346, Jun 1973.
- [30] J. Ellis, Mary K. Gaillard, and Dimitri V. Nanopoulos. A historical profile of the higgs boson. *The Standard Theory of Particle Physics*, pages 255–274, Aug 2016.
- [31] CMS Collaboration . A measurement of the higgs boson mass in the diphoton decay channel. *Physics Letters B*, 805:135425, 2020.
- [32] A. Djouadi. The anatomy of electroweak symmetry breaking: Tome i: The higgs boson in the standard model. *Physics Reports*, 457(1):1–216, 2008.
- [33] J. H. Christenson, J. W. Cronin, V. L. Fitch, and R. Turlay. Evidence for the  $2\pi$  decay of the  $k_2^0$  meson. *Phys. Rev. Lett.*, 13:138–140, Jul 1964.
- [34] J. E. Kim. Strong cp problem, axions, and cosmological implications of cp violation, 2017.
- [35] J.H. Christenson, J.W. Cronin, V.L. Fitch, and R. Turlay. Evidence for the  $2\pi$  Decay of the  $K_2^0$  Meson. *Phys. Rev. Lett.*, 13:138–140, 1964.
- [36] LHCb Collaboration. Physics case for an LHCb Upgrade II - Opportunities in flavour physics, and beyond, in the HL-LHC era. Technical Report LHCb-PUB-2018-009. LHCC-G-171, CERN, Geneva, Aug 2018. ISBN 978-92-9083-494-6.

- [37] M. Maltoni, Thomas Schwetz, Mariam Tórtola, and José W F Valle. Status of global fits to neutrino oscillations. *New Journal of Physics*, 6:122–122, Sep 2004.
- [38] M. F. Sohnius. Introducing supersymmetry. *Physics Reports*, 128(2):39 – 204, 1985.
- [39] R. M. Godbole, C. Hangst, M. Muhlleitner, S. D. Rindani, and P. Sharma. Model-independent analysis of Higgs spin and CP properties in the process  $e^+e^- \rightarrow t\bar{t}\Phi$ . *Eur. Phys. J.*, C71:1681, 2011.
- [40] G. Aad, B. Abbott, D.C. Abbott, A. Abed Abud, K. Abeling, D.K. Abhayasinghe, S.H. Abidi, O.S. AbouZeid, N.L. Abraham, H. Abramowicz, and et al. Cp properties of higgs boson interactions with top quarks in the  $t\bar{t}h$  and  $th$  processes using  $h \rightarrow \gamma\gamma$  with the atlas detector. *Physical Review Letters*, 125(6), Aug 2020.
- [41] ATLAS Collaboration. Measurement of Higgs boson production in association with a  $t\bar{t}$  pair in the diphoton decay channel using  $139 \text{ fb}^{-1}$  of LHC data collected at  $\sqrt{s} = 13 \text{ TeV}$  by the ATLAS experiment. Technical Report ATLAS-CONF-2019-004, CERN, Geneva, Mar 2019.
- [42] M. Thomson. Particle flow calorimetry and ilc detector design.
- [43] O. S. Brüning, Paul Collier, P Lebrun, Stephen Myers, Ranko Ostojic, John Poole, and Paul Proudlock. *LHC Design Report*. CERN Yellow Reports: Monographs. CERN, Geneva, 2004.
- [44] CERN. *LEP design report*. CERN, Geneva, 1984.
- [45] A. Abada, M. Abbresci, S.S. AbdusSalam, and et al. Fcc-ee: The lepton collider. *The European Physical Journal Special Topics*, 228(2):261–623, 2019.
- [46] A. Abada, Abbresci, S.S. M., AbdusSalam, and et al. Fcc-hh: The hadron collider. *The European Physical Journal Special Topics*, 228(4):755–1107, 2019.
- [47] K. Peters. Physics opportunities at future high-energy colliders, 2018.
- [48] M. Bicer, H. Duran Yildiz, I. Yildiz, G. Coignet, M. Delmastro, T. Alexopoulos, C Grojean, S. Antusch, T. Sen, and et al. First look at the physics case of tlep. *Journal of High Energy Physics*, 2014(1), Jan 2014.
- [49] C. Adolphsen, Maura Barone, Barry Barish, Karsten Buesser, Philip Burrows, John Carwardine, Jeffrey Clark, Helene Mainaud Durand, Gerry Dugan, Eckhard Elsen, Atsushi Enomoto, Brian Foster, Shigeki Fukuda, Wei Gai, Martin Gastal, Rongli Geng, Camille Ginsburg, Susanna Guiducci, Mike Harrison, Hitoshi Hayano, Keith Kershaw, Kiyoshi

Kubo, Victor Kuchler, Benno List, Wanming Liu, Shinichiro Michizono, Christopher Nantista, John Osborne, Mark Palmer, James McEwan Paterson, Thomas Peterson, Nan Phinney, Paolo Pierini, Marc Ross, David Rubin, Andrei Seryi, John Sheppard, Nikolay Solyak, Steinar Staphnes, Toshiaki Tauchi, Nobu Toge, Nicholas Walker, Akira Yamamoto, and Kaoru Yokoya. The International Linear Collider Technical Design Report. Technical Report arXiv:1306.6328, Geneva, Jun 2013.

- [50] B. Richter, R. A. Bell, K. L. Brown, A. W. Chao, J. Clendenin, K. F. Crook, W. Davies-White, H. De Staebler, S. Ecklund, G. E. Fischer, R. A. Gould, R. Helm, R. Hollebeek, M.-J. Lee, A. V. Lisin, G. A. Loew, R. E. Melen, R. H. Miller, D. M. Ritson, D. J. Sherden, C. Sinclair, J. Spencer, R. Stiening, H. Wiedemann, P. B. Wilson, and C. Y. Yao. *The SLAC Linear Collider*, pages 168–188. Birkhäuser Basel, Basel, 1980.
- [51] J. Seeman, D. Schulte, J. P. Delahaye, M. Ross, S. Staphnes, A. Grudiev, A. Yamamoto, A. Latina, A. Seryi, R. Tomás García, S. Guiducci, Y. Papaphilippou, S. A. Bogacz, and G. A. Krafft. *Design and Principles of Linear Accelerators and Colliders*, pages 295–336. Springer International Publishing, Cham, 2020.
- [52] A. Robson, P. N. Burrows, N. Catalan Lasheras, L. Linssen, M. Petric, D. Schulte, E. Sicking, S. Staphnes, and W. Wuensch. The compact linear  $e^+e^-$  collider (clic): Accelerator and detector, 2018.
- [53] H. Abramowicz, A. Abusleme, K. Afanaciev, N. Alipour Tehrani, C. Balázs, Y. Benhammou, M. Benoit, B. Bilki, J.-J. Blaising, M. J. Boland, and et al. Higgs physics at the clic electron–positron linear collider. *The European Physical Journal C*, 77(7), Jul 2017.
- [54] H. Abramowicz, N. Alipour Tehrani, D. Arominski, Y. Benhammou, M. Benoit, J.-J. Blaising, M. Boronat, O. Borysov, R. R. Bosley, and et al. Top-quark physics at the clic electron-positron linear collider. *Journal of High Energy Physics*, 2019(11), Nov 2019.
- [55] CLIC Collaboration. CLIC accelerator complex for 3TeV, 2020. <http://clicdp.web.cern.ch/content/clic-accelerator>, Accessed: 2020-06-23.
- [56] M. Aicheler, P. Burrows, M. Draper, T. Garvey, P. Lebrun, K. Peach, N. Phinney, H. Schmickler, D. Schulte, and N. Toge. *A Multi-TeV Linear Collider Based on CLIC Technology: CLIC Conceptual Design Report*. CERN Yellow Reports: Monographs. CERN, Geneva, 2012.
- [57] E. Senes et al. Results of the Beam-Loading Breakdown Rate Experiment at the CLIC Test Facility CTF3. In *8th International Particle Accelerator Conference*, page TUPAB017, 2017.

[58] L. Linssen, Akiya Miyamoto, Marcel Stanitzki, and Harry Weerts. *Physics and Detectors at CLIC: CLIC Conceptual Design Report*. CERN Yellow Reports: Monographs. CERN, Geneva, 2012. Comments: 257 p, published as CERN Yellow Report CERN-2012-003.

[59] D. Dannheim and A Sailer. Beam-Induced Backgrounds in the CLIC Detectors. Apr 2012.

[60] H. Aihara, Burrows, P. and Oreglia, M. SiD Letter of Intent. Technical Report FERMILAB-LOI-2009- 01, FERMILAB-PUB-09-681-E, SLAC-R-989, ILC, 2009.

[61] The ILD Collaboration. The ild detector at the ilc, 2019.

[62] T. Behnke, James E. Brau, Philip N. Burrows, Juan Fuster, Michael Peskin, Marcel Stanitzki, Yasuhiro Sugimoto, Sakue Yamada, and Hitoshi Yamamoto. The international linear collider technical design report - volume 4: Detectors, 2013.

[63] S. Poss and André Sailer. Luminosity spectrum reconstruction at linear colliders. *The European Physical Journal C*, 74(4):2833, Apr 2014.

[64] J. S. Marshall, M. A. Thomson. Pandora Particle Flow Algorithm. In *Proceedings, International Conference on Calorimetry for the High Energy Frontier (CHEF 2013): Paris, France, April 22-25, 2013*, pages 305–315, 2013.

[65] H. L. Tran, Katja Krüger, Felix Sefkow, Steven Green, John Marshall, Mark Thomson, and Frank Simon. Software compensation in particle flow reconstruction. *The European Physical Journal C*, 77(10), Oct 2017.

[66] N. Alipour Tehrani, Jean-Jacques Blaising, Benoit Cure, Dominik Dannheim, Fernando Duarte Ramos, Konrad Elsener, Andrea Gaddi, Hubert Gerwig, Steven Green, Christian Grefe, Daniel Hynds, Wolfgang Klemp, Lucie Linssen, Nikiforos Nikiforou, Andreas Matthias Nurnberg, John Stuart Marshall, Marko Petric, Sophie Redford, Philipp Gerhard Roloff, Andre Sailer, Felix Sefkow, Eva Sicking, Nicolas Siegrist, Frank Richard Simon, Rosa Simoniello, Simon Spannagel, Szymon Krzysztof Sroka, Lars Rickard Strom, and Matthias Artur Weber. CLICdet: The post-CDR CLIC detector model. Mar 2017.

[67] S. Catani, Yu.L. Dokshitzer, M.H. Seymour, and B.R. Webber. Longitudinally-invariant  $k_t$ -clustering algorithms for hadron-hadron collisions. *Nuclear Physics B*, 406(1):187 – 224, 1993.

[68] T. Suehara and Tomohiko Tanabe. Lcfiplus: A framework for jet analysis in linear collider studies. *Nuclear Instruments and Methods in Physics Research Section A: Accelerators, Spectrometers, Detectors and Associated Equipment*, 808:109–116, Feb 2016.

- [69] A. Hoecker, P. Speckmayer, J. Stelzer, J. Therhaag, E. von Toerne, H. Voss, M. Backes, T. Carli, O. Cohen, A. Christov, D. Dannheim, K. Danielowski, S. Henrot-Versille, M. Jachowski, K. Kraszewski, A. Krasznahorkay Jr., M. Kruk, Y. Mahalalel, R. Ospanov, X. Prudent, A. Robert, D. Schouten, F. Tegenfeldt, A. Voigt, K. Voss, M. Wolter, and A. Zemla. Tmva - toolkit for multivariate data analysis, 2007.
- [70] T. Sjöstrand, Stephen Mrenna, and Peter Skands. Pythia 6.4 physics and manual. *Journal of High Energy Physics*, 2006(05):026, 2006.
- [71] KEK. Physsim. <http://www-jlc.kek.jp/subg/offl/physsim/>.
- [72] F. Gaede and J. Engels, Marlin et al. A Software Framework for ILC detector R&D, 2007. EUDET-Report 2007-11.
- [73] C. Grefe and A. Muennich. The CLIC SiD CDR Detector Model for the CLIC CDR Monte Carlo Mass Production. Jun 2011.
- [74] R.D. Heuer, D. Miller, F. Richard, P. Zerwas. *TESLA Technical Design Report, pt. 1-6: the superconducting electron-positron linear collider with an integrated x-ray laser laboratory*. DESY, Hamburg, 2001.
- [75] J. S. Marshall. PandoraPFA LC reconstruction, 2017.
- [76] Z. Wan. A search for new physics with high mass tau pairs in  $p\bar{P}$  collisions at  $\sqrt{s} = 1.96$  tev at cdf, 2005.
- [77] A. Münnich. TauFinder: A reconstruction algorithm for t leptons at linear colliders, 2010. LCD- Note 2010-009.
- [78] G. Salam M. Cacciari and G. Soyez. FastJet User Manual. *Eur. Phys. J.*, C72:1896, 2012.
- [79] S. Redford, P. Roloff, M. Vogelr. Physics potential of the top Yukawa coupling measurement at a 1.4 TeV Compact Linear Collider using the CLIC SiD detector, 2014. CERN, CLICdp-Note-2014-001.
- [80] S. Catani, Y. L. Dokshitzer, M. Olsson, G. Turnock, and B. R. Webber. New clustering algorithm for multijet cross sections in  $e^+e^-$  annihilation. *Physics Letters B*, 269:432–438, October 1991.
- [81] B. C. Nejad, Wolfgang Kilian, Jonas M. Lindert, Stefano Pozzorini, Jürgen Reuter, and Christian Weiss. Nlo qcd predictions for off-shell  $t\bar{t}$  and  $t\bar{t}h$  production and decay at a linear collider. *Journal of High Energy Physics*, 2016(12):75, Dec 2016.
- [82] T. Price, P. Roloff, J. Strube, and T. Tanabe. Full simulation study of the top Yukawa coupling at the ILC at 1 TeV. *European Physical Journal C*, 75:309, July 2015.

- [83] P. Roloff. Physics performance for measurements of chargino and neutralino pair production at a 1.4 TeV CLIC collider. Feb 2013.
- [84] P. Roloff. Monte carlo samples with modified tth coupling, 2017.
- [85] CMS Collaboration. Projected Performance of an Upgraded CMS Detector at the LHC and HL-LHC: Contribution to the Snowmass Process. Technical Report CMS-NOTE-13-002, CERN, Geneva, Jun 2013.
- [86] E. Mobs. The CERN accelerator complex - 2019. Complexe des accélérateurs du CERN - 2019. Jul 2019. General Photo.
- [87] A. Szeberenyi. A luminous future for the lhc. *CERN Courier*, Feb 2015.
- [88] ATLAS Collaboration . *ATLAS detector and physics performance: Technical Design Report, 1.* Technical Design Report ATLAS. CERN, Geneva, 1999.
- [89] ATLAS Collaboration. *ATLAS detector and physics performance: Technical Design Report, 2.* Technical Design Report ATLAS. CERN, Geneva, 1999.
- [90] ATLAS Collaboration. The ATLAS experiment at the CERN large hadron collider. *Journal of Instrumentation*, 3(08):S08003–S08003, aug 2008.
- [91] ATLAS Collaboration. Technical Design Report for the ATLAS Inner Tracker Strip Detector. Technical Report CERN-LHCC-2017-005. ATLAS-TDR-025, CERN, Geneva, Apr 2017.
- [92] ATLAS Collaboration. Technical Design Report for the ATLAS Inner Tracker Pixel Detector. Technical Report CERN-LHCC-2017-021. ATLAS-TDR-030, CERN, Geneva, Sep 2017.
- [93] C. D. Via, Maurizio Boscardin, Gian-Franco Dalla Betta, Giovanni Darbo, Celeste Fleta, Claudia Gemme, Philippe Grenier, Sebastian Grinstein, Thor-Erik Hansen, Jasmine Hasi, Chris Kenney, Angela Kok, Sherwood Parker, Giulio Pellegrini, Elisa Vianello, and Nicola Zorzi. 3d silicon sensors: Design, large area production and quality assurance for the atlas ibl pixel detector upgrade. *Nuclear Instruments and Methods in Physics Research Section A: Accelerators, Spectrometers, Detectors and Associated Equipment*, 694:321 – 330, 2012.
- [94] M. Garcia-Sciveres. The RD53A Integrated Circuit. Technical Report CERN-RD53-PUB-17-001, CERN, Geneva, Oct 2017.
- [95] S. Spannagel, S. Terzo, A. Macchiolo, R. Nisius, B. Paschen, H. Augustin, R. Ballabriga, M. Campbell, E. Heijne, X. Llopart, and et al. Performance of the eudet-type beam telescopes, Jan 1970.
- [96] H. Perrey. EUDAQ and EUTelescope: Software Frameworks for Test Beam Data Acquisition and Analysis. *PoS*, TIPP2014:353, 2014.

- [97] T. Bisanz, A Morton, and I Rubinskiy. EUTelescope 1.0: Reconstruction Software for the AIDA Testbeam Telescope. Mar 2015.
- [98] EUTelescope. A generic pixel telescope data analysis framework.
- [99] R. Diener, J. Dreyling-Eschweiler, H. Ehrlichmann, I.M. Gregor, U. Kötz, U. Krämer, N. Meyners, N. Potylitsina-Kube, A. Schütz, P. Schütze, and et al. The desy ii test beam facility. *Nuclear Instruments and Methods in Physics Research Section A: Accelerators, Spectrometers, Detectors and Associated Equipment*, 922:265–286, Apr 2019.
- [100] D. R. Rodriguez and Edoardo Rossi. Eutelescope guide for atlas itk strip: Reconstruction and analysis, 2017.
- [101] TBmon2. The atlas pixel testbeam analysis framework, 2020.
- [102] L. Rossi. *Pixel detectors: from fundamentals to applications*. Springer, 2006.
- [103] ATLAS Collaboration. Observation of higgs boson production in association with a top quark pair at the lhc with the atlas detector. *Physics Letters B*, 784:173 – 191, 2018.